

DIAMOND ON GaN: HETERO INTERFACE AND THERMAL TRANSPORT  
STUDY

Md Anwar Siddique, M.S.

A dissertation submitted to the Graduate Council of  
Texas State University in partial fulfillment  
of the requirements for the degree of  
Doctor of Philosophy  
with a Major in Materials Science, Engineering, and Commercialization  
August 2019

Committee Members:

Edwin L. Piner, Chair

Mark Holtz

Ravi Droopad

Casey Smith

Harlan R. Harris

**COPYRIGHT**

by

Md Anwar Siddique

2019

## **FAIR USE AND AUTHOR'S PERMISSION STATEMENT**

### **Fair Use**

This work is protected by the Copyright Laws of the United States (Public Law 94-553, section 107). Consistent with fair use as defined in the Copyright Laws, brief quotations from this material are allowed with proper acknowledgment. Use of this material for financial gain without the author's express written permission is not allowed.

### **Duplication Permission**

As the copyright holder of this work I, Md Anwar Siddique, authorize duplication of this work, in whole or in part, for educational or scholarly purposes only.

## **DEDICATION**

I would like to dedicate this dissertation to my mother (Rokeya Begum), father (A B Siddique), my beloved siblings and my wife (Nusrat Jahan Neela).

## **ACKNOWLEDGEMENTS**

First of all, I would like to express my greatest gratitude towards Almighty Allah! I would love to take this moment to express my heartiest appreciation and gratitude towards my parents Rokeya Begum and A B Siddique for their continuous support, unconditional love, continuous believe and all the sacrifices along this arduous journey with every up and down. I want to take this opportunity to express my gratitude and apperception to all my teachers and mentors from preparatory school to this day for their guidance and encouragements. In addition, an especial thanks to my wife Nusrat Jahan Neela for her patient, love and encouragement which kept me on the track.

I would like to express my sincere thanks to my supervisor, Dr. Edwin L. Piner, for his prudent guidance and support throughout my graduate journey. Being a mentor, he has not only enlightened me with his wealth of knowledge about the research topic but also guided me to be a professional, responsible scholar. I truly appreciate his willingness to listen to new ideas, always being encouraging and supportive to find new territory, learn something new.

I would like to thank the other members of my dissertation committee, Dr. Mark Holtz, Dr. Ravi Droopad, Dr. Casey Smith, Dr. Harlan R. Harris for their insightful guidance and continuous support. Especial thanks to Dr. Mark Holtz for his stewardship, guidance and mentorship. Thank you, Dr. Casey Smith, for all your patience with me and

your endless support while using ARSC and cleanroom facility in Texas State. This has been a privilege to get to know you all and to have a chance to learn from you.

I want to acknowledge my friend and as per Dr. Piner, my partner in crime Dr. Raju Ahmed for his endless encouragement and assistance throughout my journey which began a decade ago until this very day. Thanks for being a true friend! I would like to acknowledge my colleagues, Jonathan Anderson, Dr. Mohammed Nazari, and Dr. Luke Yates, for their collaboration and support to this dissertation project.

Finally, I would love to thank the faculty and staffs in the Materials Science, Engineering and Commercialization Program, ARSC, SRO and the Department of Physics for their constant support through my time in Texas State.

## TABLE OF CONTENTS

ACKNOWLEDGEMENTS .....	v
TABLE OF CONTENTS.....	vii
LIST OF TABLES .....	xi
LIST OF FIGURES.....	xii
ABSTRACT .....	xv
CHAPTER	
1 INTRODUCTION.....	1
1.1 GaN/AlGa <sub>N</sub> -based HEMT .....	4
1.1.1 Spontaneous polarization.....	5
1.1.2 Piezoelectric polarization: .....	7
1.1.3 AlGa <sub>N</sub> / GaN HEMT structure.....	10
1.2 Metal organic chemical vapor deposition system for III-Nitride deposition .....	11
2 STRUCTURAL CHARACTERIZATION OF OF AlGa <sub>N</sub> /GaN	
HEMT BY XRD.....	16
2.1 Introduction .....	16
2.2 Experimental Details: .....	19
2.2.1 XRD fundamentals.....	21
2.2.2 Determination of AlN composition in Al <sub>x</sub> Ga <sub>1-x</sub> N for partially- or fully-strained layers.....	26
2.2.3 Bi-axial stress from HRXRD .....	30

2.2.4 Bi-axial Stress from Raman.....	31
2.3 Results and Discussion.....	32
2.4 Conclusions .....	44
3 EFFECT OF REACTANT GAS STOICHIOMETRY OF <i>IN-SITU</i> SiN <sub>x</sub>	
PASSIVATION ON STRUCTURAL PROPERTIES OF MOCVD GROWN	
AlGaN/GaN HEMTS.....	45
3.1 Introduction .....	45
3.2 Materials and Methods.....	46
3.3 Results .....	47
3.4 Conclusions .....	61
4 CO-RELATION OF CONSTITUENT GAS CHEMISTRY AND	
STOICHIOMETRY OF <i>IN-SITU</i> SiN <sub>x</sub> TO THE STRUCTURAL	
AND ELECTRICAL PROPERTIES OF AlGaN/GaN HEMT.....	62
4.1 Introductions .....	62
4.2 Experimental Details.....	63
4.3 Results and discussion.....	65
4.4 Conclusions .....	79
5 OVERVIEW: SELF-HEATING IN AlGaN/GaN HEMTS,	
AND DIAMOND AS A HEAT SPREADER.....	80
5.1 Self-heating in AlGaN/GaN HEMT .....	80
5.2 Diamond as a Heat Spreader .....	82
5.3 Effect of TBR on GaN-on-diamond performance .....	85
5.4 Proposed Solution .....	88

6	STRUCTURAL AND INTERFACE ANALYSIS OF DIAMOND ON AlGa <sub>N</sub> /Ga <sub>N</sub> HEMT UTILIZING AN <i>IN-SITU</i> SiN <sub>x</sub> INTERLAYER GROWN BY MOCVD .....	89
6.1	Introduction .....	89
6.2	Experimental Details .....	92
6.3	Results and Discussion .....	94
6.4	HRXRD results .....	95
6.5	Interface analysis by STEM .....	105
6.6	Thermal Characterization by TDTR .....	107
6.7	Conclusions .....	112
7	OPTIMIZATION OF THERMAL BOUNDARY RESISTANCE OF DIAMOND-AlGa <sub>N</sub> /Ga <sub>N</sub> INTERFACE BY <i>IN-SITU</i> SiN <sub>x</sub> THICKNESS REDUCTION AND CVD DIAMOND GROWTH OPTIMIZATION.....	114
7.1	Introductions .....	114
7.2	Experimental Details .....	115
7.3	Surface, structural and interface characterization of Diamond-on-AlGa <sub>N</sub> /Ga <sub>N</sub> HEMT .....	116
7.4	Thermal Characterization by TDTR .....	122
7.5	Conclusions .....	125
8	CONCLUSIONS AND FUTURE WORKS .....	126
8.1	Conclusions .....	126
8.2	Publications .....	128
8.3	Future Works .....	128
8.3.1	Device fabrication, electrical and thermal properties comparison of HEMT with different TL scheme.....	129

8.3.2	Effect of <i>in-situ</i> SiN <sub>x</sub> passivated AlGa <sub>N</sub> /Ga <sub>N</sub> HEMT on surface-state reduction, RF dispersion and device characterization.....	130
8.3.3	Build a theoretical model to explain the outstanding electrical performance of Si-rich <i>in-situ</i> SiN <sub>x</sub> passivated HEMT.....	130
8.3.4	Thermal conductivity comparison of PECVD or LPCVD vs <i>in-situ</i> SiN <sub>x</sub> .....	131
8.3.5	Fabrication of RF devices using Diamond-on-AlGa <sub>N</sub> /Ga <sub>N</sub> HEMTs .....	131
8.3.6	TBR Optimization of diamond-AlGa <sub>N</sub> /Ga <sub>N</sub> HEMT by further thinning the SiN <sub>x</sub> thickness .....	131
	REFERENCES.....	132

## LIST OF TABLES

Table	Page
1. 1 Spontaneous polarization for different materials.....	7
2.1 Calculated Bragg's angles ( $2\theta$ ) for different accessible asymmetric planes.....	26
2.2 Relaxed lattice parameters for AlN and GaN and corresponding elastic constants.....	30
2.3 Out-of-plane lattice constant $c$ and transition layer composition.....	35
2.4. Comparison of stress-strain from different asymmetric reflections (10-14), (10-15) and (20-25) and visible Raman measurements.....	40
3. 1 Reactant gas flow, SiN <sub>x</sub> growth rate, AlGa <sub>N</sub> barrier layer thickness and AFM RMS roughness.....	49
3. 2 Al mole fraction, strain relaxation and polarization induced charge.....	60
4. 1 Growth conditions and measured structural properties .....	67
4. 2 The structural and electrical properties of in-situ SiN <sub>x</sub> passivated AlGa <sub>N</sub> /Ga <sub>N</sub> HEMT with SiN <sub>x</sub> stoichiometry.....	72
5. 1. Extracted thermal properties of SiN <sub>x</sub> on diamond and Ga <sub>N</sub> .....	87
6. 1 Measured lattice parameters calculated uniaxial strain, hydrostatic and biaxial stress before and after diamond growth.....	100
6. 2 micro-Raman spectroscopy before and after diamond growth.....	104
6. 3 Parameters used in TDTR model and fit parameters.....	112
7. 1 Thickness of the top layers of <i>in-situ</i> SiN <sub>x</sub> passivated AlGa <sub>N</sub> /Ga <sub>N</sub> HEMT wafers determined by XRR.....	117
7. 2 Thermal properties of the Ga <sub>N</sub> -diamond interface from TDTR measurement.....	124

## LIST OF FIGURES

Figure	Page
1. 1 Wurtzite structure of Ga-face and N-face GaN <sup>7</sup> .....	5
1. 2 Crystal structure, polarization and 2DEG formation in pseudomorphic GaN/AlGaN/GaN heterostructure .....	7
1. 3 Polarization charge distributions at different interfaces .....	10
1. 4 General schematic diagram of an MOCVD system .....	12
1. 5 Various parts of the MOCVD reactor.....	14
2. 1 Schematic diagram of the AlGaN/GaN HEMT structures with different transition layer combinations .....	21
2. 2 Schematic of x-ray diffraction & Requirement for Bragg diffraction .....	23
2. 3 A section through reciprocal space for [0001] oriented GaN .....	25
2. 4 Various diffraction geometries .....	25
2. 5 2D AFM images of 1 $\mu\text{m}$ x 1 $\mu\text{m}$ o f HEMT.....	33
2. 6 Measured and simulated grazing incidence x-ray reflectivity data for the three experimental transition layer structures .....	33
2. 7 RSM of AlGaN/GaN HEMT around GaN symmetric (0002) reflections .....	35
2. 8 RSM of AlGaN/GaN HEMT around asymmetric GaN (10-14) reflections .....	41
2. 9 RSM of AlGaN/GaN HEMT around asymmetric GaN (10-15) reflections .....	42
2. 10 RSM of AlGaN/GaN HEMT around asymmetric GaN (20-14) reflections .....	43
3. 1 (a) Growth rate and barrier layer thickness variation (b) XRR profile of HEMT (c) 1 $\mu\text{m}$ $\times$ 1 $\mu\text{m}$ 3D AFM images of the passivated <i>in-situ</i> SiN <sub>x</sub> surface.....	51
3. 2 (a) Growth rate and barrier layer thickness variation (b) XRR profile of HEMT (c) 1 $\mu\text{m}$ $\times$ 1 $\mu\text{m}$ 3D AFM images of the passivated in-situ SiN <sub>x</sub> surface .....	52
3. 3 STEM cross-section images from sample D .....	54

3. 4 RSM of AlGa <sub>N</sub> /Ga <sub>N</sub> HEMT on Si around Ga <sub>N</sub> (10-14) .....	56
3. 5 Hg-probe C-V of the <i>in-situ</i> SiN <sub>x</sub> passivated HEMT .....	60
4. 1 Schematic diagram of <i>in-situ</i> SiN <sub>x</sub> passivated HEMT .....	64
4. 2 1μm x 1μm 2D AFM images of the AlGa <sub>N</sub> /Ga <sub>N</sub> HEMTs .....	67
4. 3 5μm x 5μm 2D AFM images of the AlGa <sub>N</sub> /Ga <sub>N</sub> HEMTs .....	68
4. 4 Measured and simulated grazing incidence XRR spectra of the <i>in-situ</i> SiN <sub>x</sub> passivated AlGa <sub>N</sub> /Ga <sub>N</sub> HEMT .....	68
4. 5 Relationship between constituent gas flow ratio (SiH <sub>4</sub> /NH <sub>3</sub> ) to the surface roughness and SiN <sub>x</sub> growth rate. ....	69
4. 6 RSM of AlGa <sub>N</sub> /Ga <sub>N</sub> HEMT around asymmetric Ga <sub>N</sub> (10-14) reflections .....	71
4. 7 XPS analysis of <i>in-situ</i> SiN <sub>x</sub> comparing the Si2p spectra.....	74
4. 8 XPS analysis of <i>in-situ</i> SiN <sub>x</sub> comparing the N1s spectra.....	75
4. 9 Effect of constituent gas flow ratio (R= SiH <sub>4</sub> /NH <sub>3</sub> ) on (i) barrier layer strain relaxation, (ii) barrier layer biaxial tensile stress, (iii) SiN <sub>x</sub> stoichiometry, (iv) 2DEG sheet charge density, (v) 2DEG mobility, and (vi) sheet resistance .....	78
5. 1 Temperature rise in different regions of an AlGa <sub>N</sub> /Ga <sub>N</sub> heterostructure .....	81
5. 2 Current droop measured from Ga <sub>N</sub> -on-diamond .....	82
5. 3 Temperature rise near the 2DEG channel measured by IR.....	83
5. 4 Schematic process flows for incorporating diamond as a heat spreader for AlGa <sub>N</sub> /Ga <sub>N</sub> HEMTs .....	84
5. 5 $TBR_{eff}$ of Ga <sub>N</sub> -on-diamond as a function of the SiN <sub>x</sub> layer thickness .....	87
6. 1 (a) Schematic of the target diamond-on-AlGa <sub>N</sub> /Ga <sub>N</sub> HEMT structure.....	92
6. 2 Measured and simulated grazing incidence x-ray reflectivity of the <i>in-situ</i> SiN <sub>x</sub> passivated III-Nitride HEMT heterostructure. ....	95
6. 3 AFM images <i>in-situ</i> SiN <sub>x</sub> surface and fully coalesce diamond film. ....	96
6. 4 HRXRD 2-Theta/Theta spectrum of the AlGa <sub>N</sub> /Ga <sub>N</sub> structure on Si (111) before and after diamond growth.....	97

6. 5 RSM of AlGaIn/GaN HEMT around asymmetric GaN (10-14) reflections .....	99
6. 6 Ultraviolet (a) and visible (b) Raman spectra of the AlGaIn/GaN HEMT .....	103
6. 7 Bright-field STEM images of interfacial region (a) before and (b) after diamond growth. EELS data comparison (c) point scan .....	106
6. 8 (a) Experimental TDTR data (red circles) and the analytical fit solution (blue line) (b) Normal distribution of the effective diamond/GaN TBR.....	109
6. 9 Sensitivity analysis of the TDTR model used in this work.....	111
7. 1 Tapping mode 2D AFM 5 $\mu\text{m}$ x 5 $\mu\text{m}$ images of the SiN <sub>x</sub> surface, (a) sample X25, and (b) sample X100. ....	118
7. 2 AFM images of the diamond surfaces of sample X25 , (a) 10 $\mu\text{m}$ x 10 $\mu\text{m}$ diamond, and (b) 5 $\mu\text{m}$ x 5 $\mu\text{m}$ diamond .....	119
7. 3 RSM collected around the asymmetric (10-14) planes before (left) and after (right) diamond deposition.....	120
7. 4 RSM c collected around the asymmetric (10-14) planes before (left) and after (right) diamond deposition.....	121
7. 5 Cross-sectional SEM of Diamond-on-AlGaIn/GaN HEMT interface (a) X25 and (b) X100.....	122
7. 6 Normal distribution of the (a) effective diamond/GaN TBC, and (b) thermal conductivity of CVD diamond of sample X25 deter. ....	124
7. 7 Normal distribution of the (a) effective diamond/GaN TBC, and (b) thermal conductivity of CVD diamond of sample X100.....	125

## ABSTRACT

III-Nitride based high electron mobility transistors (HEMT) have been in the forefront of the 5G LTE revolution and continue to show promise for next-generation terahertz (THz) communications and radar detection systems. GaN-based HEMT devices possess wide bandwidth and high breakdown voltage due to their high electron velocity, high-density two-dimensional electron gas (2DEG), and large breakdown field. More recently, AlGaN/GaN-based transistors for terahertz (THz) emitters and detectors have been reported that can operate from 0.75 THz to 2.1 THz. Furthermore, AlGaN/GaN HEMTs grown on silicon are reported to have switching speeds as high as  $\sim 150$  GHz, while the power densities can exceed 12 W/mm, as well as under harsh operational conditions. The maximum radio frequency (RF) power densities for GaN-based HEMTs reported to date is  $41.4 \text{ Wmm}^{-1}$  at 4 GHz. However, the currently fielded and commercially available HEMTs are operating at only 5-6  $\text{Wmm}^{-1}$ . This massive gap in performance is due to power loss because of self-heating in the HEMT device, which degrades the power added efficiency (PAE) and eventually causes device failure. This self-heating effect is quite severe and can cause a temperature rise in the device as high as  $350^\circ\text{C}$  while operating at  $7.8 \text{ Wmm}^{-1}$ . Creating a low thermally resistive pathway using chemical vapor deposition (CVD) diamond at very close proximity to the self-heating source could effectively dissipate heat, thereby mitigating the self-heating problem. The challenge here is to find the thinnest possible dielectric adhesion layer with low thermal boundary

resistance (TBR) to facilitate diamond growth on the HEMT and to protect it from the harsh CVD diamond growth environment.

*In-situ* SiN<sub>x</sub> using metal organic chemical vapor deposition (MOCVD) has been developed and optimized for use as a dielectric adhesion layer to facilitate diamond growth. The effect of reactant gas stoichiometry of *in-situ* SiN<sub>x</sub> passivation on structural and electrical properties of MOCVD grown AlGaIn/GaN HEMT structures on 100 mm Si (111) is reported. A systematic study on the effect of constituent gas flows on surface morphology and growth rate is reported. X-ray reflectometry and atomic force microscopy is performed to determine the surface morphology and thickness of the near-surface layers. Conformal coverage of SiN<sub>x</sub> with abrupt SiN<sub>x</sub> -III-Nitride interface is confirmed by transmission electron microscopy. When the growth rate of the *in-situ* SiN<sub>x</sub> is less than a critical threshold of 10 nm/hr, the AlGaIn barrier layer is significantly etched. The charge density of the 2DEG induced at the AlGaIn/GaN interface due to polarization and surface state filling is evaluated with Hg-probe C-V profile and calculations based on strain relaxation. Sheet charge density, electron mobility, and sheet resistance were determined by measuring Cloverleaf Hall structures. Passivated samples with growth rates higher than the critical threshold show excellent suppression of strain relaxation in the barrier layer. In addition to the strain induced carrier density, surface state filling with *in-situ* SiN<sub>x</sub> passivation contributes 8-12% of the total sheet charge density. Increased sheet charge density as high as 1.07E13 cm<sup>-2</sup>, mobility up to 2500 cm<sup>2</sup>V<sup>-1</sup>s<sup>-1</sup> and sheet resistance as low as 275 Ω/sq is observed for the *in-situ* passivated samples.

Integration of diamond and AlGaIn/GaN HEMTs terminated with an *in-situ* grown SiN<sub>x</sub> interface layer via MOCVD is also investigated. The effect of diamond growth on the structure and interface properties of the HEMT is studied using high-resolution x-ray diffraction, micro-Raman spectroscopy, atomic force microscopy and scanning transmission electron microscopy (STEM). No structural or physical damage is observed to the HEMT device layers as a result of the hot filament chemical vapor deposited diamond fabrication process. TEM cross-section confirms the smooth and abrupt interface of *in-situ* SiN<sub>x</sub>/AlGaIn/GaN before and after the diamond growth, with no detectable carbon diffusion into the GaN buffer layer. However, selective degradation of the *in-situ* SiN<sub>x</sub> dielectric adhesion layer was observed at the SiN<sub>x</sub>/diamond interface. Using time domain thermoreflectance (TDTR) the effective isotropic thermal conductivity of the diamond was determined to be up to 176 – 35/ + 40 W/m-K. The effective thermal boundary resistance of the diamond/GaN interface (including the SiN<sub>x</sub> and additional layers) was as low as 31 - 2.6/+ 2.5 m<sup>2</sup>K/GW.

# 1 INTRODUCTION

III-Nitride based semiconductor devices possess wide bandwidth and high breakdown voltage simultaneously due to their high electron velocity, high two-dimensional electron gas (2DEG, for heterostructures) and large breakdown field. Wide bandgap, polar semiconductor gallium nitride (GaN) based high electron mobility transistors (HEMTs) have demonstrated high-frequency power amplification from the S-band to W-band with high power-added efficiencies (PAE) and substantially higher output power densities than its competitors, GaAs- or InP- based devices. The maximum RF power densities for GaN-based HEMTs reported to date is  $41.4 \text{ W mm}^{-1}$  at 4 GHz.<sup>1</sup> More recently, AlGaN/GaN-based transistors for terahertz (THz) emitters and detectors has been reported that can operate from 0.75 up to 2.1 THz.<sup>2-4</sup> Furthermore, a heterojunction field-effect transistor (HFET) grown on silicon is reported to have a switching speed as high as  $\sim 160 \text{ GHz}$  with power densities  $>12 \text{ W/mm}$  under harsh operational conditions.<sup>5,6</sup>

The AlGaN/GaN heterostructure has two inherent polarization effects, namely spontaneous polarization due to electronegativity and lack of crystal inversion symmetry, and piezoelectric polarization due to lattice mismatch and thermal strain. Therefore, a high polarization induced electric field is generated within the wurtzite crystal, which creates a charge separation between the surface and interface.<sup>7</sup> If a polarization induced 2DEG is created at the AlGaN/GaN interface, a sheet of opposite charge is also created on the top surface of the AlGaN layer, making the HEMT device highly sensitive to surface states and any modification of surface state filling<sup>7,8</sup>.

As reported by R. Vetury et al.<sup>9</sup> and G. Meneghesso et al.<sup>10</sup> the virtual channel that is created by the surface states is the reason for degradation and dispersion and can be successfully mitigated by passivating the III-N surface. Using an operando photoelectron nanospectroscopy, K. Omika et al. explained the role of SiN<sub>x</sub> in surface electron trapping<sup>11</sup>. SiN<sub>x</sub> passivation reduces the surface-trapped electrons by about 10 % indiscriminately across the surface, which leads to weakening of the local electrical field<sup>11</sup>. This reduction of the surface-electron traps could be the result of the formation of a chemical bond between SiN<sub>x</sub> and the AlGa<sub>N</sub>/Ga<sub>N</sub> HEMT surface<sup>12</sup>. An ideally passivated AlGa<sub>N</sub>/Ga<sub>N</sub> HEMT should have proper surface state filling to avoid any dispersion due to unsatisfied surface dangling bonds and at the time should prevent any relaxation of the pseudomorphic AlGa<sub>N</sub> barrier layer.

As previously reported, *in-situ* SiN<sub>x</sub> suppresses the strain-relaxation in the barrier layer, thereby preventing partial relaxation in the pseudomorphically grown AlGa<sub>N</sub> (> 20 nm) barrier layer<sup>13-15</sup>. The degree of suppression of strain-relaxation should depend on the stoichiometry and, hence, the mechanical property of the SiN<sub>x</sub>. Although suppression of strain relaxation using *in-situ* SiN<sub>x</sub> has been previously reported, the effect of constituent gas chemistry and, hence, the stoichiometry on the degree of strain-relaxation has not been adequately studied. To realize the true potential of *in-situ* SiN<sub>x</sub> passivation, and to thereby design a perfect passivating layer for AlGa<sub>N</sub>/Ga<sub>N</sub> HEMT, the co-relation between the SiN<sub>x</sub> stoichiometry and the suppression of strain-relaxation and surface state filling needs to be correctly understood.

For Ga<sub>N</sub>-based HEMT or HFET, the high current driven through the channel is confined to the very narrow, < 10 nm, 2DEG and therefore produces significant self-

heating (as high as 350 °C for GaN on Si) in the active region of the device <sup>16</sup>. Since the 2DEG and the active GaN/AlGaN layers are very thin, the dissipation of heat from the self-heating source is predominantly vertical.<sup>16</sup> Therefore, a low resistance thermal pathway from the self-heating source to the nearest heat sink (high thermal conductive substrate) is very much desired.

Owing to the outstanding thermal conductivity which can reach up to 2000 W/m-K, chemical vapor deposited (CVD) poly-crystalline diamond is being developed as a better heat spreading substrate than SiC and Al<sub>2</sub>O<sub>3</sub>. Moreover, diamond can provide 5 times better near junction local thermal conductivity than SiC. <sup>17,18</sup> Effective heat spreading in a GaN-on-diamond system is not determined only by the thermal conductivity of CVD polycrystalline diamond but also on the effective thermal boundary resistance ( $TBR_{eff}$ ) at the GaN to diamond interface. Since diamond does not directly grow on GaN, a dielectric adhesion layer (typically < 100 nm SiN<sub>x</sub>) is applied at the GaN-diamond interface. <sup>18,19</sup> SiN<sub>x</sub> has very low thermal conductivity; from ~ 1 - 12 W/m-K <sup>20</sup> where for GaN it is 130 W/m-K and for diamond up to 2000 W/m-K. <sup>17</sup> Therefore, having such a layer at the interface causes a huge thermal mismatch and results in an increased TBR.

To realize the full potential of the GaN-on-diamond system TBR has to be minimized. This research project proposes to understand the heat dissipation from the self-heating source to the heat spreader substrate, to find ways to reduce TBR using ultra-thin *in-situ* SiN<sub>x</sub> dielectric adhesion layer.

## 1.1 GaN/AlGaN-based HEMT

In general, III-nitrides exist in two different structural forms, either the wurtzite (hexagonal) or zincblende crystal structure. Wurtzite has two lattice constants:  $a$  and  $c$ , but zincblende has only one:  $a$ , as all three edges of the interpenetrating cubic structure are identical.<sup>21</sup> Among the two, the wurtzite structure is the thermodynamically stable phase under typical conditions. The metastable zincblende structure is formed mainly when GaN is grown on a cubic material such as GaAs and 3C-SiC under strictly controlled conditions.<sup>22</sup> Normally, III-nitrides crystallize in the hexagonal (wurtzite) phase. The existence of strong spontaneous and piezoelectric fields is a unique feature of the hexagonal III-nitrides grown along the  $c$ -axis.<sup>22,23</sup> Parameters like lattice constant  $a_o$  (the basal edge length),  $c_o$  (height of the hexagonal lattice cell) and  $u_o$  (cation-anion bond length ratio along  $[0001]$  direction) define the wurtzite structure as shown in **Figure 1.1** The subscript “o” indicate that these values are the equilibrium lattice. For an ideal wurtzite structure crystal the  $c_o/a_o$  ratio equals 1.633 and the value of  $u_o$  is 0.374.<sup>21</sup> Zincblende and wurtzite both have polar axes (lack of inversion symmetry). In the wurtzite structure the bonds in the  $\langle 0001 \rangle$  direction and for zincblende in  $\langle 111 \rangle$  direction are all faced by nitrogen (N) in the same direction while the cation (Ga) is in the opposite direction. Both surface and bulk properties depend on whether the surface is nitrogen or metal atom faced.<sup>24</sup>

The typical growth direction of hexagonal GaN is normal to the  $\{0001\}$  basal plane, where the atoms are arranged in bilayers consisting of two closely spaced hexagonal layers, one with cations and the other with anions, such that the bilayers have polar faces.<sup>24</sup> Therefore, for GaN, the basal surface is either Ga- or N-faced. Ga face doesn't mean Ga-

terminated rather it means Ga on the top position of the {0001} bilayer corresponding to [0001] polarity (**Figure 1.1**).

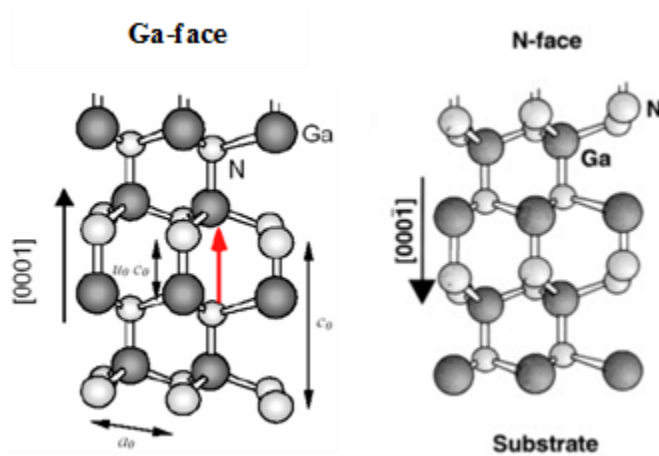


Figure 1.1 Wurtzite structure of Ga-face and N-face GaN. <sup>7</sup>

The term “termination” should only be used to describe a surface property. A surface which is N-face might be Ga-terminated if it is covered with gallium atoms, but without flipping the crystal it will never be Ga-faced. More importantly the (0001) and (000 $\bar{1}$ ) surfaces of GaN are inequivalent (by convention, the [0001] direction is given by a vector pointing from a Ga atom to a nearest neighbor N atom) <sup>24</sup> Lack of inversion symmetry in III-nitrides along the hexagonal c-axis provide nanoscopic spontaneous polarizations. Furthermore, tensile or compressive strain due to lattice mismatch in AlGaN/GaN-type heterostructures induces piezoelectric polarization. <sup>23</sup>

### 1.1.1 Spontaneous polarization

The position of the nitrogen in the periodic table (the most electronegative Group-V and the topmost smallest atom) makes it special among other III-V compounds, as this has a significant impact on properties. The electronic configuration of a N atom is  $1s^2 2s^2 2p^3$  and indicates empty outer orbitals. Therefore, the electron involve in the covalent gallium-

nitrogen bond will be strongly attracted by the Coulomb potential of the N atomic nucleus. This implies the bond between gallium-nitrogen (or, generally, the group III metal atom and nitrogen) will have stronger ionicity than any other III-V covalent bond. This ionicity of the metal-nitrogen bond causes nanoscopic polarization and will result in a macroscopic polarization as large as 3 MV/cm, along the hexagonal c-axis, because the wurtzite GaN crystal has lack of inversion symmetry parallel to [0001] <sup>21,22</sup>. As this polarization occurs absent any strain in the lattice and in equilibrium lattice conditions, this is said to be spontaneous. In the case of the AlGaN/GaN heterostructure, spontaneous polarization is more significant than the piezoelectric polarization. <sup>22</sup>

Spontaneous polarization is strongly affected by the non-ideality of a crystal structure. All four bonds in the tetrahedral structure have equal ionicity but only the bond along the hexagonal c-axis contribute to the spontaneous polarization because the other three are aligned in such a way that each counteract the effect of adjacent similar bonds and, therefore, no net polarization. <sup>22</sup> If the  $c_0/a_0$  ratio decreases, e.g.,  $c_0$  decreases and  $a_0$  increases, the three bonds obtain a wider angle from the c-axis and their resultant dipole compensation decreases. All of these factors contribute to the increase in the macroscopic spontaneous polarization. **Table 1.1** shows the non-ideality increase as the  $c_0/a_0$  ratio shifts from the ideal value of 1.633. Spontaneous polarization increases going from GaN to AlN. As noted, the orientation of the polarization is positive pointing from the metal cation (Ga, Al, In) to nitride anion. Therefore, spontaneous polarization for Ga-face nitrides is negative, i.e. directed toward the substrate, while for N-face the direction is toward the surface of the layer sequence. <sup>21,22</sup>

Table 1.1 Spontaneous polarization for different materials. <sup>23</sup>

Material	AlN	GaN	InN
$c_0/a_0$	1.6010	1.6259	1.6116
$P_{sp}(C/m^2)$	-0.081	-0.029	-0.032

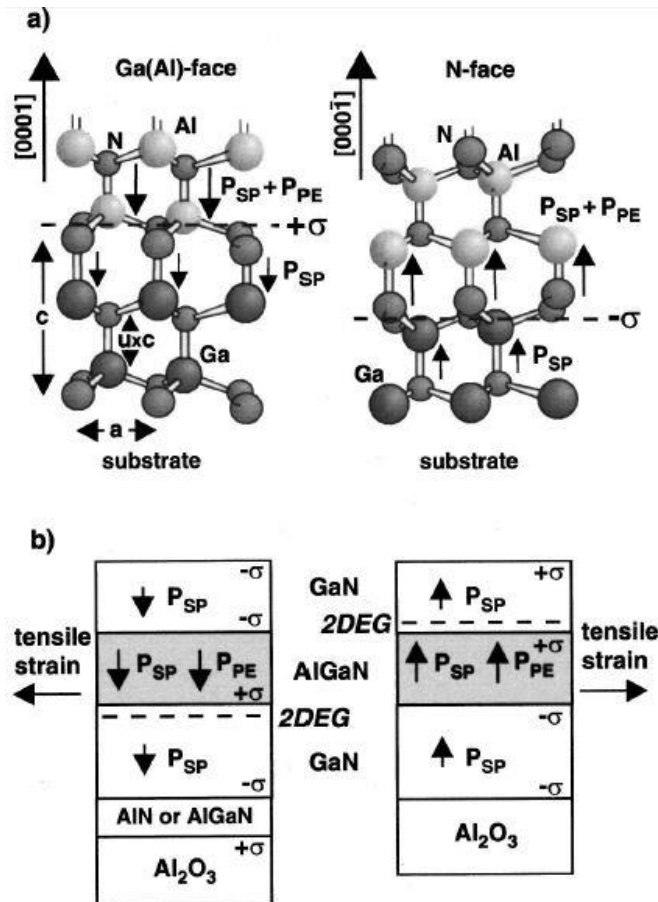


Figure 1.2 a) Crystal structure, polarization induced bound sheet charge, and spontaneous and piezoelectric polarization direction for both N-face and Ga-face. b) 2DEG formation in pseudomorphic GaN/AlGaN/GaN heterostructures with Ga-face and N-face polarity. <sup>23</sup>

### 1.1.2 Piezoelectric polarization:

Due to the difference in lattice constant between AlN and GaN, a significant lattice mismatch takes place when AlGaN is grown on GaN. Strain is induced in the III-N crystal as a result of this lattice mismatch which results in a displacement of the anion-sublattice

to the cation-sublattice. The result of this phenomenon is an induced piezoelectric polarization. The piezoelectric tensor is comprised of three independent components ( $C_{6v}$  point group).<sup>23,24</sup>

The relevant relationship can be derived from two of these components which gives the piezoelectric polarization  $P_{PE}$  as

$$P_{PE} = e_{33}\epsilon_z + \epsilon_{11}(\epsilon_x + \epsilon_y) \quad (1.1)$$

Where  $\epsilon_z = (c-c_0)/c_0$  is the strain along the c-axis, isotropic in plane strain,

$\epsilon_x = \epsilon_y = (a - a_0)/a_0$ ,  $e_{33}$ ,  $e_{31}$  are the Piezoelectric coefficients, and  $a$ ,  $c$ , are the lattice constants of the strained layer. The relation between lattice constants in the hexagonal AlGaIn system is given by

$$\frac{c-c_0}{c_0} = -2 \frac{C_{13}}{C_{33}} \frac{a-a_0}{a_0} \quad (1.2)$$

Where  $C_{13}$  and  $C_{33}$  are elastic constants. Combining equation (1.1) and (1.2), the piezoelectric polarization along the hexagonal c-axis can be determined by,

$$P_{PE} = 2 \frac{a-a_0}{a_0} (e_{31} - e_{33} \frac{C_{13}}{C_{33}}) \quad (1.3)$$

From a microscopic point of view, a strain in the lattice parallel or perpendicular to the c-axis creates an internal displacement of the metal sublattice with respect to the nitrogen sublattice.<sup>23</sup> Piezoelectric polarization is positive for compressive strain and negative for tensile strained AlGaIn layers. Therefore, the orientation of spontaneous

polarization and piezoelectric polarization is parallel in case of tensile strain and opposite of each other in case of compressive strain. Here, we are considering the case where the AlGa<sub>N</sub> barrier is grown on a GaN buffer layer and as a result the AlGa<sub>N</sub> barrier layer is grown under tensile strain. For a case like this as shown in **Figure 1.2**, the direction for spontaneous polarization and piezoelectric polarization is parallel to each other and the sum of both spontaneous and piezoelectric polarization gives the total polarization,

$$P = P_{PE} + P_{SP} \quad (1.4)$$

As seen in **Table 1.1**, both the spontaneous and piezoelectric polarization increases from GaN to AlN, the total polarization for a strained (or even for unstrained) AlGa<sub>N</sub> layer has to be larger than that of a fully relaxed GaN buffer layer. As a result, both negative spontaneous polarization and negative piezoelectric polarization within the AlGa<sub>N</sub> layer under tensile strain points from nitrogen to the nearest neighbor metal atom (Ga or Al) along the hexagonal c-axis. As a result of all these factors, total polarization of both AlGa<sub>N</sub> and GaN layers act toward the substrate.

Polarization induced charge density is determined by a gradient associated with the polarization in space and is defined as,

$$\rho_p = -\nabla P \quad (1.5)$$

In any top/bottom layer AlGa<sub>N</sub>/GaN or GaN/AlGa<sub>N</sub> heterostructure the polarization causes a fixed density of polarization charge and can be defined by,

$$\begin{aligned} \sigma(P_{PS} + P_{PE}) &= P(bottom) - P(top) \\ &= \{P_{PS}(bottom) + P_{PE}(bottom)\} - \{P_{PS}(top) + P_{PE}(top)\} \end{aligned}$$

$$\begin{aligned}
&= \{ P_{PE}(bottom) - P_{PE}(top) \} - \{ P_{PS}(bottom) - P_{PS}(top) \} \\
&= \sigma(P_{PE}) + \sigma(P_{SP}) \tag{1.6}
\end{aligned}$$

### 1.1.3 AlGa<sub>N</sub>/ GaN HEMT structure

The AlGa<sub>N</sub>/GaN heterostructure is composed of two different bandgap materials stacked on top of each other, typically referred to as the barrier and channel layer, respectively. In general, a thin, strained and unintentionally doped AlGa<sub>N</sub> layer is grown on top of an unintentionally doped insulating GaN layer. The schematic diagram in **Figure 1.3** shows the basic single structure HEMT with its corresponding band diagram at flat band, or unbiased, condition.

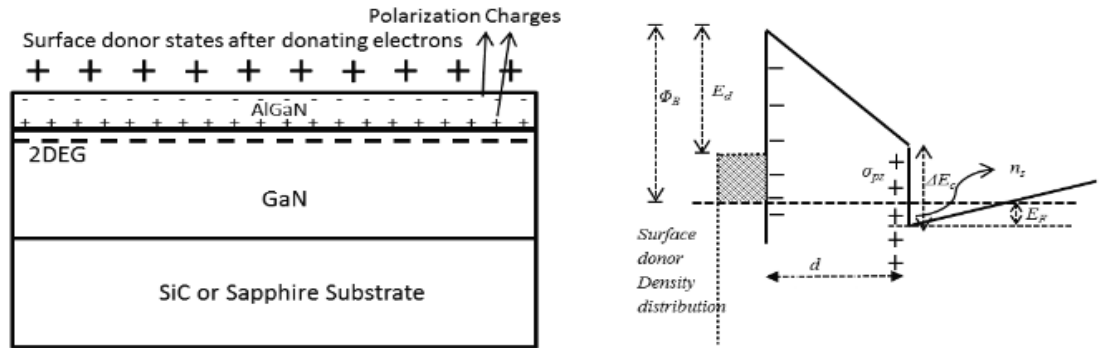


Figure 1.3 AlGa<sub>N</sub>/GaN HEMT structure showing polarization charge distributions at different interfaces and corresponding band diagram showing various charges at different interfaces, including the 2DEG at the AlGa<sub>N</sub>/GaN interface.

AlGa<sub>N</sub> and GaN have inherent polarization effects. Therefore, a high polarization induced electric field is generated in the AlGa<sub>N</sub> barrier layer for Ga-face crystal and the top surface donor state at the top interface would donate the electrons to form a 2DEG at the AlGa<sub>N</sub>/GaN heterojunction without any bias applied to the gate.<sup>25</sup> Therefore devices produced therein are normally ON.

## 1.2 Metal organic chemical vapor deposition system for III-Nitride deposition

Metal organic chemical vapor deposition (MOCVD) is a non-equilibrium semiconductor film deposition technique which involves gas phase transport of organometallic precursors (OM), hydrides (the nitrogen source, such as ammonia) and carrier gases onto a heated substrate where the precursors are pyrolyzed and film is deposited<sup>24</sup>. MOCVD growth has very complex growth chemistry and the growth is also influenced by the reactor's flow dynamics, especially the reactor chamber geometry. MOCVD reactor system design requires simultaneous considerations of thermodynamics and kinetics because they critically affect the structural, electronic and optical properties of grown thin films, as well as uniformity, controllability and run-to-run repeatability of the growth process<sup>26</sup>.

The basic MOCVD reactor must have three major components as shown in **Figure 1.4 (a)**: (i) the gas delivery system, (ii) the reactor growth chamber and (iii) exhaust system.

The detailed chemical reactions involved in a MOCVD process are very complicated in nature. However, the process can be represented by a very simple formula for a reaction of III-V employing metal-organic precursors ( $R_3M$ ) and hydride precursors<sup>26</sup>,



where M is a Group III metal atom, e.g., Ga, Al or In; R is an organic radical, typically  $CH_3$ (methyl) or  $C_2H_5$  (ethyl); E is a Group V atom e.g., As, P or N; and H is atomic hydrogen. The main difference of MOCVD compared to other CVD processes stems from the use of organometallic precursors. Compound semiconductors such as GaN, AlN and their alloys can be grown by MOCVD by using precisely controlled mass flow controllers (MFCs) and pressure controller (PCs). A simplified schematic diagram of a basic MOCVD

system and its various parts are shown in **Figure 1.4** For a III-Nitride MOCVD system, precursors and their transport system are completely different than a conventional CVD process. MOCVD of III-V compound semiconductors generally employs mixtures of Group III metal-organic and Group V hydride precursors in a carrier gas. Typical carrier gases are  $H_2$ ,  $N_2$ , or a mixture of  $H_2$  and  $N_2$ , and the precursors are transported by the one or more carrier gases and injected into an open-tube process chamber<sup>26</sup>.

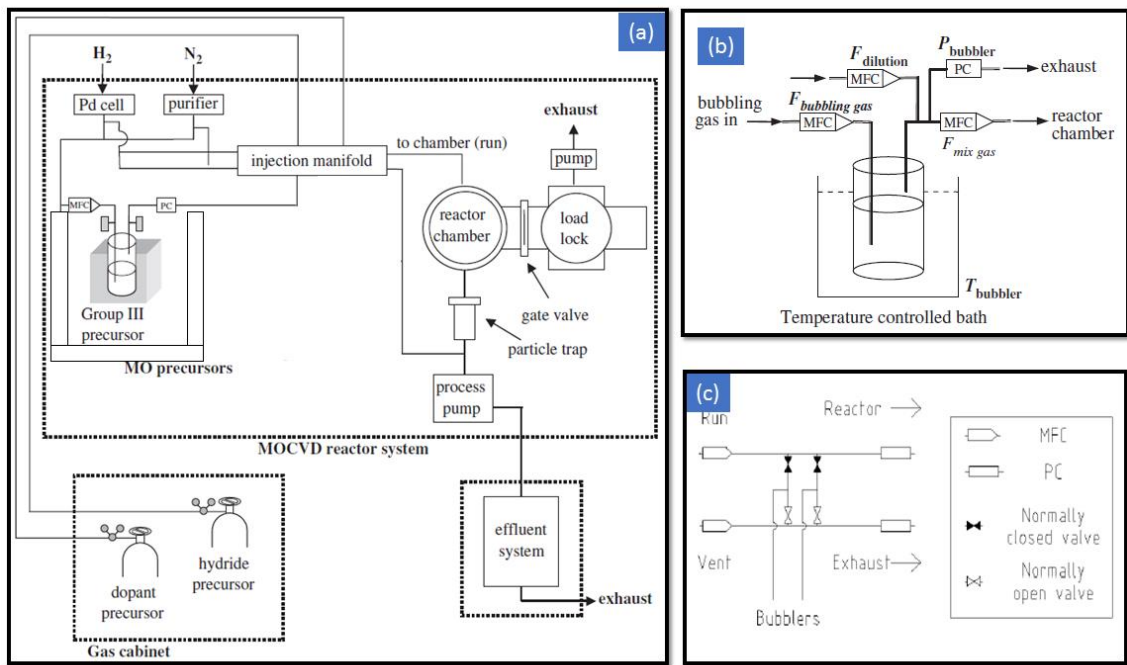


Figure 1.4 (a) General schematic diagram of an MOCVD system showing the main components only.<sup>26</sup> (b) Schematic diagram of a bubbler used for organometallic precursors and (c) run vent manifold used for MOCVD reactor<sup>27</sup>.

The most common OM precursors used for MOCVD are trimethylaluminum (TMA) (liquid at room temperature), trimethylgallium (TMG) (liquid at room temperature), and trimethylindium (TMI) (solid at room temperature). The OM precursors come in a sealed metal container because of their pyrophoric nature. The special metal

container is called a ‘bubbler’ as shown in **Figure 1.4 (b)** Since OM precursors are either liquid or solid at room temperature, they are kept in temperature-controlled baths and a carrier gas is flowed into the bubbler where it enters through a dip tube submerged in the OM. After the carrier gas bubbles through the OM liquid precursors, they become saturated based on the vapor phase of the OM above the liquid surface. Unless the gas flow rate is too high, the bubbling action sets up an equilibrium between the condensed phase and the vapor phase.

For typical III-Nitride growth via MOCVD, multiple layers of materials are deposited and abrupt interfaces between layers is necessary to realize III-Nitrides heterostructures. The flow from the bubbler to the reactor is, therefore, controlled in a precise way by linking a normally closed valve to a normally open valve in a configuration known as a run/vent manifold illustrated **Figure 1.4 (c)**. Initially, the flow is directed to the vent line which bypasses the reactor and valves are activated when flow to the reactor is required<sup>27</sup>. In the switching manifold, the individual precursor gas flows are switched, combined and routed into either the growth chamber or the vent (exhaust) line, while maintaining a differential pressure of nearly zero between the ‘run’ and ‘vent’ line so that the gas flow switching transient is minimized and does not affect the growth process<sup>26</sup>. More details of the MOCVD process with mass flow calculations, OM and reactor design are found elsewhere.<sup>26</sup>

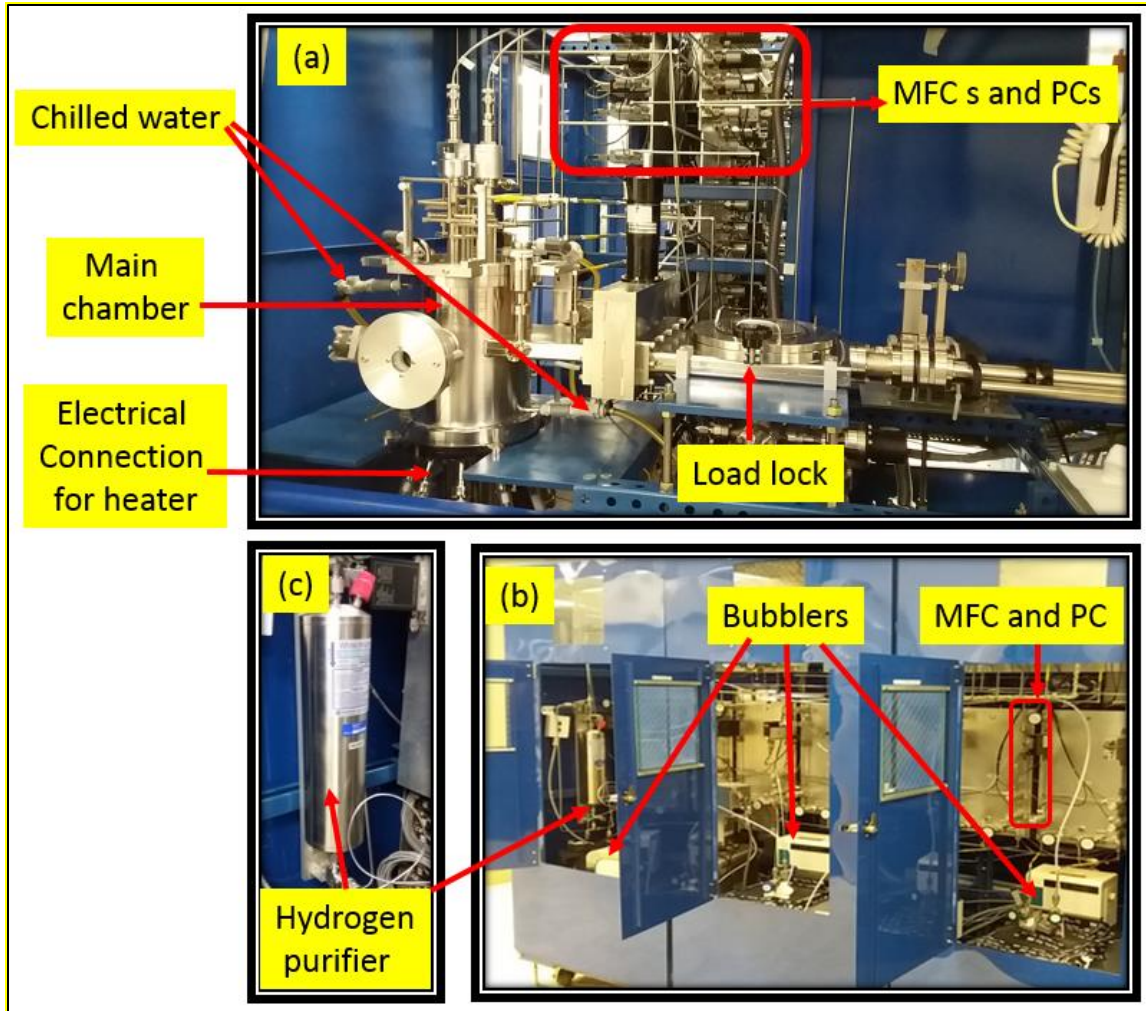


Figure 1.5 Various parts of the MOCVD reactor at Texas State. (a) Main deposition chamber, (b) bubblers and associated MFCs and PCs, and (c) magnified view of the hydrogen purifier.

The Texas State MOCVD reactor used for this dissertation research is shown in **Figure 1.5** which was donated by M/A-Com Inc. and was installed in 2014. This reactor was in production before being decommissioned in 2014. As seen from the images, the design is much more complex than the simple schematics shown in **Figure 1.5**. The main chamber and load lock is seen in **Figure 1.5 (a)** along with pyrometer, gas lines and electrical feed through. The bubblers and purifier, as seen in **Figure 1.5 (b)** and **(c)**, are connected to the main chamber through the run/vent manifold via MFCs and PCs. The

ammonia, silane, nitrogen and hydrogen gas cylinders are stored in separate gas cabinets. Each gas storage unit has adequate safety systems involving the metallic case and exhaust system with sensors to detect leaks. Hydrogen is used as the carrier gas and nitrogen is used for purging. Hydrogen, nitrogen, and ammonia are delivered in high pressure cylinders. The growth parameters for various nitride semiconductors are different in terms of V/III gas phase ratio, pressure and temperature. A baseline AlGaIn/GaN HEMT on Si recipe is generally employed and includes a thin ( $< 1$  nm) AlN profile layer at the AlGaIn/GaN interface, a growth temperature of  $\sim 1020$  °C and a chamber pressure between 30 and 100 Torr.

To optimize the growth of *in-situ* SiN<sub>x</sub> on the baseline AlGaIn/GaN HEMT, first a 200 ppm 6N pure SiH<sub>4</sub> in H<sub>2</sub> cylinder was used as the Si precursor. After initial experiments, higher SiH<sub>4</sub> concentration was needed and a 2 % SiH<sub>4</sub> in H<sub>2</sub> cylinder was installed. Due to environmental restrictions we kept the SiH<sub>4</sub> concentration to less than 4 % to minimize the complexity of handling hazardous gases. Details of the experimental growth process is described later.

## 2 STRUCTURAL CHARACTERIZATION OF OF AlGaN/GaN HEMT BY XRD

### 2.1 Introduction

X-ray diffraction (XRD) is a non-destructive technique widely used to determine different structural parameters such as thickness, interplanar spacing (and, thereby, lattice parameters; in-plane and out-of-plane), stress-strain state, composition of alloys and defect densities. For the III-Nitrides, single crystal large area homo-substrates (AlN or GaN) are only available in small size and low quantity and are, thus, highly priced. Thus, the typical choice of growing III-Nitrides is to use a foreign substrate such as silicon, sapphire, or silicon carbide<sup>24</sup>. Among these choices, GaN on Si is widely used due to its availability as a large area substrate compared to sapphire or SiC and most importantly, due to low-cost and processability. Due to the high lattice mismatch (17% between GaN and Si (REF)) and difference in thermal expansion coefficients (TEC) (as high as 56%), heteroepitaxial growth typically results in high levels of film strain, defect formation (unintentional doping, point defects) and generation of extended defects such as stacking faults and dislocations<sup>22,28</sup>.

The typical epitaxial sequence of growing GaN on Si starts with an AlN nucleation layer, which not only provides lower strain with Si, owing to its closer lattice match with Si compared to GaN, but also prevents the Ga-Si eutectic phase transformation<sup>24</sup>. AlN has a lattice constant smaller than GaN which provides compressive strain to the GaN layer grown above the AlN nucleation layer, this compressive strain balances the tensile strain which occurs during cool down from the growth temperature to room temperature due to the difference in TEC between GaN and Si<sup>29</sup>.

Determining the lattice parameters for III-Nitrides (such as alloy composition and lattice strain) via XRD measurement is challenging for various reasons. The first difficulty arises from the fact that the reported reference cell parameters and elastic constants have a wide range of values<sup>29</sup>. Therefore, the choice of the set of cell parameters impacts the determined lattice parameters.

The second problem is to select an appropriate reference for comparing measurements. For a precise measurement, the substrate is typically used as a reference to minimize errors. III-nitride semiconductors are typically grown on Si (111), SiC and Sapphire (0001). In the case of III-nitride growth on a sapphire substrate, there is a 30° in-plane rotation between the substrate and epilayer<sup>30</sup>. For GaN on Si, the substrate and epilayer peaks are widely separated. Furthermore, for asymmetric reflections, the epi-GaN (h k l) and substrate Si (h k l) are not in the same plane. Therefore, it is very challenging to use the substrate as the reference for asymmetric scans for heteroepitaxial III-Nitride layers on silicon. Finally, again, due to the lattice mismatch and TEC difference in all the transition and buffer layers, such as AlN, GaN or any of their alloys ( $\text{Al}_x\text{Ga}_{1-x}\text{N}$ ), there exists some degree of residual stress<sup>31</sup>. So, taking an epilayer as a reference is not appropriate. Therefore, the reference choice of either partially relaxed  $\text{Al}_x\text{Ga}_{1-x}\text{N}$ , GaN or the substrate as a reference comes with pros and cons.

Choosing Si as the reference has some advantages, especially that its lattice parameters and elastic constants are well established. By choosing an appropriate asymmetric reflection, for example, around the GaN (10-14) plane which is in the vicinity of Si (313) as reported by Kadir et al.<sup>30</sup>, one can calculate both reference and epi-layer lattice parameters within a single scan. Although Si has well-established lattice parameters

and elastic constants, due to intentional and/or unintentional substrate miscut, III-nitride crystallographic tilt has been observed on Si(111) substrates<sup>32,33</sup>. H. Liu et al. showed that having a tilt of 0.2° can cause a change of 0.029 Å to the lattice constant of a relaxed GaN layer which could lead to an inaccuracy of  $\Delta\varepsilon_{xx} = 0.92\%$  in the in-plane strain measurement which is greater than the largest in-plane strain in the structure (typically AlN)<sup>34</sup>. On the other hand, GaN is on the same azimuth as AlN and AlGaN, so there is no crystallographic tilt between GaN and AlN (or AlGaN), Thus, GaN is the more reliable reference and is widely used for strain measurements for GaN-on-Si, GaN-on-SiC and sapphire<sup>29,32,35</sup>.

One can try to compensate for the residual strain issue by choosing a strain invariant reflection plane such as reported by Wallis et al.<sup>31</sup> They determined strain invariant asymmetric reflection planes, such as GaN (20-24) and GaN (20-25), from the relationship,

$$\frac{\delta d}{d} = \frac{\delta a}{a} \left( 1 - \left( \frac{1+\nu}{1-\nu} \right) \cos^2(\theta) \right) \quad (2.1)$$

Where  $\nu$  is Poisson's ratio and  $\theta$  is the angle between the epilayer normal, typically (0001), and the asymmetric (h k l) reflection. When  $1 - \left( \frac{1+\nu}{1-\nu} \right) \cos^2(\theta) = 0$ , the d spacing is no longer affected by the biaxial strain. The determination of plane direction depends on Poisson's ratio and reported values do vary depending on the material quality and growth conditions. These sources of variation must be considered when measuring composition. From the discussion above, using symmetric and asymmetric diffraction, composition and stress-strain states of III-Nitride layers have been evaluated. In most of the reports, however, the AlGaIn layers used to determine composition and strain have been sufficiently thick and, hence, relaxed.<sup>30,31</sup> S.K. Jana reported detailed HRXRD studies of AlGaIn/InGaIn/GaN heterostructures with a 20 nm AlGaIn layer grown on sapphire<sup>36</sup> but

didn't compare all the possible reflection combinations. S Magalhaes et. al. reported on the determination of Al composition in AlInGaN-GaN-sapphire by HRXRD and compared with other techniques like Rutherford back scattering (RBS) and atom probe tomography (APT), but the HRXRD analysis was, again, limited. Therefore, to date, there has not been a detailed HRXRD analysis of fully strained AlGaN/GaN on Si where the effect of the different choices of asymmetric reflections on the determination of Al composition for fully strained pseudomorphically grown (>20 nm) AlGaN barrier layer has been assessed.

This chapter reviews the previously determined methods and compares the different reflection plane choices and suggests a more suitable method of determining the composition and stress-strain state of a fully pseudomorphically strained AlGaN barrier layer.

## **2.2 Experimental Details:**

GaN(cap)/AlGaN(barrier)/AlN(profile)/GaN(buffer) HEMT structures with three different transition layer schemes were grown using a custom-built cold wall, shower head MOCVD system on low resistivity (40  $\Omega$ -cm) on-axis Si(111) substrates. Trimethylgallium (TMGa), Trimethylaluminium (TMAI) and Ammonia (NH<sub>3</sub>) were used as precursors with H<sub>2</sub> as the carrier gas. For each of the three growth schemes, growth was initiated using AlN as a nucleation layer on Si to avoid Ga and Si eutectic phase formation. Subsequent Al<sub>x</sub>Ga<sub>1-x</sub>N transition layers were grown to compensate for thermal expansion mismatch and lattice mismatch. For sample SG1, two-step graded transition layers with  $x = 0.51$  for transition layer one (TL1) and  $x = 0.26$  for transition layer two (TL2) were used. For sample SG2, one additional transition layer with  $x = 0.75$  was added to the transition layers of SG1 to additionally compensate the TEC and lattice mismatches. Finally, a third sample, CG,

contains a continuous graded transition layer where the Al composition is varied from 100% to 0% (i.e., AlN to GaN) within the transition layer thickness. **Figure 2.1(a)-(c)** illustrates the three experimental structures. An 870 nm thick unintentionally doped GaN buffer layer was grown on the transition layers (SG1, SG2, and CG). The device layers included a 1.5 nm AlN profile, a 20 nm strained Al<sub>0.26</sub>Ga<sub>0.74</sub>N barrier layer and, finally, a ~ 1.5 nm GaN cap, all grown at 1020 °C with a chamber pressure of 100 Torr.

X-ray reflectometry (XRR) of the AlGa<sub>x</sub>N/GaN was performed using a Bruker SmartLab 3kW system to determine the thickness of the top active layers. A two-bounce Ge (220) X2 monochromator with a 1D HyPix detector was used for HRXRD reciprocal space mapping (RSM) around the GaN asymmetric (10-14), (10-15) and symmetric (0002) planes to determine the stress and composition of the constituent layers. The measurements were performed using grazing exit (GE) geometry to minimize instrument induced aberration. For the GaN (20-25) reflection a two-bounce Ge (220) X2 monochromator on the incident side was used, coupled with a two-bounce Ge (220) X2 analyzer on the receiver side and 0D detector to enable measuring the high angles of the 2<sup>nd</sup> order diffraction peaks. The measurements were performed using a grazing incident (GI) geometry. For all of these measurements, the sample tilt axis ( $\chi$ ) to the surface normal was kept at ( $\chi = 0$ ), and the asymmetric reciprocal points were accessed by compensating the incident angle,  $\omega$ , accordingly, as discussed below. A Bruker Dimension ICON system was used in tapping mode for AFM measurements of the HEMT surface. Visible (532 nm) micro-Raman measurements were performed to assess the structural and interface properties of the III-Nitride layers.<sup>37</sup> Bulk samples were used to determine the GaN (TDI, Inc.) and AlN

(Crystal IS) reference phonon energies. Further details of the measurements can be found elsewhere.<sup>37,38</sup>

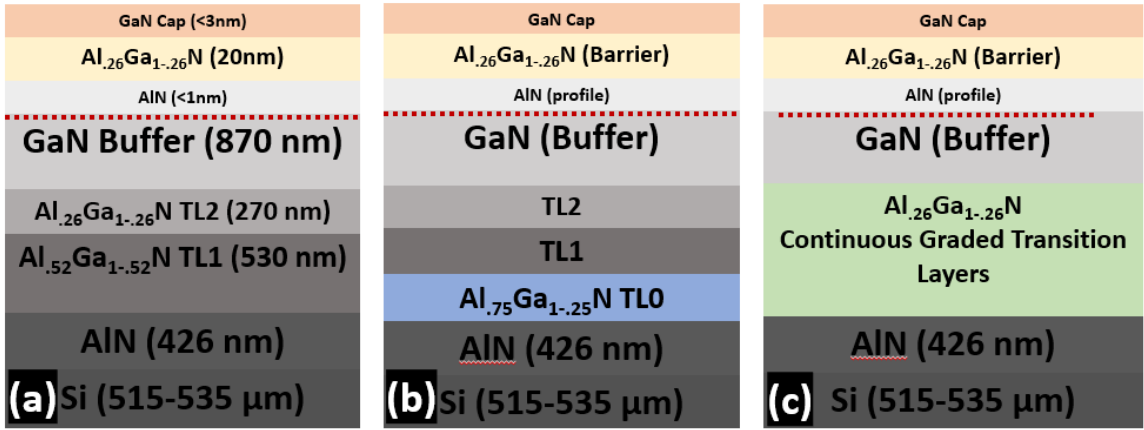


Figure 2.1 Schematic diagram of the AlGaN/GaN HEMT structures with different transition layer combinations. (a) Two-step graded transition layer (SG1), (b) three-step graded transition layers (SG2), and (c) continuous graded transition layers (CG).

### 2.2.1 XRD fundamentals

X-ray diffraction involves probing a crystal with x-ray radiation which has a wavelength ( $\lambda$ ) with the same order of magnitude as the lattice spacing ( $d$ ) of the crystal as represented in **Figure 2.2**. X-rays are produced by bombarding a metal (typically Cu) with energetic electrons in a vacuum tube and, typically, monochromatic x-rays are selected. The electron cloud surrounding each atom in the crystal scatters the x-rays. When the path difference between the incident and diffracted beams is an integer multiple of the wavelength ( $n\lambda$ ), there will be constructive interference, and the diffracted intensity will be maximum. This is the basis of Bragg's law, and it relates the lattice spacing ( $d$ ) between the planes of atoms where diffraction is occurring to the angle ( $\theta$ ) which is the angle between the incident and outgoing beams to the plane of atoms. For a monochromatic x-ray beam, according to Bragg's law, constructive interference should follow,

$$n\lambda = 2d\sin\theta \quad (2.2)$$

Experimentally, using a diffractometer, the angle  $2\theta$  is measured, and  $n$  is the order of the diffraction peak. The crystal works as a 3D diffraction grating. So, if the sample or the diffractometer is moved, a 3D array of diffraction maxima can be probed. Each set of crystal planes will produce a diffraction spot; the position and shapes of the diffraction spots are inversely related to the spacing of the planes and size of the crystallites. The crystal spacing is related to the real space and the diffraction spots with reciprocal space, thereby forming a 3D reciprocal lattice. In reciprocal space, each spot represents a crystal plane. To construct a reciprocal lattice from a crystal, each point associated with each lattice plane are plotted. This is done by choosing an origin and drawing a vector,  $Q$ , which is pointed outward from the origin and in the direction of the normal of that particular set of crystal planes. The magnitude of this vector,  $|Q| = 1/d$ , where  $d$  is the interplanar lattice spacing<sup>29</sup>. To construct the whole space, a point is plotted at the endpoint of the vector and is repeated for each set of planes until an entire reciprocal space has been created. Consequently, the direction remains the same in both real and reciprocal space, but distances are inverted. For example, in reciprocal lattice space in **Figure 2.3**, if, for instance, there is an increase in in-plane strain, it will cause the out of plane (0002) interplanar distance in the GaN lattice to decrease; i.e., shift toward the origin (following the crystals Poisson response).

Diffraction spots in 3D reciprocal space are shown in **Figure 2.3**, where the scattering vector  $Q = K_h - K_0$ , where  $K_h$ , and  $K_0$  are incident and diffracted beams, respectively. The scattering vector,  $Q$ , can be a ‘probe’ used to evaluate reciprocal lattice, and its length can be altered by changing the angle  $2\theta$ . By varying  $\omega$ , the angle at which

the incident beam meets a crystal plane, a different direction and orientation of  $Q$  can be probed. For a plane that is not parallel to the substrate, the value of  $\omega$  would differ from that of  $\theta$ . Therefore, it is useful to think of the reciprocal space always following the real crystal and if the crystal is moved with respect to the incident beam, so does the reciprocal space, accordingly. Therefore, different areas of reciprocal space can be investigated, either by altering the crystal orientation or by changing the length of the probe,  $S$ , by changing the angles  $\omega$  and  $2\theta$ .<sup>29</sup>

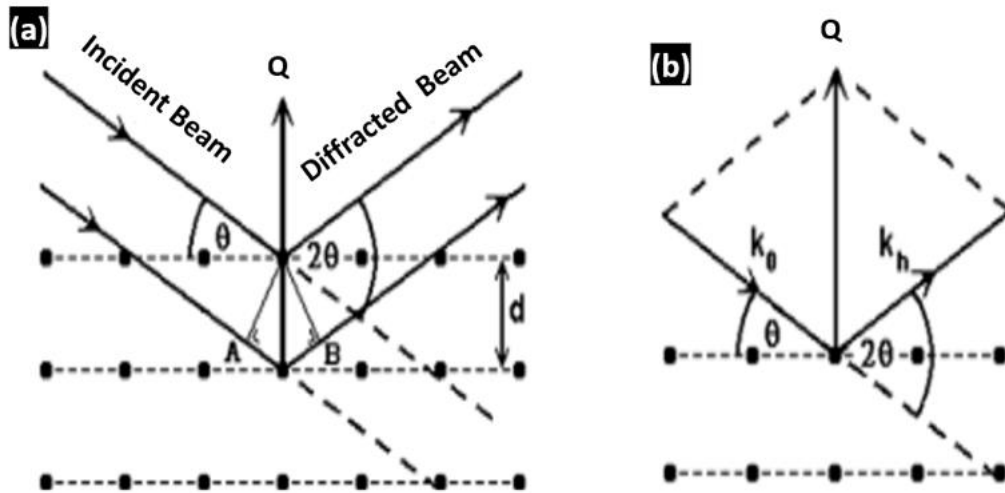


Figure 2.2 Schematic of x-ray diffraction. (a) Requirement for Bragg diffraction. (b) Relationship between incident ( $K_0$ ) and diffracted ( $K_h$ ) beam to the diffraction vector,  $Q$ . Dotted lines represent the atomic planes which may not be parallel to the sample surface. Figure 2 is recreated from an earlier report by Moram et al.<sup>29</sup>

The Ewald sphere construction is often used to illustrate reciprocal space, as shown in **Figure 2.3**. The same vectors are shown along with a sphere of radius  $1/\lambda$  (centered at the start of the incident beam vector,  $k_0$ ). This sphere shows which part of reciprocal space can be explored with  $Q$ , for a given wavelength  $\lambda$  and angle  $\theta$ . As  $\theta$  increases, the length of the scattering vector,  $Q$ , increases up to a maximum possible length of  $2/\lambda$  (i.e., twice

the length of the incident vector  $k_0$ ). Where the sphere touches a spot, diffraction occurs. For a reciprocal lattice space such as represented in **Figure 2.3**, not all the points can be accessed. For a given  $\lambda$  and maximum  $\theta$  value, the indicated outer circle limits the accessible points.

On the other hand, an offset in  $\omega$  can be applied (offset =  $\theta \pm \phi$ ), but the grey areas indicated in **Figure 2.3** are the regions where the sample itself will block the incident or the outgoing beam. However, if an alternate geometry can be used, then the shaded region may be accessible through transmission geometry (i.e., through the sample crystal). Most commonly, to access spots that are out of the page, as indicated in **Figure 2.4**, the sample is rotated  $90^\circ$  about  $\phi$ , and a  $\chi$  offset is used to give a skew symmetry. For any asymmetric lattice point for which  $\theta \neq \omega$ , an appropriate  $\omega$  can be achieved by either changing  $\omega$  by adding the angle between the surface normal of the epilayer to the surface normal of the asymmetric plane,  $\phi$ . This can be done by either keeping the incident angle  $\omega = \theta$  but adjusting  $\chi$  by  $\chi = \phi$  or keeping  $\chi = 0$  but adjusting the  $\omega$  as  $\omega_i = \theta + \phi$ , known as grazing exit geometry (GE), or  $\omega_e = \theta - \phi$ , known as grazing-incident geometry (GI). These offsets are calculated using standard equations for interplanar angles  $\phi$  and interplanar distance<sup>39</sup>  $d$  as represented in **Table 2.1**. (h'i'k'l') are the corresponding Miller indices for the associated asymmetric planes and  $d'$  (h'i'k'l') is the interplanar distance.

GE vs. GI geometry is also equivalent to mirror planes, for example, (10-14) to (-1014)<sup>39</sup>. Either geometry may be used and the choice depends on the measurement set-up because, depending on the incident angle, the x-ray beam penetration in the sample is different<sup>40</sup> and the diffracted beam could be either broadened or shortened. <sup>29 40</sup>

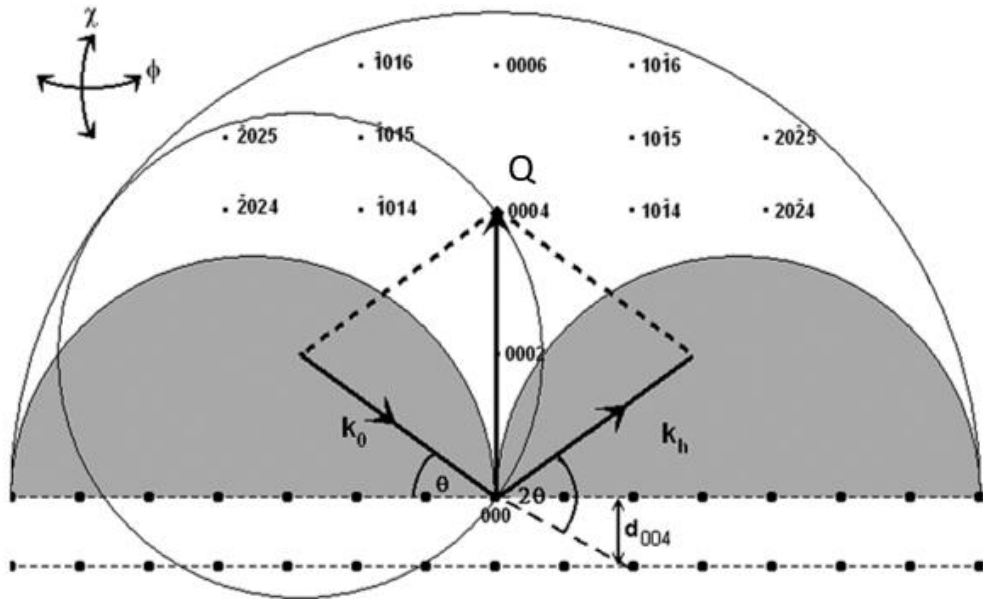


Figure 2.3 A section through reciprocal space for [0001] oriented GaN. The shaded regions are reciprocal spaces where the beam are blocked.  $K_0$  and  $K_h$  have a length of  $(1/\lambda)$ , where  $\lambda$  is the x-ray wavelength. The figure is recreated from Moram et al.<sup>29</sup>

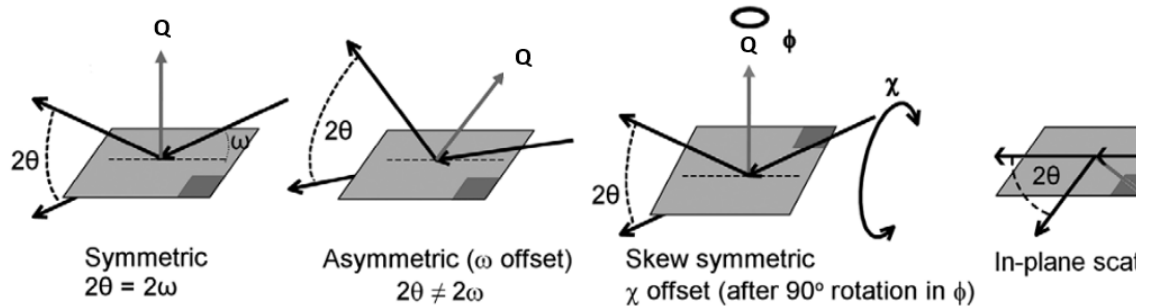


Figure 2.4 Various diffraction geometries. The figure is recreated from Moram et al.<sup>29</sup>

Table 2.1 Calculated Bragg's angles ( $2\theta$ ) for different accessible asymmetric planes, corresponding inclination angles ( $\phi$ ) from the surface normal, and calculated symmetric & asymmetric incident angles  $\omega_i = \theta + \phi$  &  $\omega_e = \theta - \phi$  for grazing exit (GE) and grazing incident (GI) geometry.

		Interplanar Angle	Bragg Angle	Symmetric Incident Angle	GE	GI
(h'i'k'l')	d'(h' i' k' l')	$\phi$	$2\theta$	$\theta = \omega$	$\omega_i = \theta + \phi$	$\omega_e = \theta - \phi$
1 0 -1 4	0.1174	25.14	82.03	41.15	66.16	15.87
1 0 -1 5	0.0971	20.58	104.97	52.49	73.07	31.90
1 0 -1 6	0.0825	17.37	138.04	69.02	86.39	51.64
2 0 -2 4	0.0945	43.19	109.14	54.56	97.76	11.37
2 0 -2 5	0.0829	36.91	136.46	68.23	105.14	31.32
1 1 0 4	0.1006	39.11	99.92	49.46	89.07	10.85
0 0 0 2	0.2592	0	0		0	0

## 2.2.2 Determination of AlN composition in $\text{Al}_x\text{Ga}_{1-x}\text{N}$ for partially- or fully-strained layers

Typically, RSM data are presented in a contour representation of diffraction intensity in reciprocal space coordinates,  $Q_{(hkl)_z}$  and  $Q_{(hkl)_x}$ . Peak positions in this coordinate system are readily converted into interplanar spacing ( $d_z$ ,  $d_x$ ), and, hence, the lattice constants ( $c$ ,  $a$ ). The reciprocal lattice vector  $Q_{(hkl)}$  for a given hkl plane is defined in terms of interplanar spacing  $d_{hkl}$  and lattice parameters  $a$  and  $c$  as follows,

$$Q_{(hkl)} = \frac{1}{d_{hkl}} = \sqrt{\frac{4(h^2+k^2+hk)}{3a^2} + \frac{l^2}{c^2}} \quad (2.3)$$

Now, for a given reciprocal lattice point with hkl index, the out-of-plane (along  $c$ -axis) and in-plane (along  $a$ -axis) reciprocal lattice vectors can be expressed as,

$$Q_{(hk0)_x} = \frac{1}{d_{(hk)_x}} = \sqrt{\frac{4(h^2+k^2+hk)}{3a^2}} \quad (2.4)$$

And

$$Q_{(00l)z} = \frac{1}{d_{(hkl)z}} = \frac{l}{c} \quad (2.5)$$

Thus, symmetric GaN (0002) and asymmetric (10-14), (10-15) and (20-25) reflections can be expressed as,

$$Q_{(104)x} = \frac{1}{d_{(100)x}} = \frac{2}{\sqrt{3}} \frac{1}{a} \quad (2.6)$$

$$Q_{(104)z} = \frac{1}{d_{(004)z}} = \frac{4}{c} \quad (2.7)$$

$$Q_{(105)x} = \frac{1}{d_{(100)x}} = \frac{2}{\sqrt{3}} \frac{1}{a} \quad (2.8)$$

$$Q_{(105)z} = \frac{1}{d_{(005)z}} = \frac{5}{c} \quad (2.9)$$

$$Q_{(205)x} = \frac{1}{d_{(200)x}} = \frac{4}{\sqrt{3}} \frac{1}{a} \quad (2.10)$$

$$Q_{(205)z} = \frac{1}{d_{(005)z}} = \frac{5}{c} \quad (2.11)$$

$$Q_{(002)z} = \frac{1}{d_{(002)z}} = \frac{2}{c} \quad (2.12)$$

From the above expressions, the  $a$  and  $c$  lattice constants can be determined for all epitaxial Al(Ga)N layers including AlN and GaN using  $Q_{(hkl)x}$ , and  $Q_{(hkl)z}$  coordinates.

For unstrained or partially strained thick ( $>$  critical thickness)  $\text{Al}_x\text{Ga}_{1-x}\text{N}$  layers, such as TL1 and TL2, a single diffraction measurement, e.g.  $c$  lattice constant, and Vegard's Law<sup>41</sup> are sufficient for determining the AlN composition ( $x$ ). Vegard's law<sup>41</sup> states that the lattice parameter of any alloy will vary linearly between the end constituents. To find  $x = \text{Al}\%$ , the  $a$  and  $c$  lattice parameters, according to Vegard's law, are

$$c_{AlGaN}(x) = xc_{AlN} + (1 - x)c_{GaN} \quad (2.13)$$

$$\text{Or } x = \frac{c_{AlGaN} - c_{GaN}}{c_{AlN} - c_{GaN}} \quad (2.14)$$

With this equation, one can easily solve for  $x$ , given that the lattice parameters for fully relaxed GaN, AlN ( $c_{AlN}$ ,  $c_{GaN}$  &  $a_{AlN}$ ,  $a_{GaN}$ ) and AlGaN layers ( $c_{GaN}$  &  $a_{AlN}$ ) are measured. Vegard's law is reliable for these alloys since the lattice mismatch between AlN and GaN is less than 2%.<sup>29</sup>

Uniaxial strain can be calculated from the following equations,

$$\text{In-plane strain,} \quad \varepsilon_{xx} = \frac{(a_m - a_0)}{a_0} \quad (2.15)$$

$$\text{Out of plane strain,} \quad \varepsilon_{zz} = \frac{(c_m - c_0)}{c_0} \quad (2.16)$$

Here,  $a_0$ , and  $c_0$  are the relaxed lattice constants from literature, given in **Table 2.2**, and  $a_m$  and  $c_m$  are the measured lattice parameters from HRXRD.

For a fully strained  $Al_xGa_{(1-x)}N$  layer, where  $x$  is unknown, and using Vegard's Law to express the relaxed alloy lattice parameters and elastic constants ( $C_{ij}$ ), the in-plane and out-of-plane strain relation can be written as,<sup>42,36</sup>

$$\varepsilon_{zz} = -D \times \varepsilon_{xx} \quad (2.17)$$

$$\varepsilon_{zz} = -\frac{2\nu}{1-\nu} \varepsilon_{xx} = -\left(\frac{2C_{13}}{C_{33}}\right) \times \varepsilon_{xx} \quad (2.18)$$

The above relationship can be rewritten as follows,

$$\frac{c_m(x) - c_0(x)}{c_0(x)} = \frac{-2C_{13}}{C_{33}} \times \frac{a_m(x) - a_0(x)}{a_0(x)} = -\frac{2\nu(x)}{1-\nu(x)} \times \frac{a_m(x) - a_0(x)}{a_0(x)}, \quad (2.19)$$

Here, “ $c(x)$ ” and “ $a(x)$ ” are the c-axis and a-axis lattice parameters, respectively. The subscripts “ $m$ ” and “ $0$ ” refer to the measured and relaxed lattice parameters, respectively.  $\nu$  is Poisson’s ratio,  $C_{13}$  and  $C_{33}$  are the components of the elastic stiffness tensors.

Where,

$$\nu(x) = x\nu_{AlN} + (1 - x)\nu_{GaN} \quad (2.20)$$

$$C_0(x) = xC_0^{AlN} + (1 - x)C_0^{GaN} \quad (2.21)$$

$$a_0(x) = xa_0^{AlN} + (1 - x)a_0^{GaN} \quad (2.22)$$

$$\frac{c_m(x) - [xC_0^{AlN} + (1-x).C_0^{GaN}]}{[xC_0^{AlN} + (1-x).C_0^{GaN}]} = \frac{-2[xC_{13}^{AlN} + (1-x).C_{13}^{GaN}]}{[xC_{33}^{AlN} + (1-x).C_{33}^{GaN}]} \times \frac{a_m(x) - [xa_0^{AlN} + (1-x).a_0^{GaN}]}{[xa_0^{AlN} + (1-x).a_0^{GaN}]}, \quad (2.23)$$

By considering  $x$  as a rational fraction, the above equations reduce to a simple third order polynomial as,

$$Ax^3 + Bx^2 + Cx + D = 0, \quad (2.24)$$

Where, A, B, C, and D are coefficients.

The measured lattice parameters  $c_m(x)$  were determined from RSM around the GaN (0002) reflection and lattice parameters  $a_m(x)$  from RSM around the GaN (10-14), (10-15) and (20-25) reflections. (For examples, refer to **Figures 2.8-2.10.**) By solving Eq. (2.24), the AlN mole fraction for the fully strained AlGaN barrier layer can be determined.

Table 2.2 Relaxed lattice parameters for AlN and GaN and corresponding elastic constants.<sup>43</sup>

	$a_0$	$c_0$	$C_{13}$	$C_{33}$	$C_{11}$	$C_{12}$	Poisson's ratio
GaN	3.189	5.186	$106 \pm 20$	$398 \pm 20$	$390 \pm 15$	$145 \pm 20$	0.210
AlN	3.112	4.982	$108 \pm 5$	$373 \pm 10$	$396 \pm 10$	$137 \pm 10$	0.224

### 2.2.3 Bi-axial stress from HRXRD

By determining the exact  $x$  value for the strained barrier layer,  $\varepsilon_{xx}$  and  $\varepsilon_{zz}$  can be determined. Strain in III-Nitride layers may be composed of hydrostatic ( $\varepsilon^h$ ) and biaxial ( $\varepsilon_{ii}^b$ ) components<sup>36,44,45</sup>, where  $i$  represents direction;  $x$  or  $z$ . Due to the significantly different covalent radii of the Ga and the N atoms, GaN is prone to native defect formation.<sup>44</sup> It is well known that GaN-on-Si grown by MOCVD contains a significant concentration of point defects which can affect the lattice parameters through local expansion or contraction (depending on the density and types of point defects), thereby causing hydrostatic strain in the crystal.<sup>46</sup> The hydrostatic strain can be quantified using  $\varepsilon_h = \frac{\Delta c}{c_0} = \frac{\Delta a}{a_0} = bC$ , where  $b$  is an expansion (contraction) factor for an individual defect and  $C$  is their concentration.<sup>44</sup> For heterostructure epitaxial growth (e.g., AlGaIn/GaN on Si or diamond on GaN) biaxial strain is induced in the Al(Ga)N layers due to the lattice mismatch between layers and different TECs.<sup>42,44,46</sup> Therefore, to better understand the true nature of the strain and the material quality before and after diamond growth, these strain components are considered. Uniaxial in-plane and out-of-plane strain can be expressed as a linear combination of biaxial strains ( $\varepsilon_{zz}^b, \varepsilon_{xx}^b$ ), along  $c$  and  $a$  directions, respectively, and hydrostatic strain  $\varepsilon_h$  as follows [38],[40],

$$\varepsilon_{zz} = \varepsilon_{zz}^b + \varepsilon_h \quad (2.23)$$

$$\varepsilon_{xx} = \varepsilon_{xx}^b + \varepsilon_h \quad (2.24)$$

Considering both biaxial and hydrostatic strain contributions, the strain relation can be rewritten as follows,<sup>44</sup>

$$\varepsilon_{zz} = \frac{c-(c_0-\Delta c)}{c_0-\Delta c}, \text{ and} \quad (2.25)$$

$$\varepsilon_{xx} = \frac{a-(a_0-\Delta a)}{a_0-\Delta a} \quad (2.26)$$

From the strain relation and rearranging the above equation, the hydrostatic strain can be expressed in terms of uniaxial strain and Poisson's ratio by the following expression,

$$\varepsilon_h = \frac{1-\nu}{1+\nu} (\varepsilon_{zz} + \frac{2\nu}{1-\nu} \varepsilon_{xx} ). \quad (2.27)$$

Using the lattice parameters and elastic constants shown in **Table 2.2**, the strains are evaluated for sample SG1, SG2 & CG. The corresponding in-plane biaxial stress  $\sigma_{bs}$  in the III-Nitride layers can be expressed in terms of biaxial strain and biaxial elastic modulus,

$$M_f = C_{11} + C_{12} - 2 \frac{C_{13}^2}{C_{33}}$$

$$\sigma_{bs} = M_f \varepsilon_{xx}^b \quad (2.28)$$

Here,  $C_{ij}$  are the elastic constants of the corresponding III-Nitride layers.

#### 2.2.4 Bi-axial Stress from Raman

The  $E_2^2$  peak positions in GaN and AlN layers are sensitive to stress<sup>37,44</sup>. GaN is transparent to visible light and as such, excitation from the 532 nm visible laser provides an average stress profile for the entire GaN buffer layer. Peak positions ( $\omega$ ) and line width are determined by fitting the data using a Lorentzian function. Relaxed GaN and AlN

reference peaks are determined to be GaN  $E_2^2$   $\omega_0 = 568.24 \text{ cm}^{-1}$  and AlN  $E_2^2$   $\omega_0 = 656.72 \text{ cm}^{-1}$ . Biaxial stress  $\sigma_{xx}$  values are determined using the following equation<sup>37</sup>

$$\sigma_{xx} = \Delta\omega/K_R = (\omega - \omega_0)/K_R \quad (2.29)$$

where,  $K_R$  is the Raman stress factor. For the  $E_2^2$  phonon,  $K_R^{E_2^2} = -3.4 \pm 0.3 \text{ cm}^{-1}/\text{GPa}$  was used<sup>4849</sup>. **Table 2.4** tabulates the residual biaxial stress along the  $a$ -axis in the GaN and AlN layers.

### 2.3 Results and Discussion

To evaluate the AlGaIn/GaN HEMT surface morphology grown with different transition layer schemes tapping mode AFM was performed, as shown in **Figure 2.5**. **Figure 2.5(a)** shows the top GaN (cap) surface morphology with the two-step graded transition layer (SG1), (b) shows the surface of SG2 sample and (c) shows the surface morphology of continuous graded (CG) transition layers. Characteristic AlGaIn/GaN HEMT morphology is observed. The RMS roughness from these  $1 \mu\text{m} \times 1 \mu\text{m}$  scans are 0.20 nm for SG1 and SG2, and 0.15 nm for CG. Further comparative analysis of the AFM data indicates that adding the extra transition layer in SG2 has reduced the surface pitting texture. Furthermore, for the CG transition layers, the defects are minimum. This could be due to the additional transition layers providing better TEC and lattice mismatch and, thereby, better accommodating the strain which would result in less strain in the GaN buffer layer thereby reducing the dislocation defects threading from the buffer.

**Figure 2.6** shows the specular XRR reflection spectra for the AlGaIn/GaN heterostructures. For samples SG1, SG2, and CG, well defined periodic Kiessing fringes are observed.<sup>29</sup> Since periodicity of the fringes directly relates to the thickness of each

constituent layer, a Fast Fourier Transform (FFT) of the spectrum resolves the individual contribution of each layer. Using Rigaku's GlobalFit software, which incorporates both optimization (Extended Fourier Transform) and refinement (least-square) of the layer parameters, thicknesses, interface roughness, and material density of each layer is estimated.<sup>50</sup> The thickness of the barrier layers was found to be  $17 \pm 1$  nm for SG1 and  $18 \pm 1$  nm for both SG2 and CG. All samples exhibit identical peak reflection intensities which indicates the surface layers are comprised of substantially the same material.

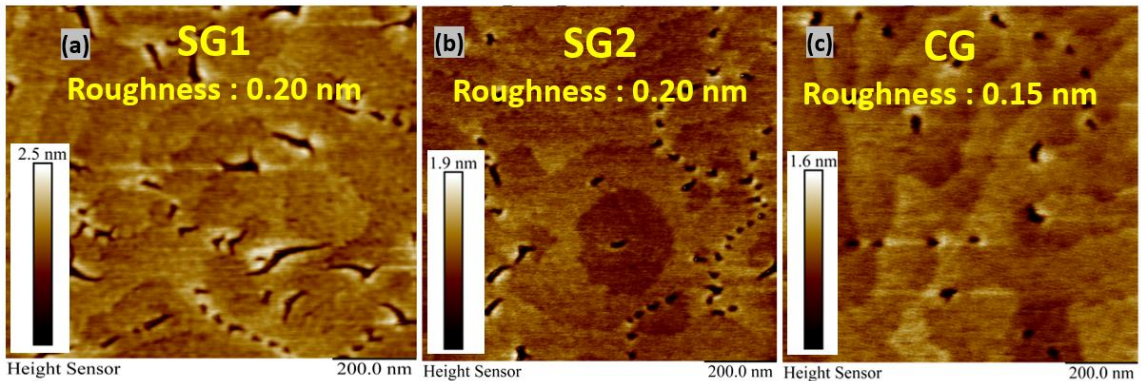


Figure 2.5 Measured and simulated grazing incidence Figure 2.6 2D AFM images of  $1 \mu\text{m} \times 1 \mu\text{m}$  GaN/(cap)AlGaIn(barrier)/AlN(profile)/GaN(buffer) surface confirming the smooth GaN cap surface with atomic step flow

For high-performance AlGaIn/GaN HEMTs, it is highly beneficial that the GaN buffer layer is strain free and fully relaxed. For heteroepitaxial growth of GaN-on-Si, the challenge is to minimize the TEC mismatch and lattice mismatch between the AlN nucleation layer to the GaN buffer layer. A smooth, continuous transition from the nucleation layer to the GaN buffer should reduce the strain in GaN thereby ensuring the strain-free buffer layer. To measure the impact of the different transition layer schemes on the AlGaIn/GaN HEMT in view of the stress-strain state of the GaN buffer, HRXRD based RSM was performed. x-ray reflectivity data for the three experimental transition

layer structures. Figure 2. 7 Measured and simulated grazing incidence x-ray reflectivity data for the three experimental transition layer structures.

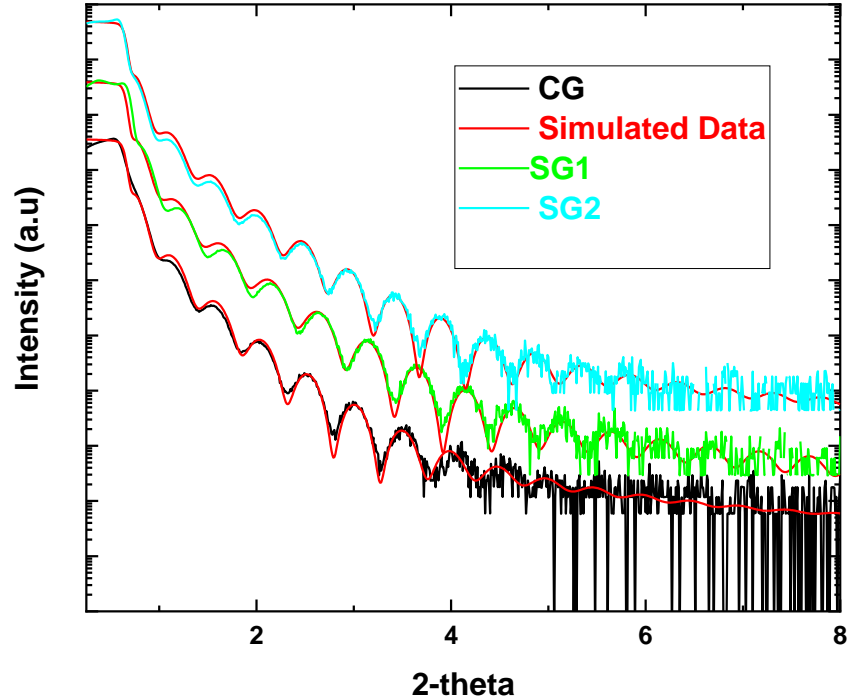


Figure 2. 6 Measured and simulated grazing incidence x-ray reflectivity data for the three experimental transition layer structures.

**Figure 2.7** shows the RSMs around the GaN symmetric (0002) reflection. The data are presented in a contour plot in reciprocal coordinates  $Q_x$  and  $Q_z$ . The color schemes show the variation in the intensity of the diffracted beam, with red representing the highest diffraction intensity while blue represents the lowest. Clear and distinct reciprocal points are observed for the binary AlN and GaN layers, and all the transition layers (TL0, TL1 & TL2) for sample SG1, **Figure 2.7(a)**, and SG2, **Figure 2.7(b)**. These data confirm the compositions of the various step graded transition layers. For sample CG, **Figure 2.7(c)**, the contour plot shows a continuous peak which starts from AlN and continues to the GaN buffer layer and confirms a continuous alloy transition for  $Al_xGa_{1-x}N$  from  $x = 100$  to  $x = 0$ . **Table 2.3** represents the out of plane lattice constant  $c$  determined from Eq-(2.5) and the

AlN composition in  $\text{Al}_x\text{Ga}_{(1-x)}\text{N}$  transition layers from equation Eq-(2.14). For SG1 and SG2, TL1's AlN% is  $x = 0.52$  &  $0.50$ , respectively, and TL2's AlN% is  $x = 0.28$  &  $0.26$ , while TL0's AlN% is  $x = 0.75$ .

Table 2.3 Out-of-plane lattice constant  $c$  and transition layer composition determination from RSM around the GaN symmetric (0002) reflections.

	SG1		SG2		CG	
	$c$	Al % = $x$	$c$	Al% = $x$	$c$	Al% = $x$
<b>AlN</b>	4.972		4.971		4.971	
<b>AlGaN(TL0)</b>			5.023	0.75		
<b>AlGaN(TL1)</b>	5.073	0.52	5.076	0.50		
<b>AlGaN(TL2)</b>	5.125	0.28	5.127	0.26		
<b>GaN</b>	5.184		5.182		5.183	

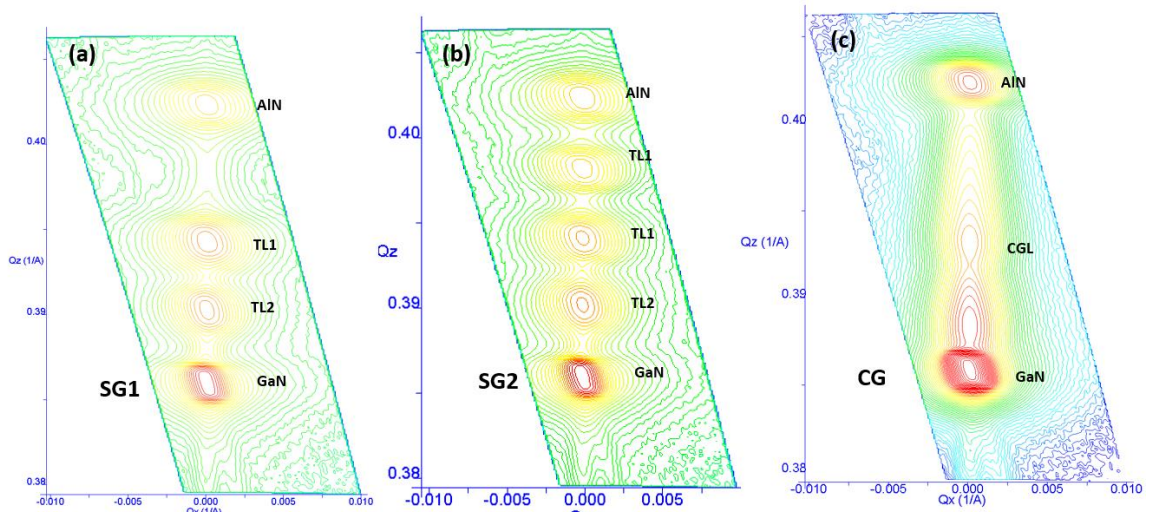


Figure 2. 8 RSM contour plots of the AlGaN/GaN HEMT wafers with AlN, GaN, TL0 ( $\text{Al}_{0.75}\text{Ga}_{0.25}\text{N}$ ), TL1 ( $\text{Al}_{0.51}\text{Ga}_{0.49}\text{N}$ ), TL2 ( $\text{Al}_{0.26}\text{Ga}_{0.74}\text{N}$ ) and barrier layer ( $\text{Al}_{0.27}\text{Ga}_{0.73}\text{N}$ ) peaks collected around their symmetric (0002) reflections. (a) Step graded transition layer stack 1 (SG1) (b) Step graded transition layer stack 2 (SG2) (c) continuous graded transition layer (CG). The axes are converted to  $Q_z$  and  $Q_x$  reciprocal coordinates ( $Q_z = 1/d_z$ ;  $Q_x = 1/d_x$ ). The color schemes show the variation in the intensity of the diffracted beam, with red represents the highest diffraction intensity while blue represents the lowest.

Since the strained AlGaN barrier layer has similar AlN composition to TL2 ( $\text{Al}_{0.26}\text{Ga}_{0.74}\text{N}$ ), neither the symmetric (0002) HRXRD or RSM scans can independently resolve the barrier layer as they have nearly identical interplanar spacings along the  $c$ -axis. Therefore, RSM around the asymmetric (10-14), (10-15) and (20-25) reflections was performed to analyze the strained AlGaN barrier layer. Using the strain sensitive RSM, the thin (20 nm) AlGaN barrier layer can be independently measured and the impact of the different transition layer schemes on the GaN buffer and the barrier layer characteristics can be accurately ascertained. The composition of the barrier layer determines the band offset and spontaneous polarization while the tensile strain in the barrier layer determines the piezoelectric polarization and, thus, the total induced 2DEG sheet charge density in the AlGaN/GaN heterostructure. Thus, the exact quantification of these parameters is of utmost important to accurately predict the electrical performance of the AlGaN/GaN HEMT.

**Figure 2.8** presents the HRXRD RSM data around the GaN (10-14) reflections (a) SG1, (b) SG2 and (c) CG. **Figure 2.9** presents the HRXRD RSM data around the GaN (10-15) reflections (a) SG1, (b) SG2 and (c) CG. **Figure 2.10** presents the HRXRD RSM data around the GaN (20-25) reflections (a) SG1, (b) SG2 and (c) CG. The XRD goniometer was first normalized to the GaN asymmetric peaks using a GE geometry for (10-14) and (10-15) and adjusting the incident beam angle by adding the angular distance from the surface normal to the asymmetric reflections as described in the previous sections (see **Table 2.1**). For the GaN (20-25) reflection GI geometry was used. The vertical dotted line in each panel represents the zero-relaxation line along the GaN  $a$ -axis. For any layer grown pseudomorphically on GaN, its peak will lie on the zero-relaxation line. For (10-14) and (10-15) reflections the diffraction peaks for AlN, TL0, TL1, and TL2 lie on the right side

of the zero-relaxation line corresponding to partially or fully relaxed layers. On the other hand, for (20-25) reflection these peaks lie on the left side of the zero-relaxation line. This is because due to GI geometry, the accessible reflections are mirror planes to those accessed in GE geometry. Because the asymmetric reflections are very sensitive to the strain state, the fully strained pseudomorphically grown AlGaN barrier layer diffraction peak is clearly separated from the TL2 peak and lattice matched to the GaN buffer along  $Q_x$  (the  $a$ -axis). The thin barrier layer ( $< 20$  nm) peak's vertical spread is expected for a pseudomorphically grown thin film.<sup>29</sup> Distinct barrier layer peaks are visible in all scans given in **Figures 2.8-2.10**, (highlighted within the dotted ellipse indicated on each figure). The exact determination of in-plane,  $a$ , and out-of-plane lattice parameter,  $c$ , allows accurate evaluation of the barrier layer's structural properties. The barrier layer lattice parameters  $a$  and  $c$  are calculated from the peak position in the reciprocal space. These parameters are then substituted into equations Eq-2.17-2.23. For the (10-14) and (10-15) reflections, the relaxed  $c$  lattice parameters for AlN and GaN are taken from the symmetric (0002) measurement as presented in the **Table 2.2**. Finally, the 3<sup>rd</sup> order polynomial Eq-2.24 is solved to determine the real root  $x$ , and thereby determine the barrier layer AlN composition. In the case of the (20-25) reflection, all lattice parameters for both binary layers (AlN & GaN) and the ternary (AlGaN barrier) layer are taken from the RSM scan (**Figure 2.10**).

Uniaxial strains  $\varepsilon_{zz}$  and  $\varepsilon_{xx}$  are calculated from the measured parameters using equations Eq 2.13 & 2.14. The hydrostatic strain ( $\varepsilon_h$ ) components are determined from Eq 2.27 and the biaxial strain along the x-axis  $\varepsilon_{xx}^b$  is determined using Eq 2.24 as tabulated in **Table**

**2.4.** Finally, biaxial stresses are calculated using equation Eq 2.29 (see **Table 2.4**). The elastic constants are taken from previously reported values, presented in **Table 2.2**.

From the (10-14) and (10-15) reflection data, biaxial strain in the barrier layer is higher than that of GaN and AlN. This is because the thin (<20 nm) barrier layer is pseudomorphically grown on GaN and is fully strained. On the other hand, the strain in AlN is also higher than GaN. This is because AlN is grown directly on Si which has a substantial lattice mismatch with AlN, compared to the GaN buffer layer that is grown on the strain engineered transition layer schemes. Biaxial stress values, which are directly correlated to strain values, follow the same trend. SG1 has two transition layers whereas with SG2, an additional transition layer (TL0, with  $x = 0.75$ ) was engineered to ensure a more gradual transition from AlN, compare to SG1. From the stress-strain values shown in **Table 2.4** it is evident that the GaN stress in SG2 has reduced by 40% - 50% compared to SG1 (i.e., from 0.66 to 0.48 GPa). Furthermore, for CG where a continuous graded transition layer is employed, the GaN buffer strain has further reduced to the point that it is fully relaxed compared to SG1 and SG2. These HRXRD trends are consistent with the GaN and AlN stress data from visible Raman measurements, also shown in **Table 2.4**. The AlN nucleation layer exhibits consistent stress values for all transition layer structures and is confirmation of the validity of the different measurement approaches. The variation in the XRD and Raman stress values arise from the fact that the Raman stress factor used here (3.4 GPa/cm) is obtained from a reported value<sup>38</sup> and not from these samples. Discrepancies in the reported stress factors and elastic coefficients may be attributed to differences in defect densities in the III-Nitride layers investigated by the different

researchers, which has an impact on the strain values, particularly  $\varepsilon_h$ , and Poisson's ratio.<sup>44,51</sup>

For the (20-25) reflection data as presented in **Figure 2.10** lattice parameters, Al compositions, strain relaxation and corresponding biaxial stresses in the barrier layer is evaluated as presented in **Table 2.4**. The AlN and GaN buffer layer lattice parameters are also evaluated. While the composition of the barrier layer determined shows consistent but slightly higher Al% for all the stack compare to (10-14) and (10-15), the bi-axial stress values even for the binary partially relaxed (AlN and GaN) layers are inconsistent compare to the Raman stress result. The evaluated stresses as shown in Table 4.2 are of compressive in nature. The inconsistency in the stress values could come from the fact that GaN (20-25) reflection is strain invariant and are not sensitive bi-axial stress.<sup>31,52</sup>

To ascertain the confidence in the measured and calculated parameters, an uncertainty analysis was performed considering several different sources of uncertainty while determining the RSM peak positions. For the SmartLab Rigaku system with an optical precision  $\leq 4$  arcsec, the instrumental contribution to the uncertainty in determining the 2-theta position (and interplanar spacing) is negligible. However, uncertainty arises from the step size in  $\omega$ -space ( $0.03^\circ$ ). The maximum uncertainty is estimated using the half-width half-maximum (HWHM) of the GaN buffer layer peaks in reciprocal space. First, for biaxial strain, the biaxial stress uncertainty is 0.0004 GPa, or 0.06 % of the determined 0.66 GPa value (specifically, the biaxial stress of SG1 from the (10-14) reflection data).

Table 2.4. Comparison of stress-strain in GaN, AlN and fully strained AlGaIn barrier layer, and AlN composition in the barrier layer from different asymmetric reflections (10-14), (10-15) and (20-25) and visible Raman measurements.

		SG1			SG2			CG		
		Barrier	GaN	AlN	Barrier	GaN	AlN	Barrier	GaN	AlN
From (10-14) reflection	$a$ (Å)	3.188	3.193	3.124	3.191	3.191	3.123	3.183	3.185	3.118
	Biaxial strain ( $\epsilon_{xx}^b$ )%	0.68	0.16	0.39	0.64	0.10	0.36	0.43	-0.02	0.27
	AlN%	<b>27.9</b>			<b>26.9</b>			<b>24.8</b>		
	Biaxial stress (GPa)	<b>2.83</b>	<b>0.66</b>	<b>1.70</b>	<b>3.05</b>	<b>0.48</b>	<b>1.679</b>	<b>2.12</b>	<b>-0.12</b>	<b>1.37</b>
From (10-15) reflection	$a$ (Å)	3.188	3.188	3.119	3.186	3.189	3.121	3.179	3.183	3.115
	Biaxial strain ( $\epsilon_{xx}^b$ )%	0.585	0.023	0.276	0.577	0.066	0.331	0.364	-0.08	0.206
	AlN%	<b>27.9</b>			<b>28.5</b>			<b>24.7</b>		
	Biaxial stress (GPa)	<b>2.78</b>	<b>0.11</b>	<b>1.30</b>	<b>2.74</b>	<b>0.31</b>	<b>1.55</b>	<b>1.74</b>	<b>-0.41</b>	<b>0.96</b>
From (20-25) reflection	$a$ (Å)	3.152	3.153	3.086	3.154	3.154	3.088	3.153	3.155	3.091
	Biaxial strain ( $\epsilon_{xx}^b$ ) %	-0.24	-0.87	-0.61	-0.23	-0.82	-0.55	-0.31	-0.83	-0.49
	AlN%	<b>30</b>			<b>29.1</b>			<b>26.4</b>		
	Biaxial stress (GPa)	<b>-1.14</b>	<b>-4.14</b>	<b>-2.87</b>	<b>-1.1</b>	<b>-3.9</b>	<b>-2.54</b>	<b>-1.45</b>	<b>-3.99</b>	<b>-2.31</b>
<b>Vis Raman</b>	Biaxial stress (GPa)		<b>0.59</b>	<b>1.33</b>		<b>0.29</b>	<b>1.31</b>		<b>0.01</b>	<b>1.3</b>

The uncertainty resulting from the empirical values of the elastic constants ( $C_{11}$ ,  $C_{12}$ ,  $C_{13}$ ,  $C_{13}$ ) was also considered. Published elastic constants used here vary up to 19 % as reported in the literature by Vurgaftman *et al.*<sup>43</sup> and by Wright *et al.*<sup>53</sup>, as shown in **Table 2.2**. This results in a biaxial stress uncertainty of  $\pm 0.07$  GPa, which is 11 % of the determined GaN biaxial stress value of 0.66 GPa, given in **Table 2.4**. The barrier layer composition measured from the combination of the GaN symmetric (0002) and asymmetric (10-14) or (10-15) reflections are very close, while there is a consistent increase in the

AlN% in the (20-25) reflection data, as seen in **Table 2.4**. A proper comparison of these methods in terms of determining the composition could be made by comparing this non-destructive XRD based method to a direct physical quantization such as atomic probe tomography.

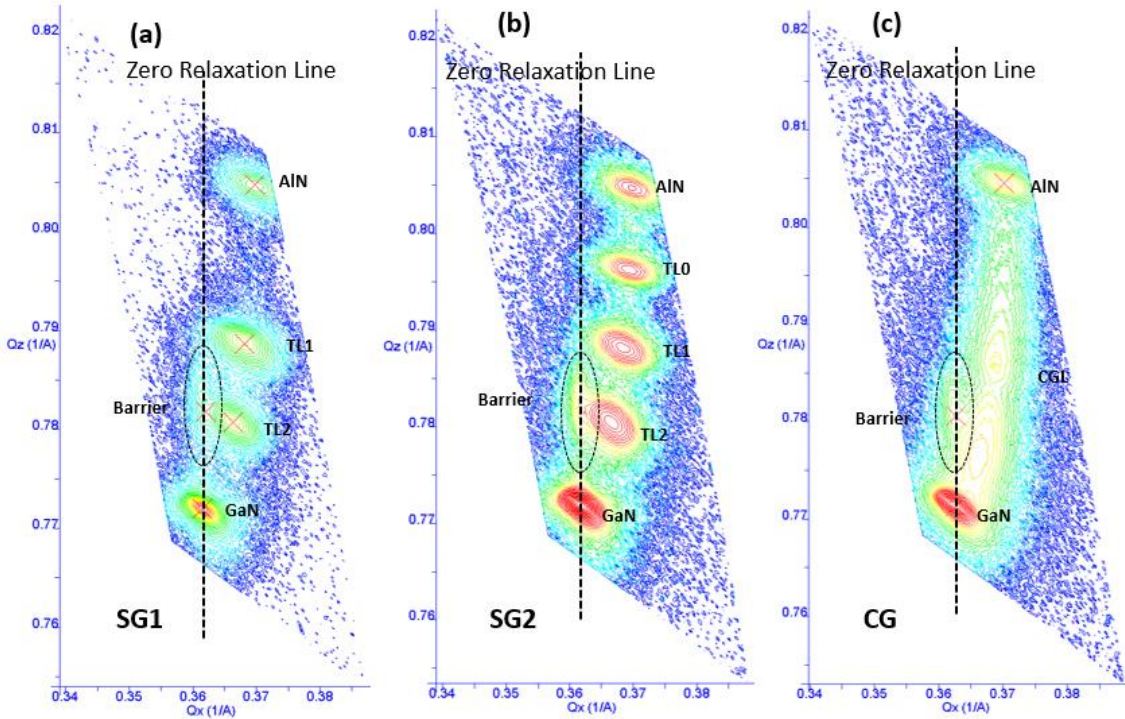


Figure 2.8 RSM contour plots of the AlGaN/GaN HEMT wafers with AlN, GaN, TL0 ( $\text{Al}_{0.75}\text{Ga}_{0.25}\text{N}$ ), TL1 ( $\text{Al}_{0.51}\text{Ga}_{0.49}\text{N}$ ), TL2 ( $\text{Al}_{0.26}\text{Ga}_{0.74}\text{N}$ ) and barrier layer ( $\text{Al}_{0.27}\text{Ga}_{0.73}\text{N}$ ) reflections collected around their asymmetric GaN (10-14) reflection. (a) Step graded transition layer stack 1 (SG1) (b) Step graded transition layer stack (SG2) (c) continuous graded transition layer (CG). The dotted line indicates the zero-relaxation line along the crystallographic  $a$ -axis. The dotted ellipses highlight the strained barrier layer peaks. The axes are converted to  $Q_z = 1/d_z$ ;  $Q_x = 1/d_x$ .

Due to the light mass of Al, this method should be preferred over secondary ion mass spectroscopy or Rutherford backscattering. As evidenced in **Table 2.4**, stress determination using the GaN (20-25) reflection does not correspond to the Raman stress data and is substantially different than the stresses calculated by the (10-14) and (10-15) reflections. Therefore, strain determination using this particular reflection is considered inaccurate. Furthermore, while both (10-14) and (10-15) reflections give reasonable stress-

strain values for AlN and GaN compared to Raman, in terms of determining structural properties, the (10-14) reflection is recommended over the (10-15) reflection. This is because RSM around the (10-14) reflection provides a more differentiated barrier layer peak that is fully separated from TL2, while for (10-15) there is a small overlap between them. One other benefit of using (10-14) is that the radial axis coverage is less than that of (10-15) which makes the scan faster, which is also true compared to the (20-25) data collection time.

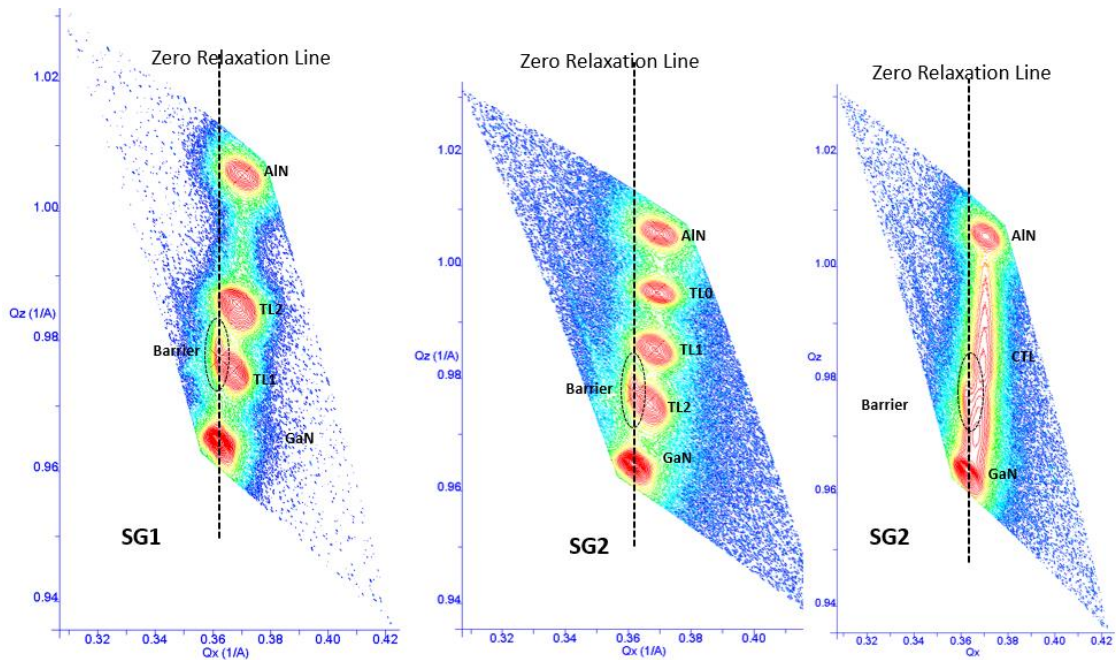


Figure 2.9 RSM contour plots of the AlGaN/GaN HEMT wafers with AlN, GaN, TL0 ( $\text{Al}_{0.75}\text{Ga}_{0.25}\text{N}$ ), TL1 ( $\text{Al}_{0.51}\text{Ga}_{0.49}\text{N}$ ), TL2 ( $\text{Al}_{0.26}\text{Ga}_{0.74}\text{N}$ ) and barrier layer ( $\text{Al}_{0.27}\text{Ga}_{0.73}\text{N}$ ) reflections collected around their asymmetric GaN (10-15) reflection. (a) Step graded transition layer stack 1(SG1) (b) Step graded transition layer stack 2(SG2) (c) continuous graded transition layer (CG). The dotted line indicates the zero-relaxation line along the crystallographic  $a$ -axis. The dotted ellipses highlight the strained barrier layer peaks.

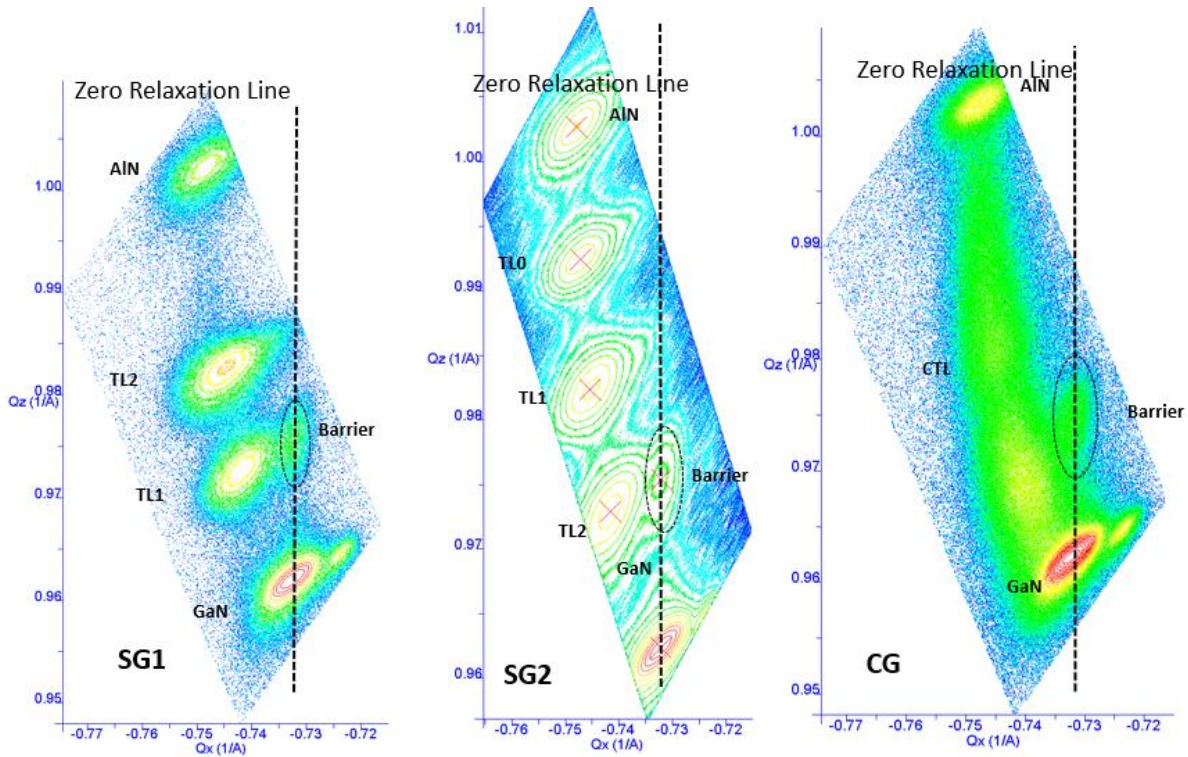


Figure 2.90 RSM contour plots of the AlGaIn/GaN HEMT wafers with AlN, GaN, TL0 ( $\text{Al}_{0.75}\text{Ga}_{0.25}\text{N}$ ), TL1 ( $\text{Al}_{0.51}\text{Ga}_{0.49}\text{N}$ ), TL2 ( $\text{Al}_{0.26}\text{Ga}_{0.74}\text{N}$ ) and barrier layer ( $\text{Al}_{0.27}\text{Ga}_{0.73}\text{N}$ ) reflections collected around their asymmetric GaN (20-25) reflection. (a) Step graded transition layer stack 1(SG1) (b) Step graded transition layer stack 2(SG2) (c) continuous graded transition layer (CG). The dotted line indicates the zero-relaxation line along the crystallographic  $a$ -axis. The dotted ellipses highlight the strained barrier layer peaks

As noted previously, the fully strained barrier layer's AlN composition may be determined using just the RSM scan around the (20-25) reflection. However, to calculate the barrier layer physical properties and, hence, the electrical properties of the AlGaIn/GaN HEMT, both AlN% and strain must be evaluated. By choosing only the (20-25) reflection, one would be restricted to compositional determination, only. In addition, the radial coverage for the (20-25) reflection is larger and requires a 0D detector (point detector) to reach the

high GI angle while the other reflections, (10-15) and (10-14), can be scanned using a 1D detector, which has a much faster scan rate than the 0D detector. For example, for an accurate RSM scan around (10-14) (as applied in this study) it takes about 2.5 hours, the (10-15) scan is somewhat longer at 3.5 hours, while for (20-25) the scan time is greater than 6 hours.

## **2.4 Conclusions**

In this chapter experiments involving AlGa<sub>N</sub>/Ga<sub>N</sub> HEMTs on 100 mm, low resistance Si (111) wafers with three different transition layer schemes are reported. The surface morphology of the AlGa<sub>N</sub>/Ga<sub>N</sub> HEMTs were evaluated using atomic force microscopy (AFM), and the thickness of the top surface layers was determined from x-ray reflectivity measurement. High resolution x-ray diffraction (HRXRD) characterization of the stress-strain state and Al composition of the fully strained barrier layer is evaluated using different combinations of symmetric and asymmetric reflections. Residual stress in binary AlN and GaN is also characterized using visible micro Raman measurement. Stress values determined from Raman were compared with different schemes of HRXRD measurements and it is found that reciprocal space mapping around the GaN (10-14) reflection is more reliable compared to other asymmetric reflections.

### 3 EFFECT OF REACTANT GAS STOICHIOMETRY OF *IN-SITU* SiN<sub>x</sub> PASSIVATION ON STRUCTURAL PROPERTIES OF MOCVD GROWN AlGa<sub>N</sub>/Ga<sub>N</sub> HEMTS

#### 3.1 Introduction

The AlGa<sub>N</sub>/Ga<sub>N</sub> heterostructure has two inherent polarization effects, namely spontaneous polarization due to electronegativity and lack of crystal inversion symmetry, and piezoelectric polarization due to lattice mismatch and thermal strain, discussed in the Introduction. Therefore, a high polarization induced electric field is generated within the wurtzite crystal, which creates a charge separation between surface and interface.<sup>23</sup> If a polarization induced 2DEG is created at the AlGa<sub>N</sub>/Ga<sub>N</sub> interface, a sheet of opposite charge is also created on the top surface of the AlGa<sub>N</sub> layer, making the HEMT device highly sensitive to the surface states and any modification of surface state filling.<sup>13</sup> Drain current collapse and DC-RF dispersion are two obstacles to producing high efficiency AlGa<sub>N</sub>/Ga<sub>N</sub> HEMT devices. As reported by R. Vetury et al.<sup>9</sup> and G. Meneghesso et al.<sup>10</sup> the virtual channel that is created by the surface states is the reason for the degradation and dispersion and can be successfully mitigated by passivating the III-Nitride surface.

Several studies regarding the benefits of *in-situ* SiN<sub>x</sub> as a passivating layer for AlGa<sub>N</sub>/Ga<sub>N</sub> over *ex-situ* passivation have been published.<sup>13,14,15</sup> Among the reports, Ma et al. investigated *in-situ* SiN<sub>x</sub> passivation at elevated temperature (1080 to 1145 °C) on AlN/Ga<sub>N</sub> HEMT<sup>15,54</sup>, while P. Gamarra et al. reported MOVPE grown *in-situ* SiN<sub>x</sub> on InAlGa<sub>N</sub>/Ga<sub>N</sub> HEMT at 875 °C<sup>55</sup>. While the effectiveness of the MOCVD grown *in-situ*

SiN<sub>x</sub> as a passivating layer has been established, there is a lack of detailed studies on the effect of constituent gas ratios on growth mechanisms of *in-situ* SiN<sub>x</sub> on AlGaN as well as the surface morphology and electrical properties, at typical AlGaN/GaN growth conditions.

In this chapter, *in-situ* SiN<sub>x</sub> grown by MOCVD at typical AlGaN/GaN growth temperature and pressure is reported. The effect of individual constituent reactant gases on the growth mechanism and morphology of SiN<sub>x</sub> and the suppression of strain relaxation in the barrier layer and concurrent 2DEG carrier density due to the *in-situ* passivation layer is studied.

### **3.2 Materials and Methods**

First, an AlGaN/GaN HEMT baseline heterostructure was grown by MOCVD at 1020 °C while keeping the chamber pressure between 30 Torr (for AlN growth) and 100 Torr (for the remaining III-Nitride structure). This unpassivated structure is referred to as the baseline reference sample (REFF). The details of the growth parameters and layers thickness with corresponding alloy compositions are described in Chapter 2. Experimental samples were produced by introducing various silane (SiH<sub>4</sub>)-ammonia (NH<sub>3</sub>) ratios to the chamber for 15 minutes, while maintaining the same temperature and chamber pressure of the HEMT structure.

Tapping mode atomic force microscopy (AFM) was used to ascertain surface morphology. Several X-ray diffraction (XRD) techniques were employed utilizing a Rigaku SmartLab 3 kW system. The thickness of the near-surface layers was measured by x-ray reflectometry (XRR). The measured XRR data were fitted using GlobalFit software. High resolution x-ray diffraction (HRXRD) with a Ge (220)×2 monochromator was used

to image the reciprocal space map (RSM) around the GaN asymmetric (10-14) reflections and symmetric axis coupled scan of the III-Nitride layers around the (0002) reflections. By combining the in-plane lattice constant,  $a$ , from (10-14) reflections and out of plane lattice constant,  $c$ , from symmetric (0002) reflections, the composition and in-plane strain of the barrier layer was determined using strain-corrected Vegard's law<sup>42,56</sup> discussed in Chapter 2. Furthermore, Al composition for the relaxed  $\text{Al}_x\text{Ga}_{1-x}\text{N}$  transition layers ( $x = 0.51 - 0.52$  for TL1, and  $x = 0.25 - 0.26$  for TL2) were determined using Vegard's law for the  $c$ -plane (out of plane) lattice constant from the symmetric GaN (0002) reflection data. Scanning transmission electron microscopy (STEM) was used to analyze the interface characteristics and layer thicknesses of the passivated and unpassivated samples. Cross-sectional samples were prepared using standard focused ion beam (FIB) techniques using a FEI Helios Nanolab 400 DualBeam system by first depositing a protective Pt layer and milling using a 30 kV accelerating voltage. A final polishing step was then done with an accelerating voltage of 2 kV to remove surface damage. Bright-field and high-angle annular dark-field (HAADF) images of the samples were collected using a JEOL ARM 200F operating at 200 kV. Hg-probe C-V measurements were performed to evaluate the effect of the passivation on AlGaIn/GaN HEMT using a Materials Development Corporation (MDC) system. Total carrier density induced at the AlGaIn/GaN interface was evaluated by strain relaxation-based calculations.<sup>57</sup>

### 3.3 Results

The first *in-situ* passivation experiment ascertained the effect of  $\text{SiH}_4$  concentration on  $\text{SiN}_x$  thickness and surface morphology. Samples A, B and C, detailed in **Table 3.1**, were grown with  $\text{SiH}_4$  flows ranging between 0.05 to 0.53  $\mu\text{mol/min}$  while keeping the

NH<sub>3</sub> flow constant, at 0.60 mol/min, and maintaining the chamber pressure at 100 torr and a growth temperature of 1020 °C. **Figure 3.1(b)** shows the specular XRR reflection spectrum from the SiN<sub>x</sub> + barrier layer structures. For samples B, C, and REFF, well defined periodic Kiessing fringes were observed.<sup>29</sup> Since periodicity of the fringes directly relates to the thickness of each constituent layer, a Fast Fourier Transform (FFT) of the spectrum resolves the individual contribution of each layer. Using Rigaku's GlobalFit software, which incorporates both optimization (Extended Fourier Transform) and refinement (least-square) of the layer parameters, thicknesses, interface roughness and material density of each layer is estimated.<sup>50</sup> The R factor (reliability of the fit, or a measure of agreement between the experimental and fitting parameter)<sup>58</sup> for the fitted curves ranges between 0.029 to 0.033. **Figure 3.1(a)** shows the growth rate of SiN<sub>x</sub> with respect to the SiH<sub>4</sub> flow, and associated barrier layer thicknesses. The dashed line in **Figure 3.1(a)** indicates the thickness of the baseline REFF sample. The growth rate of the *in-situ* SiN<sub>x</sub> is linearly dependent on the SiH<sub>4</sub> concentration. For sample A, with the lowest SiH<sub>4</sub> flow, 0.05 μmol/min, there is no apparent growth of SiN<sub>x</sub> as indicated by the absence of Kiessing fringes in **Figure 3.1(b)**. Furthermore, the III-N barrier layer has been etched, as confirmed by RSM with the absence of the barrier layer peak (**Figure 3.4**, discussed later).

The highest growth rate of 17.4 nm/hr is achieved for sample C with a SiH<sub>4</sub> flow rate of 0.53 μmol/min. For sample B, while the SiN<sub>x</sub> growth rate is 8.4 nm/hr, it is also observed that ~ 30 % of the barrier layer has been etched, compared to the REFF sample (20.1 nm barrier layer thickness as indicated by the dashed line in **Figure 3.1(a)**). The

effect of reduced thickness is evident in the XRR scan shown in **Figure 3.1(b)**, as fringes become wider spaced with the reduction of the overall stack (SiN<sub>x</sub> + AlGaN) thickness.

Table 3.1 Reactant gas flow conditions of the experimental samples with associated SiN<sub>x</sub> growth rate, AlGaN barrier layer thickness and AFM RMS roughness.

	SiH <sub>4</sub> ( $\mu\text{mol}/\text{min}$ )	SiH <sub>4</sub> /NH <sub>3</sub> ( $\times 1\text{E}-6$ )	AFM RMS Roughness s 1 $\mu\text{m}$ by 1 $\mu\text{m}$ (nm)	From XRR Data		
				Barrier (nm)	SiN <sub>x</sub> (nm)	Growth Rate (nm/hr)
A	0.05	0.09	0.68	0	0	0.0
B	0.27	0.44	0.49	13.6	2.1	8.4
C	0.53	0.89	0.51	18.6	4.3	17.4
D	0.53	1.85	0.82	20.0	2.9	11.6
E	0.53	24.0	0.64	14.2	1.9	7.3
REFE	N/A	N/A	0.15	20.1	N/A	N/A

Similar barrier layer etching while growing *in-situ* SiN<sub>x</sub> with low SiN<sub>x</sub> growth rate (< 10 nm/hr) has been reported by Lugani et al. for InGaN/GaN at 875 °C and by Ma *et al.* at (1080 °C to 1145 °C) for AlN/GaN HEMT structures.<sup>54,59</sup> Selective etching of GaN with SiH<sub>4</sub>, for either intentional reduction of threading dislocations in GaN heteroepitaxy<sup>60</sup>, or for decorating dislocations for better contrast<sup>61</sup> in the MOCVD environment, has been reported by others. Etch selectivity is due to a higher etch rate at screw and mixed dislocation cores, compared to edge dislocations. This has been attributed to the lack of atomic steps on the surface at edge threading dislocations, but are present around screw and mixed threading dislocations, and the associated favorable step-edge etching by SiH<sub>4</sub><sup>60</sup>. Therefore, the etching process is dominated by the SiH<sub>4</sub> induced etching rather than decomposition of GaN at elevated temperature (> 870 °C) in a nitrogen overpressure environment. In these samples, the selective etching of GaN with SiH<sub>4</sub> is an effect of two

different mechanisms. Initially, when the  $\text{SiH}_4$  is introduced to the chamber, it encounters the surface GaN cap layer and GaN etching begins around the screw and mixed dislocation cores. Simultaneously,  $\text{SiN}_x$  is deposited as a discontinuous porous film and this fractal like film acts as a mask for selective  $\text{SiH}_4$  etching of the Al(Ga)N, but over time these fractals coalesce<sup>54</sup>. If the growth rate of the  $\text{SiN}_x$  is not sufficiently high, the initial selective etching of Al(Ga)N will leave pitted features as seen in the 3D AFM images in **Figure 3.1(c)** (i.e., samples B and C).

As shown in **Figure 3.1**, the increased  $\text{SiH}_4$  flow and concomitant higher growth rate of  $\text{SiN}_x$  reduces the etching of the underlying AlGaN barrier layer. This is because the higher  $\text{SiH}_4$  flow readily incorporates more Si from  $\text{SiH}_4$ , which can dominate the competing  $\text{SiH}_4$  induced etching of Al(Ga)N thereby reducing etching. **Figure 3.1(c)** shows tapping mode  $1\mu\text{m} \times 1\mu\text{m}$  3D AFM images of the different sample surfaces with the line scan profiles given as insets to the images. The REFF sample AFM image indicates the representative surface comprising the GaN (cap) layer of the unpassivated HEMT. For sample A, the GaN buffer layer surface is imaged (due to complete etching of the entire AlGaN barrier layer). For sample B, the AFM image is of the  $\text{SiN}_x$  coated AlGaN barrier layer surface, while for sample C, the  $\text{SiN}_x$  coated GaN cap layer is imaged. The standard HEMT (REFF) wafer has a very smooth surface (RMS = 0.15 nm) with atomic steps present.

For sample A, the etched surface is substantially pitted, with RMS roughness of 0.68 nm, as the barrier layer has been completely etched. For sample B, the height of the pits is less than sample C (see inset images) indicating that surface damage is more prevalent with sample B compared to sample C. This is due to the  $\text{SiN}_x$  growth rate for

sample C being twice that of sample B, indicated in **Figure 3.1(a)**, which provides faster coalesce of the SiN<sub>x</sub> fractals thereby reducing surface damage.

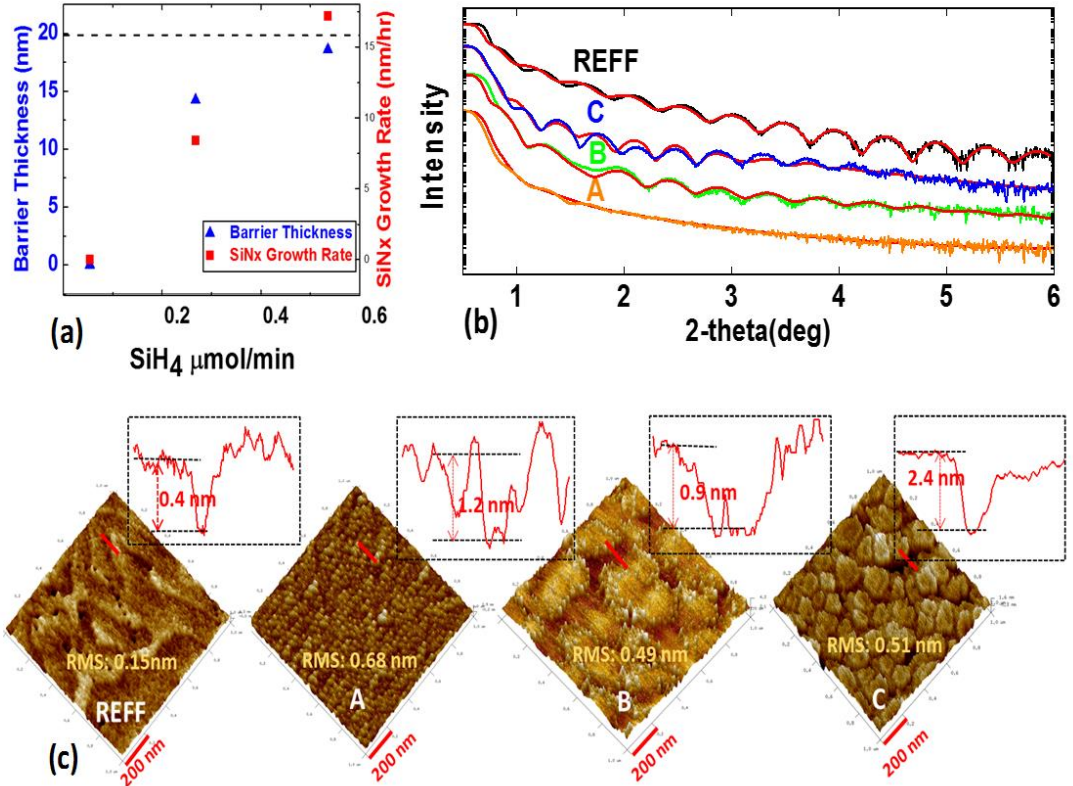


Figure 3.1 (a) Growth rate and barrier layer thickness variation with SiH<sub>4</sub> flow while keeping NH<sub>3</sub> and H<sub>2</sub> flows constant. The dashed line is the REFF sample barrier layer thickness, (b) XRR profile of SiN<sub>x</sub>/GaN/AlGaN/AlN/GaN HEMT heterostructure with fitted curves (RED), and (c) 1μm × 1μm 3D AFM images of the passivated *in-situ* SiN<sub>x</sub> surface. The inset is the line scan of the marked region (red line) on the AFM image.

From the results of the first experiment, it is ascertained that with increased SiH<sub>4</sub> flow and, thus, increased growth rate, better surface coverage is achieved, and III-Nitride etching is reduced or mitigated. The second experiment evaluated the effect of the NH<sub>3</sub> flow on the SiN<sub>x</sub> growth process. Samples D and E were grown with a constant (high) flow of 0.53 μmol/min SiH<sub>4</sub> (identical to sample C) while varying the NH<sub>3</sub> flow from 0.026 mol/min to 0.60 mol/min, as indicated in **Table 3.1**.

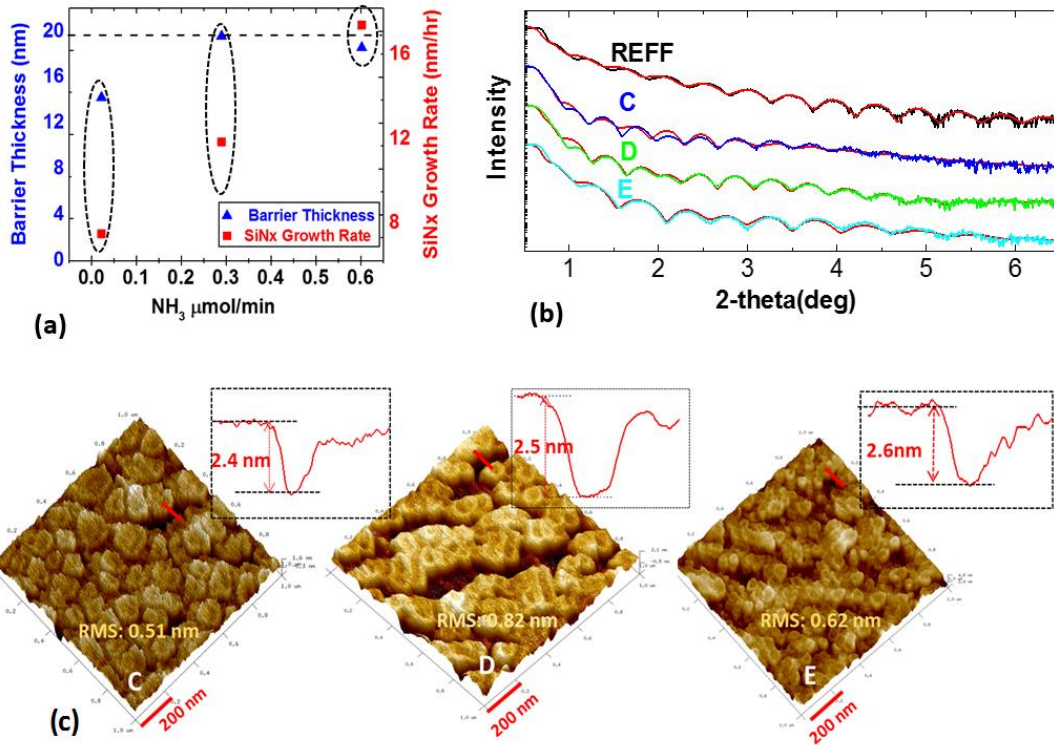


Figure 3.2 (a) Growth rate and barrier layer thickness variation with ammonia flow while keeping SiH<sub>4</sub> and H<sub>2</sub> flows constant. The dashed line is the REFF sample barrier layer thickness, (b) XRR profile of SiN<sub>x</sub>/GaN/AlGaIn/GaN HEMT heterostructure with fitted curves (RED), and (c) 1μm × 1μm 3D AFM images of the passivated *in-situ* SiN<sub>x</sub> surface. The inset is the line scan of the marked region (red line) on the AFM image.

**Figure 3.2** indicates the effect of NH<sub>3</sub> flow on the SiN<sub>x</sub> growth parameters. For sample E, with the lowest NH<sub>3</sub> flow (0.02 mol/min), the SiN<sub>x</sub> growth rate is 7.3 nm/hr, and the barrier layer (~ 14 nm) is partially etched (~ 20 % compared to the REFF sample). (The thinning of the barrier layer is also observed by RSM measurement, compared to the REFF sample, shown in **Figure 3.4**.) This is due to the low cracking coefficient of NH<sub>3</sub>, such that with lower NH<sub>3</sub> flow there are not enough N adatoms present at the surface to fulfill the necessary bonding for SiN<sub>x</sub> to achieve higher growth rate. Furthermore, insufficient N adatoms can lead to surface decomposition of the III-Nitride layers.<sup>24</sup> For samples C and D where the growth rate is 17.4 and 11.6 nm/hr, respectively, the III-Nitride barrier layer is substantially unchanged compared to the REFF sample. Furthermore, from the AFM

images (see **Figure 3.2(c)**) the density of the island (pit) like features is decreasing with increased  $\text{NH}_3$  flow which suggests that lateral growth of  $\text{SiN}_x$  has increased with increasing  $\text{NH}_3$  thereby reducing the underlying etching of the III-Nitride layers.

The AFM images in **Figure 3.2(c)** shows the  $\text{SiN}_x$  surface exhibits island-like features. To investigate in greater detail, high resolution TEM was performed to observe the  $\text{SiN}_x$ -Al(Ga)N interface. **Figure 3.3** shows TEM images of sample D. **Figure 3.3(a)** shows a HAADF image of a pit formed as a result of etching of the AlGaN barrier layer. The  $\text{SiN}_x$  is seen as the dark layer between AlGaN and Ti. **Figure 3.3(b)** shows a high resolution HAADF image at the edge of the pit shown in **Figure 3.3(a)**. The  $\text{SiN}_x$  conformally coats both the pitted and unetched AlGaN surface. **Figure 3.3(c)** is an atomic resolution bright-field image of the etched AlGaN barrier/ $\text{SiN}_x$  interface showing that the AlGaN maintains atomic abruptness after etching. In HAADF the observed intensity increases with the atomic number of the elements present. This allows distinguishing regions of differing chemical composition. In **Figure 3.3(a)** and **(b)**, the  $\text{SiN}_x$  appears as a dark region because it is on average composed of lighter elements than the AlGaN barrier layer and Ti protective layer. The images show a cross-section of the  $\text{SiN}_x$ -Al(Ga)N interface in the vicinity of an etched pit. The lateral dimension of the pit is  $\sim 71$  nm with a height of  $\sim 3$  nm. The higher magnified images (**Figure 3.3(b)** and **(c)**) indicate an abrupt interface between  $\text{SiN}_x$  and Al(Ga)N. The  $\text{SiN}_x$  is continuous and the AlGaN- $\text{SiN}_x$  interface is smooth.  $\text{SiN}_x$  has grown conformally on and around the pitted AlGaN features. These data are explained by, first, the  $\text{SiN}_x$  has fractal growth on the Al(Ga)N surface while, second, simultaneously selectively etching the exposed Al(Ga)N surface by  $\text{SiH}_4$ . Thus, the fractal distribution of  $\text{SiN}_x$  acts as a mask and facilitates selective etching of the

Al(Ga)N surface with SiH<sub>4</sub>. Finally, once the SiN<sub>x</sub> lateral growth coalescences, the Al(Ga)N layer is protected from the reactive SiH<sub>4</sub> environment and the etching ceases.

**Figure 3.4** shows HRXRD RSM of the REFF AlGa<sub>0.2</sub>N/GaN HEMT and samples A-E, around the asymmetric III-Nitride (10-14) reflections. The measurements were performed using grazing exit (GE) geometry to minimize instrument induced aberration. The data are shown in a contour representation of diffraction intensity in reciprocal space coordinates  $Q_{(hkl)z}$  and  $Q_{(hkl)x}$ .

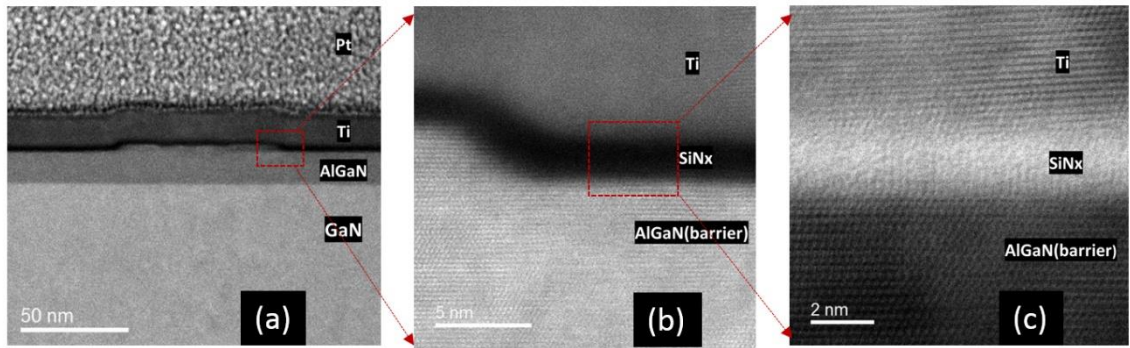


Figure 3.3 STEM cross-section images from sample D of the SiN<sub>x</sub>-Al(Ga)N interface in the vicinity of a pit. (a) HAADF image of pitting formed as a result of etching of the AlGa<sub>0.2</sub>N barrier layer. (The SiN<sub>x</sub> is the dark layer between the AlGa<sub>0.2</sub>N and Ti.) (b) High resolution HAADF image showing the edge of the pit in (a). The SiN<sub>x</sub> conformally coats the structure. (c) Atomic resolution bright-field image of the SiN<sub>x</sub> / AlGa<sub>0.2</sub>N barrier layer region.

The color scheme indicates variation in intensity of the diffracted beam with red representing the strongest intensity while blue represents the lowest. Thus, the peak positions in this coordinate system can be converted into interplanar spacing ( $d_z$ ,  $d_x$ ), and, hence, the crystal lattice constants ( $c$ ,  $a$ )<sup>29</sup>.

Strained lattice constants,  $a_{AlGa_0.2N,strained}$  and  $c_{AlGa_0.2N,strained}$ , of the AlGa<sub>0.2</sub>N barrier layer are determined from the RSM of the asymmetric GaN (10-14) plane. Strain

relaxation  $r(x)$ , which is a measure of the degree of relaxation, is determined from the in-plane lattice constant,  $a$ , according to,

$$r(x) = \frac{a_{AlGaN,strained} - a_{GaN}}{a_{AlGaN,relaxed} - a_{GaN}} \quad (3.1)$$

The vertical dashed lines on **Figure 3.4** represent the fully relaxed, or zero-relaxation, GaN  $a$ -axis. Because the AlGaN barrier layer is grown pseudomorphically on GaN, the lattice matched barrier layer peak (within the ellipses) lies on the GaN zero-relaxation line. As discussed previously, if the *in-situ* SiN<sub>x</sub> growth rate is less than 10 nm/hr, the barrier layer is etched as evident for sample A in **Figure 3.4** where there is no barrier layer peak within the ellipse, as well as for samples B and E, where the barrier layer peak intensity is reduced. The high SiN<sub>x</sub> growth rates for samples C and D allow for quick coalescent and minimal to no degradation of the AlGaN barrier layer as indicated by the nominally unchanged barrier layer peak intensities compared to the REFF sample.

Piezoelectric and spontaneous polarization have significant impacts on the AlGaN/GaN HEMT 2DEG properties. For all sample with *in-situ* SiN<sub>x</sub>, the degree of strain relaxation has decreased, as summarized in **Table 3.2**, which suggests that upon cooling, the SiN<sub>x</sub> has restricted relaxation of the barrier layer.<sup>62</sup>

For a given AlN mole fraction, considering the contribution of the strain relaxation, piezoelectric polarization of Al<sub>x</sub>Ga<sub>1-x</sub>N can be expressed as,<sup>57</sup>

$$P_{PE,AlGaN} = 2 \times [1 - r(x)] \times \frac{a_{GaN} - a_{AlGaN}}{a_{AlGaN}} \left( e_{31} - e_{33} \frac{C_{13}}{C_{33}} \right) \quad (3.2)$$

Elastic stiffness constants  $e_{31}$ ,  $e_{33}$ ,  $C_{33}$ , and  $C_{13}$  are estimated using linear approximation<sup>57</sup> for corresponding  $x$  values determined using strain corrected Vegard's law

as reported by Darakchieva et al. <sup>63</sup>. The relaxed lattice parameter and elastic constants used herein are taken from Gatabi et al. <sup>57</sup>

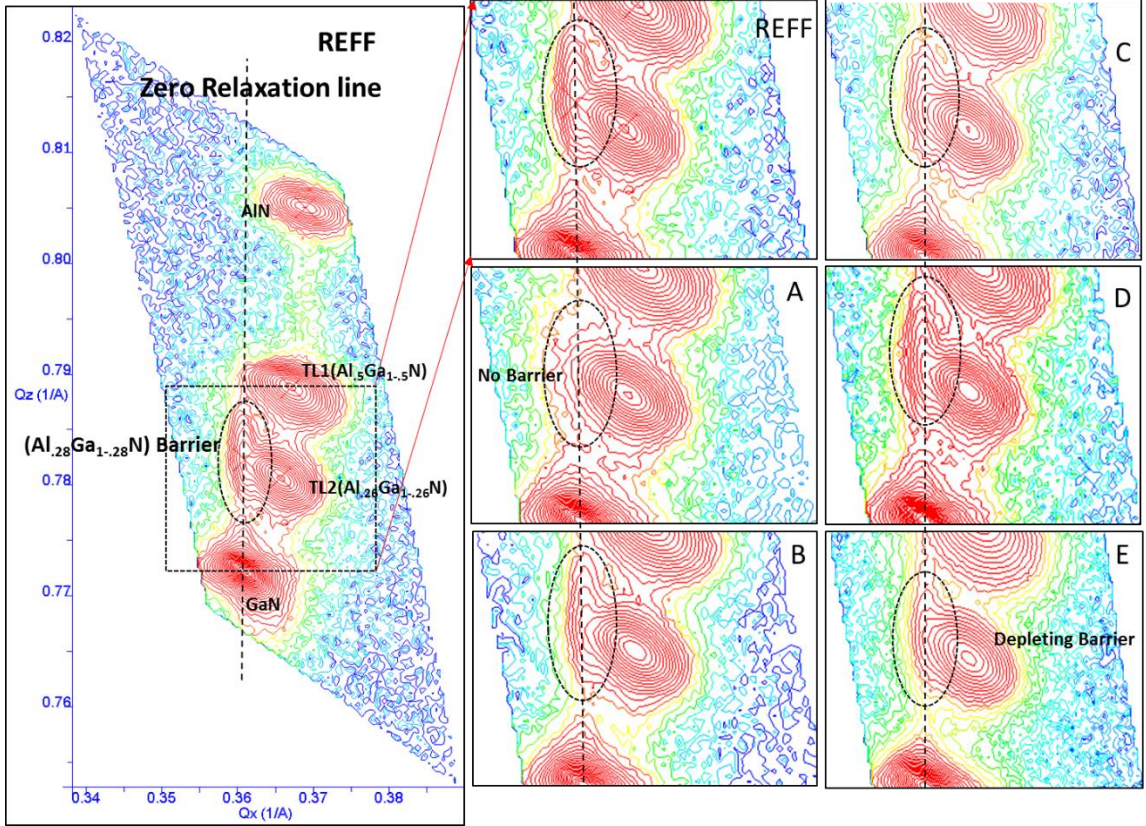


Figure 3.4 RSM of REFF AlGaN/GaN HEMT on Si with AlN nucleation layer (AlN) and two step-graded AlGaN transition layers (TL1 and TL2) along with samples A-E measured around the asymmetric (10-14) reflections. The vertical dashed lines show the zero-relaxation GaN  $a$ -axis and the ellipses indicate the AlGaN barrier layer peak position. Coordinate axes are given in  $Q_z$  and  $Q_x$  reciprocal coordinate ( $Q_z = 1/d_z$ ;  $Q_x = 1/d_x$ )

The AlGaN barrier layer spontaneous polarization is represented as,

$$P_{SP,AlGaN} = x \cdot P_{SP,AlN} + (1 - x) \cdot P_{SP,GaN} \quad (3.3)$$

Due to inherent spontaneous polarization effects in Al(Ga)N and strain induced piezoelectric effects in the AlGaN barrier, the 2DEG is formed at the AlGaN/GaN interface (without any intentional doping). Interface sheet charge density for an unpassivated

AlGa<sub>N</sub>/Ga<sub>N</sub> heterostructure, in terms of both piezoelectric and spontaneous polarization, can be written as,<sup>23,57</sup>

$$\sigma_s = \frac{P_{SP,AlGaN} + P_{PE,AlGaN} - P_{SP,GaN} - C_{AlGaN} \psi}{1 + C_{AlGaN} \frac{\pi \hbar^2}{q^2 m^*}} \quad (3.4)$$

Where  $q$  is the electron charge (1.6E-19 C),  $\hbar$  is reduced Planck's constant (6.62607E-34 m<sup>2</sup>KgS<sup>-1</sup>),  $m^* = 0.22 m_e$  ( $m_e$  is electron mass), and  $\psi = \phi_b - \Delta E_C$ . Here,  $\phi_b$  is the AlGa<sub>N</sub> surface potential,  $\Delta E_C$  is the conduction band offset at the AlGa<sub>N</sub>/Ga<sub>N</sub> interface, and  $C_{AlGaN}$  is the AlGa<sub>N</sub> capacitance per unit area.  $C_{AlGaN} = \frac{\epsilon_0 \epsilon_{AlGaN}}{t_{barrier}}$  has been determined using  $t_{barrier}$  values by XRR. For the unpassivated Al<sub>x</sub>Ga<sub>1-x</sub>N/Ga<sub>N</sub> REFF sample with  $t_{barrier} = 20$  nm,  $x = 0.28$  and with a strain relaxation of 6.9%, the approximated sheet charge density is determined to be  $9.5 \times 10^{12}$  cm<sup>-2</sup>.

The 2DEG density of the passivated SiN<sub>x</sub>/AlGa<sub>N</sub>/Ga<sub>N</sub> can be expressed as,

$$\sigma_{s,passivated} = \frac{P_{SP,AlGaN} + P_{PE,AlGaN} - P_{SP,GaN} - C_B \psi_P}{1 + C_B \frac{\pi \hbar^2}{q^2 m^*}} \quad (3.5)$$

Where,  $C_B$  is the series combination of the AlGa<sub>N</sub> and *in-situ* SiN<sub>x</sub> capacitances, and  $\psi_P = \phi_b - \Delta E_C - \Delta E_{C,inc}$ .  $\Delta E_{C,inc}$  is the conduction band offset from AlGa<sub>N</sub> to *in-situ* SiN<sub>x</sub>, and  $\phi_b$  is the *in-situ* SiN<sub>x</sub> surface potential  $C_B$  is given as,

$$\frac{1}{C_B} = \frac{1}{C_{AlGaN}} + \frac{1}{C_{SiNx}} = \frac{t_{barrier}}{\epsilon_0 \epsilon_{AlGaN}} + \frac{t_{SiNx}}{\epsilon_0 \epsilon_{SiNx}} \quad (3.6)$$

$C_B$  is calculated for  $t_{barrier}$  and  $t_{SiNx}$  thicknesses measured by XRR. **Table 3.2** gives the sheet charge densities evaluated using Equations 3.4 and 3.5 where a fixed dielectric constant of  $\epsilon_{SiNx} = 7.25$  is applied. Lattice parameters ( $a_{AlGaN}$ ,  $a_{GaN}$ ,  $a_{AlN}$ ) for

these calculations are taken from the measured values from RSM of the asymmetric GaN (10-14) reflections while ( $c_{AlGaN}, c_{GaN}, c_{AlN}$ ) are measured from symmetric GaN (0002) reflections. A sensitivity analysis was performed to ascertain the uncertainty regarding the (assumed fixed) dielectric constant of the different stoichiometric  $SiN_x$ , using reported values of  $\epsilon_{SiN_x}$  ranging from 5.8 to 8.2 by J. Ma et al.<sup>54</sup> The calculated variation in total sheet charge density across this range of values is less than 1% of the polarization induced charge shown in **Table 3.2**. Therefore, the values in **Table 3.2** accurately represent experimental variation in the samples.

For all *in-situ*  $SiN_x$  passivated samples, the sheet charge density is increased compared to the unpassivated REFF sample; **Table 3.2**, last column. (Except for sample A, in which the AlGaN barrier layer has been completely etched.) This increase in charge density can be attributed to two factors. First, the reduction in strain relaxation, from 6.9 % (REFF) to between 1.5 and 2.6 % (B-E), increases the piezoelectric polarization, because the direction of the tensile strain induced piezoelectric polarization in the AlGaN barrier layer is in the same crystallographic direction as the spontaneous polarization.<sup>62</sup> Second, mitigation of the AlGaN/GaN surface dangling bonds by donor like atoms provides a positive interface charge at the  $SiN_x$ -AlGaN interface. In order to separate these factors, the contribution of the induced sheet charge density due to strain relaxation only has been calculated and is shown in **Table 3.2**. Thus, the contribution from mitigation of interface states is 8.4 – 12 % of the total charge density. This range may be due to the varied constituent gas ratios ( $SiH_4/NH_3$ ) between samples B to E which may produce different stoichiometric ([Si]/[N]) ratios within the  $SiN_x$  passivation layers typical of this type of high temperature MOCVD grown  $SiN_x$  reported earlier by J. Ma et al.<sup>54</sup> Surface states

filling with different stoichiometric  $\text{SiN}_x$  and the impact on 2DEG charge density has been previously reported.<sup>64</sup>

An assessment of the effect of *in-situ*  $\text{SiN}_x$  passivation on the electrical properties of the AlGaIn/GaN HEMT has been conducted via Hg-probe C-V. **Figure 3.5** shows C-V results of the passivated (A-E) and unpassivated (REFF) samples. The voltage is varied from positive to negative using a 50 mV/s step at 100 kHz. Low residual capacitance  $C_{\text{min}}$  with a sharp transition from 2DEG accumulation to depletion, and a flat plateau ( $C_0$ ), corresponds to a typical AlGaIn/GaN HEMT C-V profile.<sup>15,55</sup> **Figure 3.5(a)** compares samples A, B, and C with varying  $\text{SiH}_4$  flow with the REFF sample. For sample C, the threshold voltage ( $|V_T|$ ) is increased compared to REFF because the  $\text{SiN}_x$  dielectric thickness contributes to the depth of the 2DEG below the sample surface, consistent with published results.<sup>65</sup> Correspondingly, the reduced thickness of the AlGaIn barrier layer for sample B justifies the lower  $|V_T|$  compare to REFF. For sample A, the C-V profile deviates from the typical HEMT due to the completely etched barrier layer, confirmed by XRR (**Figure 3.1(a)**) and RSM (**Figure 3.3**), discussed previously. Because the barrier layer is not present in sample A, the C-V profile could be due to diffusion of Si into the GaN acting as an n-type dopant and producing a near-surface n-GaN region<sup>66</sup>

**Figure 3.5(b)** compares the C-V profiles of samples C, D, and E with varying  $\text{NH}_3$  flows to the REFF sample. For samples C and D, the barrier layer thickness is substantially identical to the REFF sample, but with an additional 4.34 nm  $\text{SiN}_x$  for C and 2.90 nm  $\text{SiN}_x$  for D (**Table 3.1**). The correspondingly larger  $|V_T|$  values are, therefore, justified as the depth of the 2DEG from the surface has increased. For sample E, the total stack ( $\text{SiN}_x$  +

Barrier) thickness (~16 nm) is less than the REFF sample (~20 nm), and therefore, the positive shift in  $|V_T|$  is due to additional charge carriers provided to the channel.

Table 3.2 Al mole fraction, strain relaxation and polarization induced charge density calculated from XRD parameters.

	AlN% in AlGaN Barrier Layer	Barrier Layer Strain Relaxation (%)	Calculated Sheet Charge Density ( $\text{cm}^{-2}$ )	
			Induced, due to strain relaxation	Including $\text{SiN}_x$
A	N/A	N/A		N/A
B	29.2	2.6	0.96E+13	1.09E+13
C	27.2	1.5	0.98E+13	1.06E+13
D	28.1	1.6	0.99E+13	1.09E+13
E	27.0	1.6	0.93E+13	1.03E+13
REFF	27.8	6.9	0.95E+13	

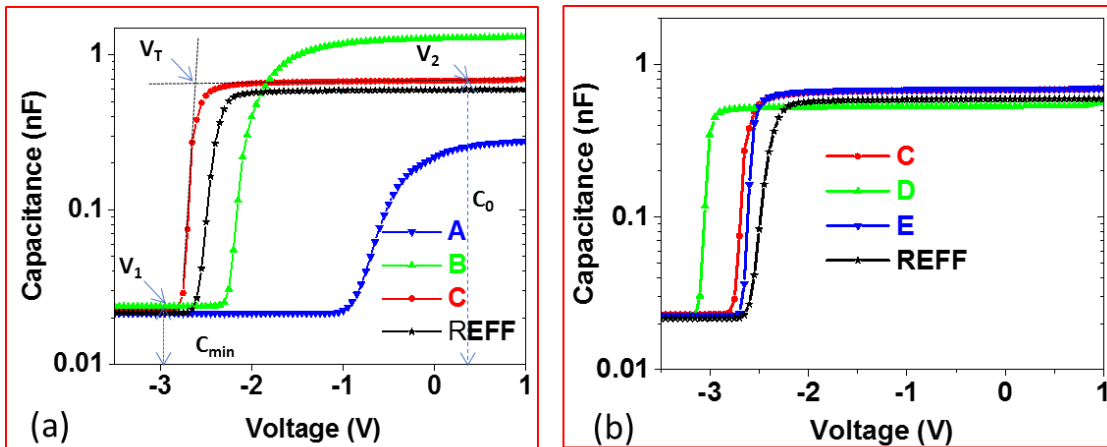


Figure 3.5 Hg-probe C-V of the *in-situ*  $\text{SiN}_x$  passivated HEMT samples compared with the unpassivated REFF sample. (a) C-V profile of the HEMT structures produced with varying  $\text{SiH}_4$  flow during  $\text{SiN}_x$  growth, and (b) with varying  $\text{NH}_3$  flow.

### 3.4 Conclusions

In conclusion, effects of varied  $\text{SiH}_4$  and  $\text{NH}_3$  gas flow ratios for growing *in-situ* MOCVD  $\text{SiN}_x$  passivation of AlGaIn/GaN HEMTs is studied. The growth rate and morphology of the *in-situ*  $\text{SiN}_x$  strongly depends on the constituent gas ratios.  $\text{SiH}_4$  induced selective etching of the underlying III-Nitride layers is prevalent with lower  $\text{SiH}_4$  and with lower  $\text{NH}_3$  gas ratios. This selective etching of III-Nitride material with  $\text{SiH}_4$  is due to two mechanisms:  $\text{SiH}_4$  induced etching of the Al(Ga)N around screw and mixed dislocation cores, and simultaneous selective  $\text{SiH}_4$  etching of the Al(Ga)N around fractal like  $\text{SiN}_x$  masking during the initial stages of growth before  $\text{SiN}_x$  coalescence. It is observed that with increased  $\text{SiH}_4$  flow and, thus, increased  $\text{SiN}_x$  growth rate, faster surface coverage is achieved, and III-Nitride etching is reduced or mitigated. It is also observed that  $\text{SiN}_x$  lateral growth increases with increasing  $\text{NH}_3$  flow while reducing the RMS surface roughness. Suppression of stress relaxation in the barrier layer has been observed for passivated samples, which provides increased piezoelectric polarization in the barrier layer. Both the suppression of the strain relaxation and surface state filling provides an increased 2DEG sheet charge density at the AlGaIn/GaN interface.

## 4 CO-RELATION OF CONSTITUENT GAS CHEMISTRY AND STOICHIOMETRY OF *IN-SITU* SiN<sub>x</sub> TO THE STRUCTURAL AND ELECTRICAL PROPERTIES OF AlGa<sub>N</sub>/Ga<sub>N</sub> HEMT

### 4.1 Introductions

*In-situ* SiN<sub>x</sub> suppresses strain-relaxation in the barrier layer, thereby helping prevent relaxation in the pseudomorphically grown AlGa<sub>N</sub> (> 20 nm ) barrier layer<sup>13-15</sup>. The degree of suppression of strain-relaxation should depend on the stoichiometry and, hence, the mechanical properties of the *in-situ* SiN<sub>x</sub>. Although suppression of strain relaxation using *in-situ* SiN<sub>x</sub> has been previously reported, the effect of constituent gas chemistry (and stoichiometry) on the degree of strain-relaxation has not been adequately studied. To realize the full potential of *in-situ* SiN<sub>x</sub> passivation, and thereby design an improved AlGa<sub>N</sub>/Ga<sub>N</sub> HEMT passivating layer, the co-relation between the SiN<sub>x</sub> stichometry and the suppression of strain-relaxation and surface state filling must be understood.

In this chapter, *in-situ* SiN<sub>x</sub> grown by MOCVD at typical AlGa<sub>N</sub>/Ga<sub>N</sub> growth temperature (1020 °C) and pressure (100 Torr) as a passivation layer for AlGa<sub>N</sub>/Ga<sub>N</sub> HEMTs is studied. The electrical properties (sheet resistance, electron mobility and sheet charge density) have been determined of the passivated AlGa<sub>N</sub>/Ga<sub>N</sub> heterostructures together with the degree of strain relaxation in the barrier layer and the stoichiometry ( $x = [N]/[Si]$ ) of the *in-situ* SiN<sub>x</sub> layer using x-ray photoelectron spectroscopy (XPS). Finally,

the relationship between  $\text{SiN}_x$  stoichiometry and electrical and mechanical properties of the AlGaIn/GaN HEMT is presented and explained.

## 4.2 Experimental Details

*In-situ*  $\text{SiN}_x$  passivated AlGaIn/GaN HEMT structures were grown using the Texas State MOCVD system on low resistivity ( $40 \text{ } \Omega\text{-cm}$ ) on-axis Si (111) substrates. The details of the baseline unpassivated HEMT structure (REF) and the thicknesses of the corresponding layers are discussed in the previous chapter. Finally, 2%  $\text{SiH}_4$  in Hydrogen ( $\text{H}_2$ ) gas with Ammonia ( $\text{NH}_3$ ) was introduced to the chamber keeping the same temperature and pressure of the HEMT structure to minimize any process dependent degradation. Experimental *in-situ*  $\text{SiN}_x$  passivated samples (labeled A1, B1, C1, and D1) were produced by introducing various silane-ammonia ratios to the chamber.

Tapping mode AFM was used to ascertain surface morphology. The thickness of the near-surface layers was measured by x-ray reflectometry (XRR). In-plane lattice constant,  $a$ , was obtained from the GaN (10-14) reflections and the out of plane lattice constant,  $c$ , from the symmetric GaN (0002) reflections. The composition and in-plane strain of the barrier layer was determined using strain-corrected Vegard's law. Al composition for the relaxed  $\text{Al}_x\text{Ga}_{1-x}\text{N}$  transition layers ( $x = 0.51 - 0.52$  for TL1, and  $x = 0.25 - 0.26$  for TL2) were determined using Vegard's law for the  $c$  lattice constant from the symmetric GaN (0002) reflection data.

X-ray photoelectron spectroscopy (XPS) was performed to determine the stoichiometry ( $x = [\text{N}]/[\text{Si}]$ ) of the *in-situ*  $\text{SiN}_x$ . Cloverleaf Hall structures were fabricated to characterize the electrical properties of the *in-situ*  $\text{SiN}_x$  passivated AlGaIn/GaN HEMTs. First, clover-leaf Hall structures were mesa isolation using photolithography. The Oxford

100 Plasma Lab inductively coupled plasma (ICP)/ reactive ion etching (RIE) system was used for dry etching of the *in-situ* SiN<sub>x</sub>.

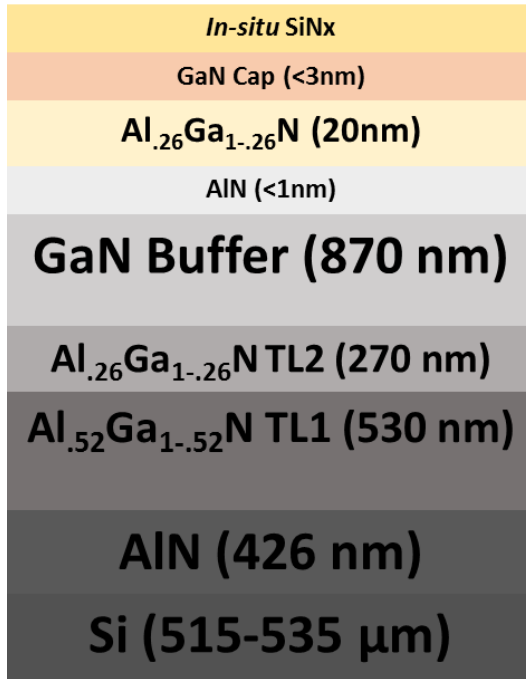


Figure 4.1 Schematic diagram of *in-situ* SiN<sub>x</sub> passivated HEMT.

To ensure a slow etch rate C<sub>3</sub>F<sub>8</sub> (20 sccm) + Ar (5 sccm) gas was flowed to the chamber while maintaining a pressure of 20 mTorr with an ICP/RIE power of 150W/15W at 60 °C, which results in a 15 nm/min etch rate. For III-Nitride dry etching, BCl<sub>3</sub> (25 sccm) + Cl<sub>2</sub> (10 sccm) gas was flowed to the chamber kept at 60 °C and 40 mTorr with a power of 750W/75W ICP/RIE, which produced a 120 nm/min etch rate. After defining the mesa isolation, Ohmic contact openings were made with a second photolithography mask followed by slow etching of the SiN<sub>x</sub> to avoid damage to the AlGa<sub>0.26</sub>N barrier layer surface. Ohmic contact metal pads are defined by Ti (20 nm)/ Al (150 nm)/ Ni (10 nm)/ Au (150 nm) metal deposition by e-beam evaporator followed by metal lift-off. After metal liftoff,

a 30 sec 850°C rapid thermal annealing was performed. (Annealing conditions were investigated, optimized and calibrated (i.e., the minimum contact resistance,  $R_c$ , identified) by measuring  $R_c$  of circular TLM structures.) A 30 sec 850°C anneal in  $N_2$  environment yields an  $R_c$  of  $8.65E-8 \Omega\text{-cm}^2$ . To minimize process variation, the metal contacts for all samples were grown in a single run, and all wafers were loaded in one RTP annealing run. The Hall devices were characterized using the BioRad Hall system applying a 0.33 Tesla alternating magnetic field.

### 4.3 Results and discussion

From the previous experiment discussed in Chapter 3,  $SiH_4$  induced selective etching of the underlying III-Nitride layers is prevalent with lower  $SiH_4$  and with lower  $NH_3$  gas ratios. It was observed that with increased  $SiH_4$  flow and, thus, increased  $SiN_x$  growth rate, faster surface coverage was achieved, and III-Nitride etching was reduced or mitigated. However, the previous experiments were limited by the  $SiH_4$  cylinder concentration. Thus, in these experiments, a higher concentration  $SiH_4$  cylinder (2% in  $H_2$ ) was installed that provides constituent gas ratios ( $R = SiH_4/NH_3$ ) from 4.44 to 88.9 E-6. This ratio range was investigated in a 4-step increment; A1, B1, C1 and D1 which is up to 1000X greater  $SiH_4$  concentration compared to the previous experiment. **Table 4.1** gives the growth conditions for the four experimental wafers.

**Figure 4.2** gives  $1 \mu\text{m} \times 1 \mu\text{m}$  2D AFM images of the surface of the AlGaN/GaN HEMTs. **Figure 4.2(a)** is from the unpassivated baseline sample (REF), and **(b)-(e)** are the *in-situ*  $SiN_x$  passivated samples; A1, B1, C1, and D1, respectively. **Figure 4.3** shows corresponding  $5 \mu\text{m} \times 5 \mu\text{m}$  2D AFM images of the samples. Typical surface morphology for the REF AlGaN/GaN HEMT is confirmed as shown in **Figure 4.2(a)** and **3(a)**. For the

sample with the lowest R values ( $R = 4.44 \text{ E-}6$  for A1, shown in **Figure 4.2(b)** and **3(b)**), some surface degradation is evident due to  $\text{SiH}_4$  induced selective etching. However, with increasing R (higher  $\text{SiH}_4$  content) the surface damage is reduced for sample B1 (**Figure 4.2(c)** and **4.3(c)**) and fully mitigated for samples C1 and D1 (**Figure 4.2(d)** and (e) and **Figure 4.3(d)** and (e), respectively). For C1 and D1, the  $\text{SiN}_x$  mimics the HEMT surface features and there is no surface damage. The AFM surface roughness is minimized (0.13 nm for  $1\mu\text{m} \times 1\mu\text{m}$ ) and is lower than the baseline REF (0.26 nm) which confirms that higher  $\text{SiH}_4$  content not only eliminates surface damage but also by reconstructing the surface it is reducing the surface roughness.

To measure the thickness of the near-surface layers, x-ray reflectometry (XRR) was performed. **Figure 4.4** shows the specular XRR reflection spectra taken from the  $\text{SiN}_x$  + barrier layer structures. GlobalFit software is used to simulate the XRR data using the referenced material's density (GaN, AlN, and AlGaN) to fit for barrier layer thickness,  $\text{SiN}_x$  thickness, and densities. The dotted lines represented the simulated data. A reasonable agreement is obtained between the measured data and simulated data, as indicated in **Figure 4.4**. The calculated thickness of the *in-situ*  $\text{SiN}_x$  is tabulated in **Table 4.1**. The corresponding growth rates have been calculated and compared with the AFM roughness and constituent gas flows and given in **Figure 4.5**. The  $\text{SiN}_x$  growth rate, determined by XRR, is approximately linearly dependent on R (note the discontinuity in the abscissa of **Figure 4.5**). The AFM roughness is reducing with increasing R values and plateauing at a minimum for the two highest gas flow ratio conditions (C1 and D1). The highest growth rate achieved is for sample D1 at 5.5 nm/min, which is a 30X over the growth rate measured in the previous experiment with 200 ppm  $\text{SiH}_4$  (see Chapter 2). With

increasing growth rate, lateral coverage is increased, thereby explaining the elimination of surface damage while reducing the overall roughness of the surface via reconstruction.

Table 4.1 Growth conditions and measured structural properties for the experimental wafers.

	SiH <sub>4</sub> / NH <sub>3</sub> (1E-6)	XRR SiN <sub>x</sub> thickness (nm)	AFM RMS roughness (nm)	FWHM (arcsec) GaN (0002)	Al composition (%)		
					TL2	TL1	Barrier
<b>A1</b>	4.44	6.4	0.40	572	26.4	52.4	28.1
<b>B1</b>	8.89	9.1	0.38	572	26.1	52.1	27.7
<b>C1</b>	22.22	7.4	0.17	590	26.2	51.8	27.0
<b>D1</b>	88.93	10.7	0.13	594	26.1	52.2	28.8
<b>REF</b>		(AlGaN 17.9)	0.26	587	26.0	51.8	26.5

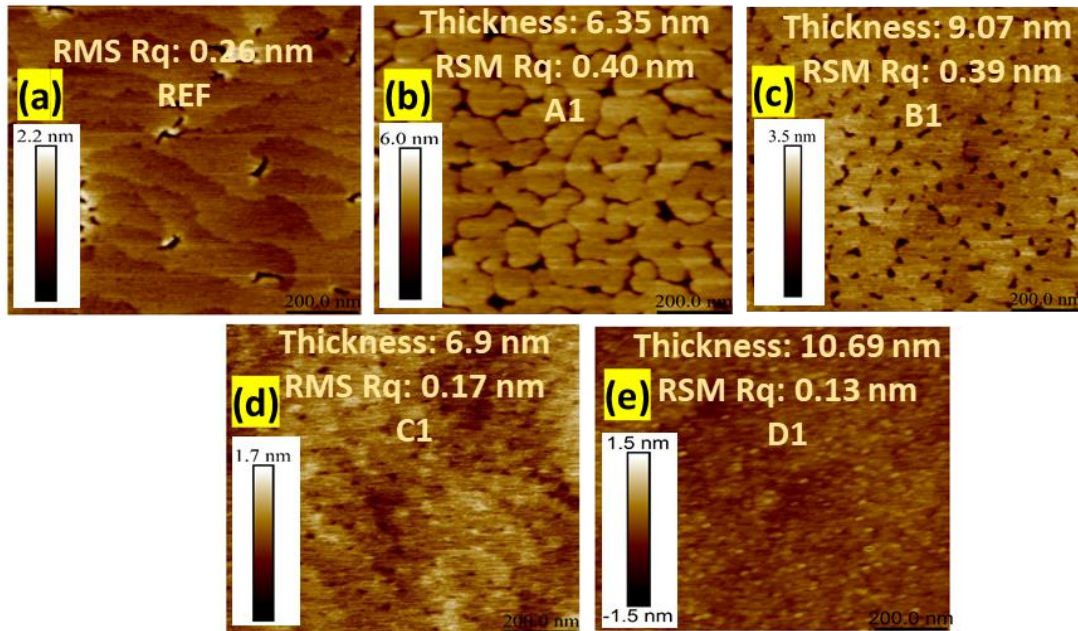


Figure 4.2 1 μm x 1 μm 2D AFM images of the AlGaN/GaN HEMTs, (a) unpassivated baseline sample (REF) (b)-(e) *in-situ* SiN<sub>x</sub> passivated samples A1, B1, C1, and D1, respectively.

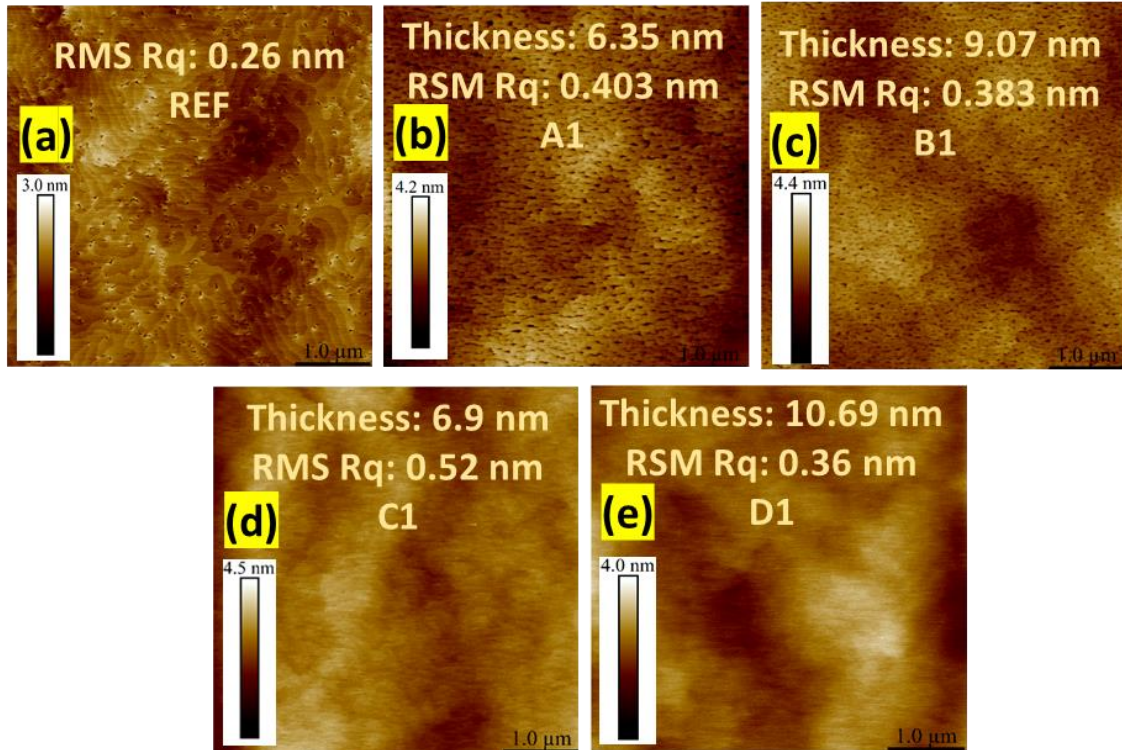


Figure 4.3  $5\mu\text{m} \times 5\mu\text{m}$  2D AFM images of the AlGaN/GaN HEMTs, (a) unpassivated baseline sample (REF) (b)-(e) *in-situ* SiN<sub>x</sub> passivated samples A1, B1, C1, and D1, respectively.

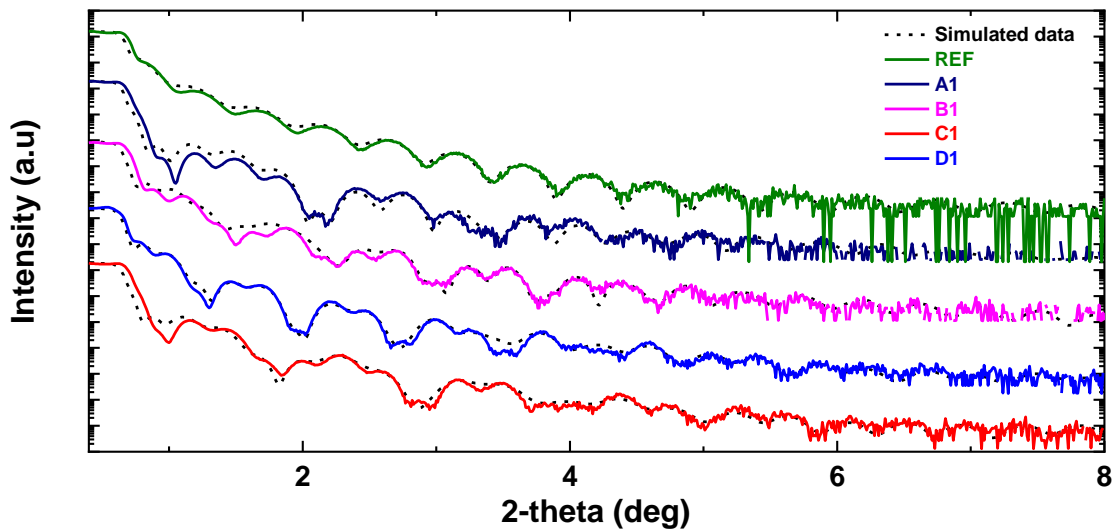


Figure 4.4 Measured and simulated grazing incidence XRR spectra of the *in-situ* SiN<sub>x</sub> passivated AlGaN/GaN HEMT heterostructures. The dotted lines show the simulated data.

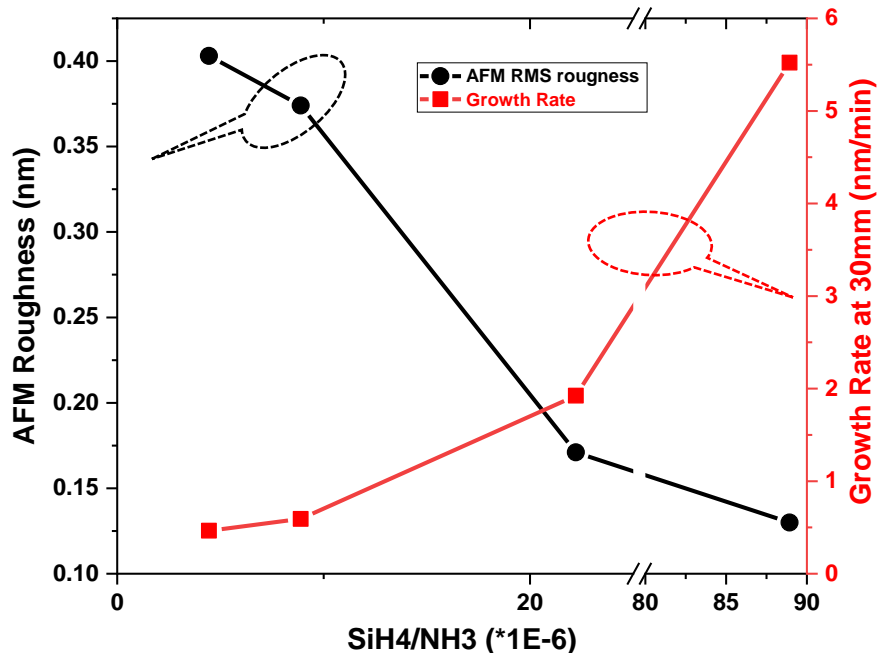


Figure 4.5 Relationship between constituent gas flow ratio ( $\text{SiH}_4/\text{NH}_3$ ) to the surface roughness and  $\text{SiN}_x$  growth rate.

HRXRD RSM around the GaN asymmetric (10-14) and symmetric (0002) reflections were performed to determine the stress-strain state in the barrier layer, as well as to characterize the other III-Nitride layers. The full-width half-maximum (FWHM) of the GaN (0002) rocking curve ( $\square\square$ scan), given in **Table 4.1**, ranges between 572 arcsec and 594 arcsec for all samples, which confirms the consistency of the growth process and high quality of the baseline heterostructure. Using Vegard's law the AlN composition of the transition layers (TL1 and TL2) was determined from the RSM around the (Al)GaN (0002) reflections as presented in **Table 4.1**. The AlN compositions are very consistent, within 1% variation, which again confirms the consistency of the baseline growth process.

A symmetric scan around GaN (0002) reflection cannot resolve the barrier peak as TL2 has nearly the same AlN composition as the barrier layer. However, the strain

sensitive GaN (10-14) asymmetric scan can fully resolve the barrier layer peaks as discussed in Chapters 2 and 3. **Figure 4.6** shows RSMs of the REF AlGa<sub>N</sub>/Ga<sub>N</sub> HEMT around the asymmetric (10-14) reflections. The vertical dashed line indicates the zero-relaxation Ga<sub>N</sub> *a*-axis, and the ellipses indicate the AlGa<sub>N</sub> barrier layer peaks for the different samples. A fully strained AlGa<sub>N</sub> barrier layer will lie on the zero-relaxation line. The figure shows the contour maps in reciprocal coordinates  $Q_z$  and  $Q_x$  ( $Q_z = 1/d_z$ ;  $Q_x = 1/d_x$ ). The right-side scans show the barrier peaks of the passivated samples A1, B1, C1, and D1. For all samples, a distinct barrier layer peak is observed. The consistent barrier layer peaks in the passivated samples with comparable size and shape to the REF (baseline) sample ensures that there has not been damage to the structural quality of the barrier layer.

Due to the very high TEC of amorphous SiN<sub>x</sub> compared to the III-Nitride layers and its atomic level adhesion with the underlying layers, *in-situ* SiN<sub>x</sub> suppresses strain relaxation in the fully strained barrier layers. Following the approach discussed in Chapters 3 and 4, the fully strained barrier layer's compositions (*x*) is calculated from the lattice parameters *a* and *c* determined from the Ga<sub>N</sub> asymmetric (10-14) and Ga<sub>N</sub> symmetric (0002) reflections. Corresponding strains, strain relaxation and stress values are determined as presented in **Table 4.2**. All *in-situ* SiN<sub>x</sub> passivated wafers show a degree of suppression of strain relaxation in the pseudomorphically grown barrier layer. Detail of the equations and processes to determine strain, strain-relaxation and bi-axial stresses have been discussed in Chapter 2&3.

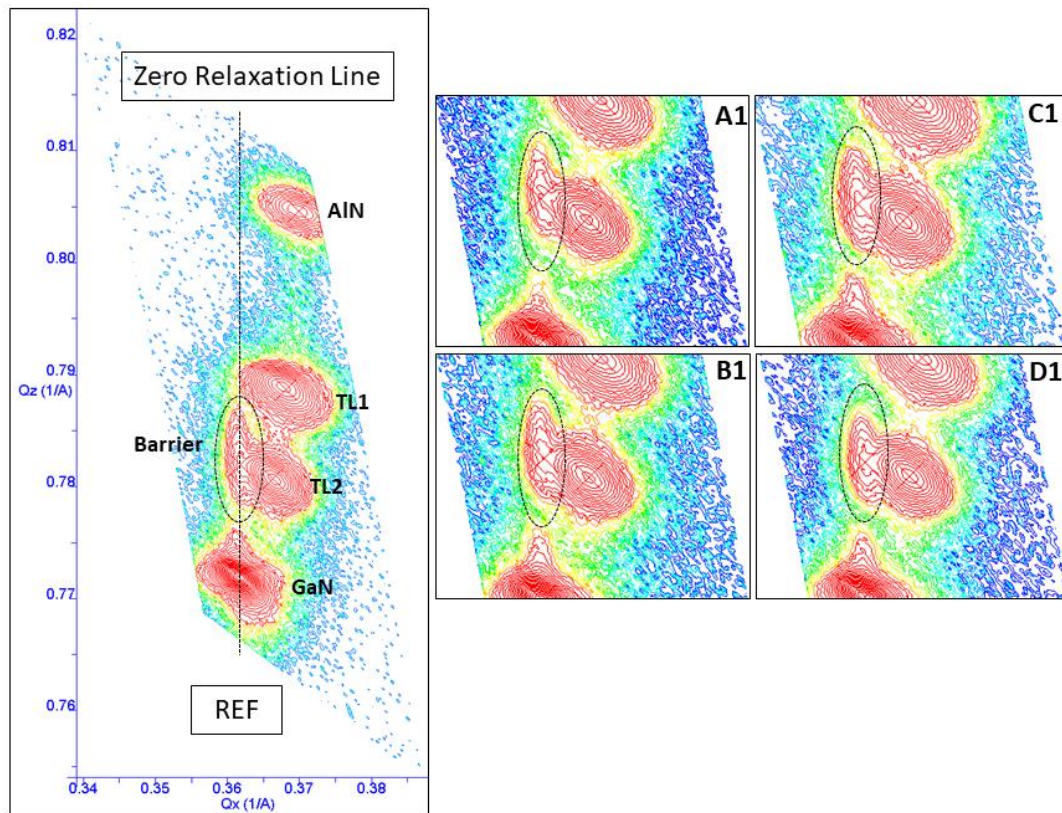


Figure 4.6 RSMs of REF AlGaIn/GaN HEMT on Si with AlN nucleation layer and two step graded AlGaIn transition layers (TL1 and TL2) around the GaN asymmetric (10-14) reflections. The vertical dashed lines show the zero-relaxation GaN  $a$ -axis, and the ellipses indicate the AlGaIn barrier layer peak position. The figure shows the contour map of the reciprocal space in reciprocal coordinates  $Q_z$  and  $Q_x$  ( $Q_z = 1/d_z$ ;  $Q_x = 1/d_x$ ). The right-side scans show the barrier peaks of passivated sample A1, B1, C1, and D1.

XPS based surface analysis is performed to estimate the stoichiometry of the MOCVD grown *in-situ* SiN<sub>x</sub>. Deconvolution and peak fittings were performed using Origin 2016 software. First, charge correction was performed to compensate for insulator charging using the 285 eV C1s peak as reference. The peaks were then fitted using a Gaussian function and Shirley background subtraction method. Deconvoluted peaks were fitted using bounds to limit, and accurately identify, different chemical bonding energy contributions; Si-Si, Si-N, and Si-O-N.

Table 4.2 The structural and electrical properties of in-situ SiN<sub>x</sub> passivated AlGaIn/GaN HEMT with SiN<sub>x</sub> stoichiometry

	SiH <sub>4</sub> /NH <sub>3</sub> (*1E-6)	XPS	Hall Data			XRD Data		
		x= [N]/[Si]	R <sub>s</sub> ohm/sq	cm <sup>2</sup> V <sup>-1</sup> S <sup>-1</sup> (1E3) μ	cm <sup>-2</sup> (1E13) N <sub>s</sub>	Strain Relaxation %	Stress (GPa)	
						Barrier	GaN	
<b>A1</b>	4.44	1.37	330	1800	1.04E+13	13.4	3.25	<b>0.79</b>
<b>B1</b>	8.89	1.31	320	1890	1.03E+13	9.6	2.76	<b>0.22</b>
<b>C1</b>	22.22	1.13	325	2140	8.97E+12	2	3.45	<b>0.92</b>
<b>D1</b>	88.93	1.11	275	2500	8.91E+12	2.1	4.08	<b>1.4</b>
<b>REF</b>			484	1650	7.81E+12	17.3	2.97	<b>0.77</b>

**Figure 4.7** shows the deconvoluted peaks of Si2p excitation. As evident from the figures, each of the samples has strong Si-N bond formation for both stoichiometric Si<sub>3</sub>N<sub>4</sub> and non-stoichiometric SiN<sub>x</sub>. With increasing SiH<sub>4</sub>/NH<sub>3</sub> ratio, the Si-Si bond contribution increases (dark blue curves) which suggests that with increasing SiH<sub>4</sub> content, there are additional Si atoms available for bonding that are not saturated by N atoms. **Figure 4.8** shows the N1s peak for the four passivated samples. For all samples, the peak lies between 396 and 397 eV, which is characteristic of Si<sub>3</sub>N<sub>4</sub> bonding<sup>67</sup>.

To analyze the SiN<sub>x</sub> stoichiometry (x = [N]/[Si]) the peak area sensitivity method is employed, which is more accurate than other methods such as intensity<sup>67</sup>. For a sample with a homogeneous analysis volume, the number of photoelectrons per second in a specific spectrum is given by<sup>67</sup>:

$$I = nf\sigma\theta y\lambda AT \quad (4.1)$$

Where n is the number of atoms of the element per cm<sup>3</sup> of the sample, f is the x-ray flux in photons/cm<sup>2</sup>-sec, σ is the photoelectric cross-section for the atomic orbital of the interest

in  $\text{cm}^2$ ,  $\theta$  is an angular efficiency factor for the instrumental arrangement based on the angle between the photon path and detected electron,  $y$  is the efficiency in the photoelectric process formation of photoelectrons in the sample,  $A$  is the area of the sample from which photoelectrons are detected, and  $T$  is the detection efficiency for electrons emitted from the sample. The above equation can be rewritten as follows:

$$n = I/f\sigma\theta y\lambda AT \quad (4.2)$$

For a specific XPS system, the denominator of Eq 4.2 can be defined as the atomic sensitivity factor (ASF),  $S$ . If a line from each of the two elements is strong, we can consider

$$\frac{n_1}{n_2} = \frac{I_1/S_1}{I_2/S_2} \quad (4.3)$$

The above expression may be used for all homogeneous samples if the ratio  $S_1/S_2$  is independent of the matrix materials. However, quantities such as  $\sigma$  and  $\lambda$  certainly varies from material to material although the ratios  $\sigma_1/\sigma_2$  and  $\lambda_1/\lambda_2$  remain constant. Thus, a set of values of  $S$  for all the elements can be developed. Considering the variation in the angular set-up, multiple sets of  $S$  values may be needed. So, a general expression for composition can be written following Eq 4.3 as follows,

$$C_x = \frac{n_x}{\sum n_i} = \frac{I_x/S_x}{\sum I_i/S_i} \quad (4.4)$$

Using the empirical values for ASF at  $54.7^\circ$  reported by Moulder *et al.*<sup>67</sup> the stoichiometry,  $x = [\text{N}]/[\text{Si}]$ , of  $\text{SiN}_x$  is determined as presented in **Table 4.2** and also correlated with the constituent gas chemistry as showed in **Figure 4.9(iii)**.

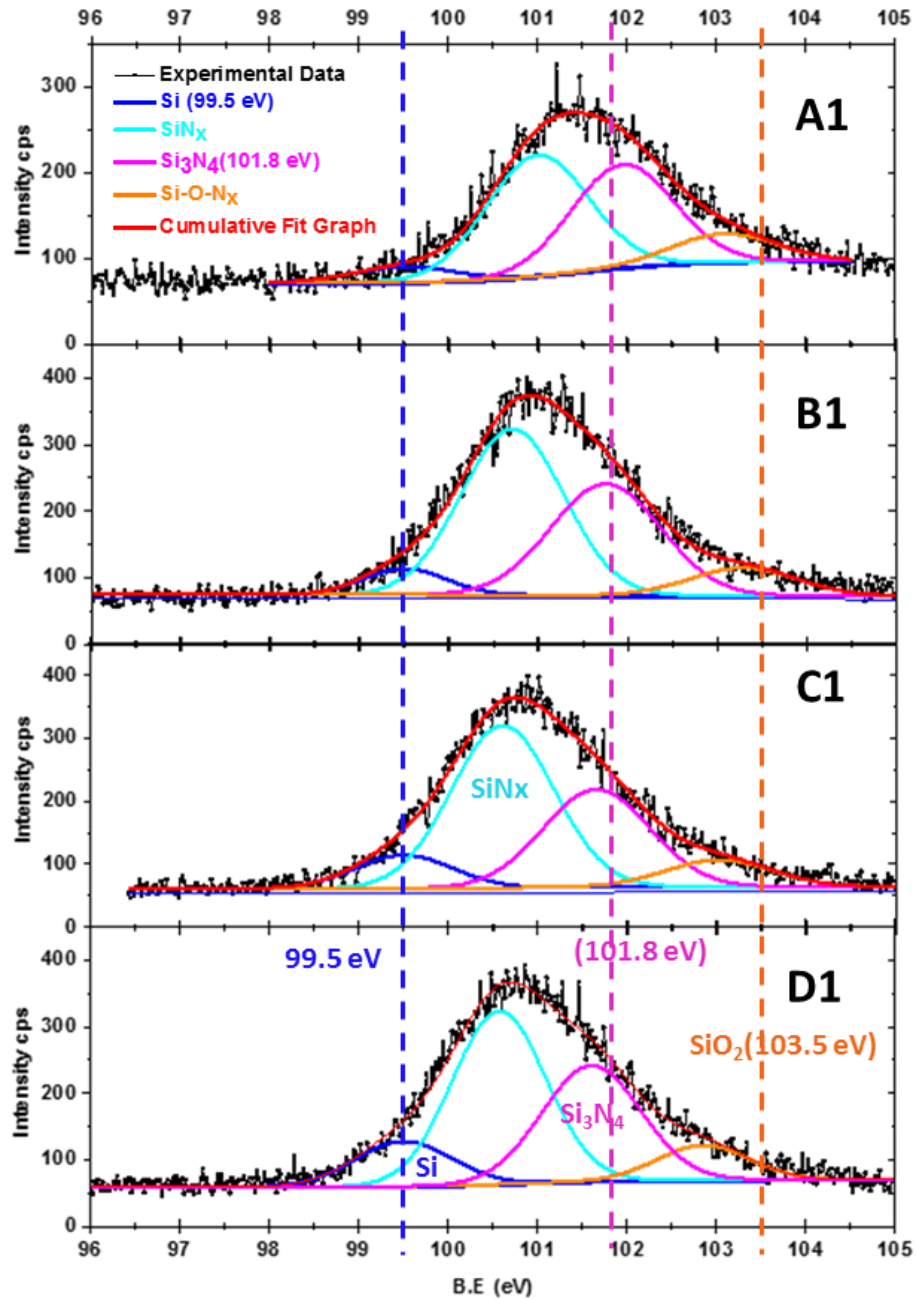


Figure 4.7 XPS analysis of *in-situ* SiN<sub>x</sub> comparing the Si2p spectra for SiN<sub>x</sub> grown on experimental wafers A1-D1. XPS data indicate peak shifts to binding energies at 99.5 eV (Si-Si), 101.8 eV (Si-N), and the formation of the Si-O-N bond.

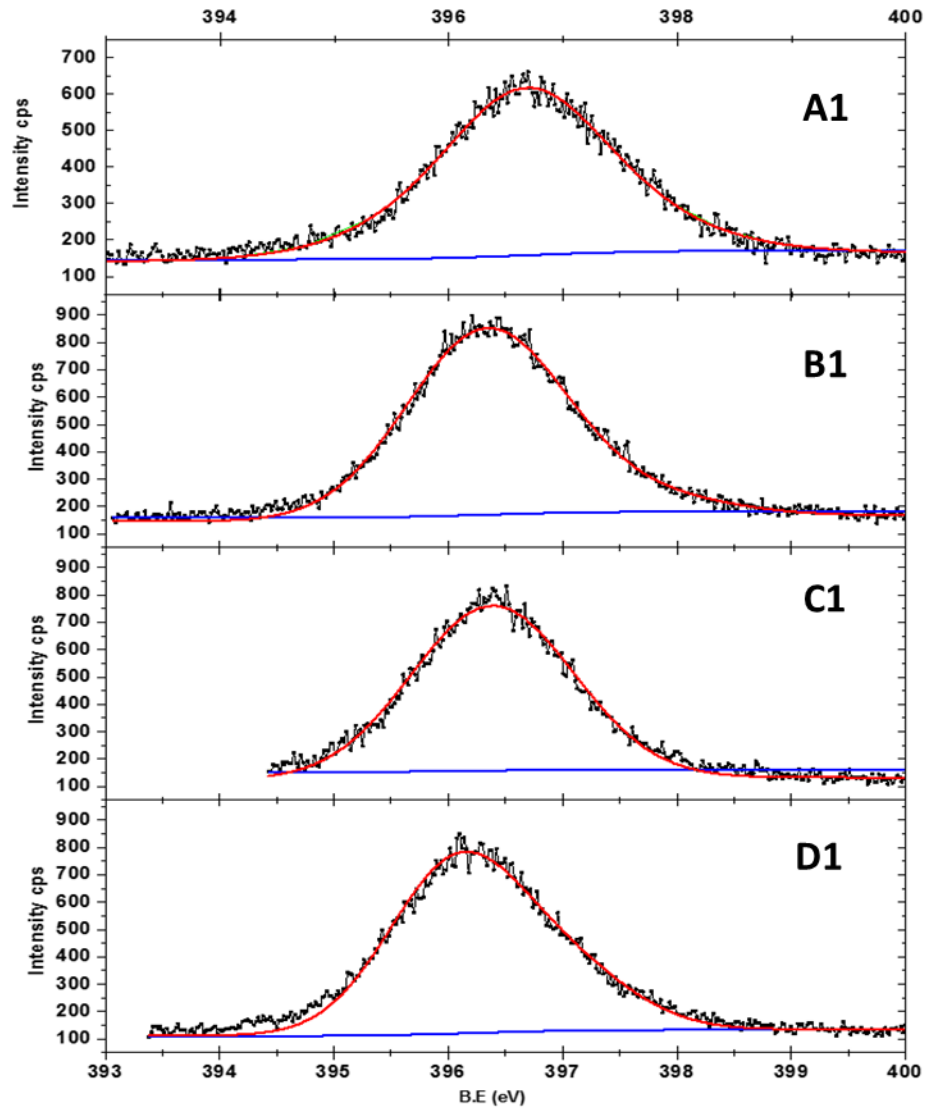


Figure 4.8 XPS analysis of *in-situ* SiN<sub>x</sub> comparing the N1s spectra for SiN<sub>x</sub> grown on experimental wafers A1-D1.

Electrical properties (sheet resistance, mobility & sheet charge density) were measured by the cloverleaf Hall structure fabricated by photolithography, metal liftoff and ICP/RIE based dry etch, using the Bio-Rad Hall measurement system at Texas State. **Figure 4.9** correlates the properties of the *in-situ* SiN<sub>x</sub> passivated AlGaIn/GaN experimental wafers. The properties being compared to the constituent SiH<sub>4</sub>-NH<sub>3</sub> gas flow ratio, R, includes, **(i)**

strain relaxation, **(ii)** biaxial stress, **(iii)** SiN<sub>x</sub> stoichiometry, **(iv)** 2DEG sheet charge density, **(v)** 2DEG Hall mobility, and **(vi)** 2DEG sheet charge density. The horizontal dashed lines on the graphs indicate the unpassivated REF baseline data.

All the passivated experimental samples show suppression of strain relaxation in the barrier layer, shown in **Figure 4.9(i)**, with a trend of reducing strain with increasing R, reaching a minimum (i.e., nearly fully strained AlGa<sub>N</sub> barrier) for samples C1 and D1. Suppression of strain relaxation follows the stoichiometry ( $x = [\text{N}]/[\text{Si}]$ ) of the *in-situ* SiN<sub>x</sub> as shown in **Figure 4.9(iii)**. With increasing Si content the SiN<sub>x</sub> density increases, which results in stiffer SiN<sub>x</sub>, and explains the increase in the suppression of strain relaxation<sup>68</sup>. With lower strain relaxation, the higher the AlGa<sub>N</sub> barrier layer strain, which produces higher biaxial stress as evidenced in the data in **Figure 4.9(ii)**. An increase in the biaxial tensile stress in the AlGa<sub>N</sub> barrier layer should increase the piezoelectric polarization electric field, which should improve the 2DEG sheet charge density<sup>7</sup>. In addition, wafers with higher R (SiH<sub>4</sub>/NH<sub>3</sub> ratio) and lower  $x = [\text{N}]/[\text{Si}]$  provide the maximum suppression of strain relaxation (2 %) which yields the largest biaxial tensile stress, 4.1 GPa for sample D1, in the barrier layer compared to 17.3 % for the reference wafer.

The 2DEG sheet charge density induced at the AlGa<sub>N</sub>/Ga<sub>N</sub> interface is an interplay between polarization induced sheet charge density and surface state filling with proper chemical surface bonding. All the *in-situ* passivated wafers have higher sheet charge density compared to the unpassivated REF wafer. The samples with highest x values (**Figure 4.9(iii)**); A1 with 1.37 and B1 with 1.31, have the highest sheet charge densities; 1.04E13 and 1.03E12 cm<sup>-2</sup>, respectively. While the barrier layer stress for samples C1 and D1 are highest; 3.5 GPa and 4.1 GPa, respectively, the reduction in the 2DEG sheet charge

density in these samples could be due to not only the surface state filling with lower N content but also from the higher biaxial tensile stress in the GaN buffer; 0.92 GPa for C1 and 1.39 GPa for D1, compared to the stress in A1; 0.76 GPa. Higher tensile stress in the GaN buffer would provide a piezoelectric field opposite to the barrier layer stress induced piezoelectric polarization. All *in-situ* SiN<sub>x</sub> passivated HEMT samples have higher mobility, as high as 2500 cm<sup>2</sup>/V·s for D1 and 2140 cm<sup>2</sup>/V·s for C1, compared to 1650 cm<sup>2</sup>/V·s for the unpassivated REF baseline.

The higher electron mobilities of for all the passivated samples could be due to the higher barrier layer strain relaxation suppression, which makes the interface between AlGa<sub>N</sub>/Ga<sub>N</sub> more abrupt compared to the unpassivated HEMT. A more abrupt heterostructure interface would reduce alloy scattering of the 2DEG at the AlGa<sub>N</sub>/Ga<sub>N</sub> heterointerface.

M. Azize et al. reported a 20% higher electron mobility under 0.16% biaxial strain,  $E_{xx}^b$ .<sup>69</sup> Kang et al. reported higher 2DEG conductivity for AlGa<sub>N</sub>/Ga<sub>N</sub> HEMTs under external stress<sup>70</sup>. A theoretical study by Dreyer et al. indicates a lower effective charge carrier mass under external stress<sup>71</sup>. Therefore, the outstanding charge mobility of sample D1 may be due to a combination of (a) the lowest x value (x = 1.13, Si rich SiN<sub>x</sub>) contributing to low interface alloy scattering due to the more abrupt heterointerface, (b) minimal barrier layer relaxation, and (c) lower effective mass of the carriers in the channel due to the higher strain in the Ga<sub>N</sub> material comprising the 2DEG channel. These three characteristic features of the optimized *in-situ* SiN<sub>x</sub> passivation process conspire to create the lowest sheet resistance of 276 Ω-sq for sample D1, which is a 43% reduction compared to the unpassivated REF sample's 484 Ω-sq sheet resistance. Furthermore, this sheet resistance

value represents a 27% reduction compared to the standard *ex-situ* PECVD SiN<sub>x</sub> passivated REF sample sheet resistance (380 Ω-sq).

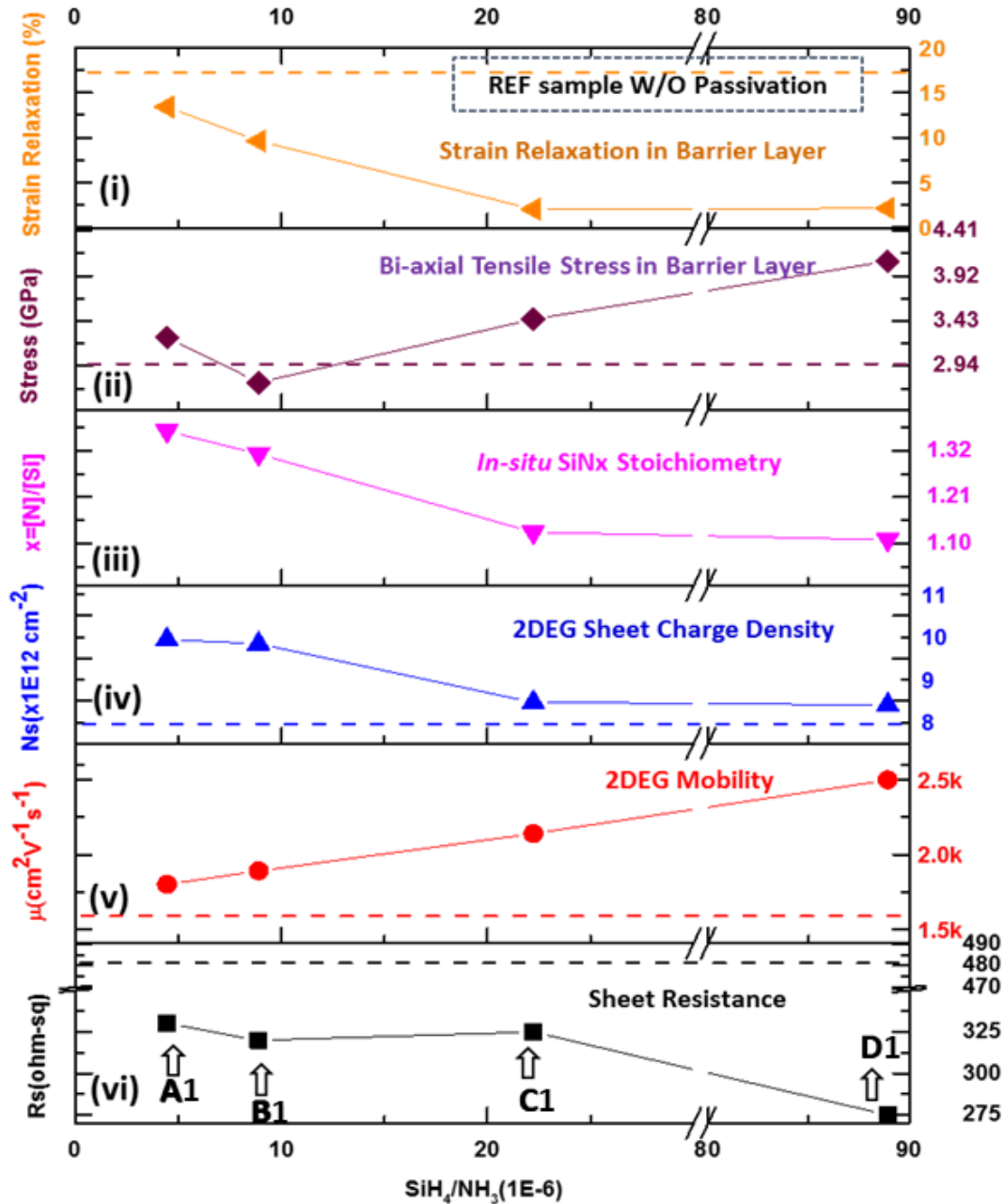


Figure 4.9 Effect of constituent gas flow ratio ( $R = \text{SiH}_4/\text{NH}_3$ ) on (i) barrier layer strain relaxation, (ii) barrier layer biaxial tensile stress, (iii) SiN<sub>x</sub> stoichiometry, (iv) 2DEG sheet charge density, (v) 2DEG mobility, and (vi) sheet resistance. The dashed lines represent measurements from the unpassivated AlGaIn/GaN HEMT (REF).

#### 4.4 Conclusions

Increasing the constituent gas ratio ( $R = \text{SiH}_4/\text{NH}_3$ ), thereby providing higher  $\text{SiH}_4$  content, increases the  $\text{SiN}_x$  growth rate, enabling quicker lateral coverage and eliminating surface damage.

The enhanced electrical properties are attributed to the simultaneous effects of  $\text{SiN}_x$  induced suppression of strain relaxation in the barrier layer, increased GaN buffer stress and surface state filling by optimizing the  $[\text{Si}]/[\text{N}]$  stoichiometry. The sample with high N content in the  $\text{SiN}_x$  exhibits high strain relaxation (13%), the largest sheet charge density  $1.04\text{E}13 \text{ cm}^{-2}$  and  $1800 \text{ cm}^{-2}\text{V}^{-1}\text{s}^{-1}$  mobility. These results are attributed to surface state filling with higher N content providing increased donor surface states to yield the high 2DEG. Finally, the combination of (a) low  $x$  (Si rich  $\text{SiN}_x$ ) contributing to low interface alloy scattering and a more abrupt heterointerface, (b) minimal barrier layer relaxation, and (c) lower effective mass of the carriers in the channel due to the higher strain in the GaN material results in an optimized *in-situ*  $\text{SiN}_x$  passivation process. The resulting 2DEG has the lowest sheet resistance ( $276 \Omega\text{-sq}$ ) representing a substantial reduction compared to the REF structure, whether unpassivated or PECVD  $\text{SiN}_x$  passivated.

## 5 OVERVIEW: SELF-HEATING IN AlGaN/GaN HEMTS, AND DIAMOND AS A HEAT SPREADER

### 5.1 Self-heating in AlGaN/GaN HEMT

Self-heating is one of the biggest challenges needing to be overcome to realize the full application potential of AlGaN/GaN HEMTs. Using ultra violet (UV) micro-Raman spectroscopy, Nazari et al. reported the temperature rise near the 2DEG channel is as high as 350 °C above ambient for an AlGaN/GaN based HEMT with an input power of 7.8 W/mm.<sup>16</sup> **Figure 5.1** indicates the depth dependent profile of temperature rise estimated by UV and visible micro-Raman spectroscopy at two different input powers ( $I_{DS}V_{DS}$ /channel length). The horizontal range for these data corresponds to the thickness averaged by each measurement, while the vertical range corresponds to error bars based on fitting the Raman data.<sup>16</sup> The comparison of self-heating induced temperature rise between different published results is difficult because each research group has different device designs. I.e., their devices have different substrate materials, barrier/buffer (AlGaN/GaN) layer thicknesses, gate layout, number of gate fingers, device density and heat sinking approaches. For a similar AlGaN/GaN transistor grown on silicon device, Beechem et al. reported a self-heating induced temperature rise of ~300 °C with an input power of ~2.8 W/mm based on visible micro-Raman measurements<sup>72</sup> while Sarua et al. reported a temperature rise of ~ 300 °C for an input power of 3.65 W/mm<sup>73</sup>. Due to this self-heating effect, the channel current ( $I_{DSS}$ ) drops significantly which significantly lowers the performance of such devices<sup>16,73–75</sup>.

**Figure 5.2** shows the side by side comparison of  $I_D$  vs.  $V_D$  for GaN-on-diamond and GaN-on-Si. Due to the self-heating effect  $I_D$  is more sensitive to the pulse length for GaN-on-Si HEMTs than GaN-on-diamond.<sup>76</sup> Power added efficiency,  $PAE \% = \frac{P_{out}}{P_{DC}} (1 - 1/G) \times 100 \%$ , is a key measure of a power amplifier, where  $P_{out}$  is output power and  $P_{DC}$  is the DC power drawn from the bias power supply.<sup>77</sup> Since,  $P_{out} \propto I_{DSS}$ ,  $I_{DSS}$  droop due to self-heating directly affects the efficiency of the devices.<sup>77</sup> Jessen et al. first demonstrated a working AlGaIn/GaN HEMT attached to a CVD diamond wafer manufactured by Group4 and Emcore.<sup>78</sup> This technological achievement proved the feasibility of using polycrystalline CVD diamond as a substrate material to maximize the heat extraction from high power HEMTs.

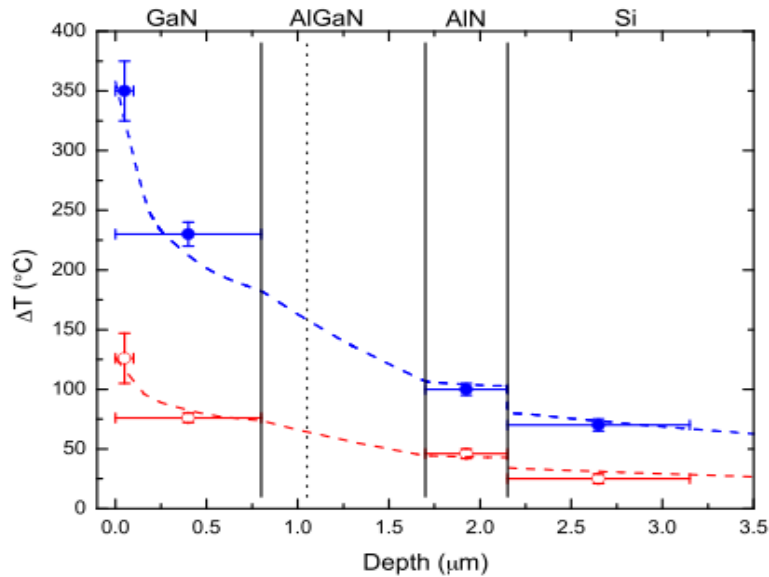


Figure 5.1 Temperature rise in different regions of an AlGaIn/GaN heterostructure at two different input powers obtained from Raman measurements along with thermal simulation results (dashed graphs) for input powers of 7.8 W/mm (filled squares) and 2.6 W/mm (empty squares). Vertical solid lines separate different layers in the device, and the vertical dashed line separates two AlGaIn TLs.<sup>16</sup>

Thermal conductivity of CVD grown diamond can be as high as  $2000 \text{ Wm}^{-1}\text{K}^{-1}$  for bulk material over  $500 \mu\text{m}$  thick <sup>17</sup>. Utilizing the advantage of the high thermal conductivity of CVD diamond and placing it proximate to the heat source (2DEG channel), Raytheon and TriQuint reported a reduced operating temperature of a GaN transistor on GaN/Diamond substrate by 40-45% compared to GaN-on-SiC. <sup>79,80</sup> While comparing with GaN-on-Si, Felix et al., reported the temperature reduction is  $\sim 85\%$  of its original temperature rise <sup>76</sup>. **Figure 5.3** shows a comparison between AlGaIn/GaN HEMTs on different substrates (solid rectangle) for GaN-on-Si, (open diamond) for GaN-on-SiC and (solid circle) for GaN-on-diamond. The temperature rise is maximum for GaN-on-Si and minimum for GaN-on-diamond while GaN-on-SiC falls in the middle. Different colors represent two different data sets for different samples. <sup>74</sup>

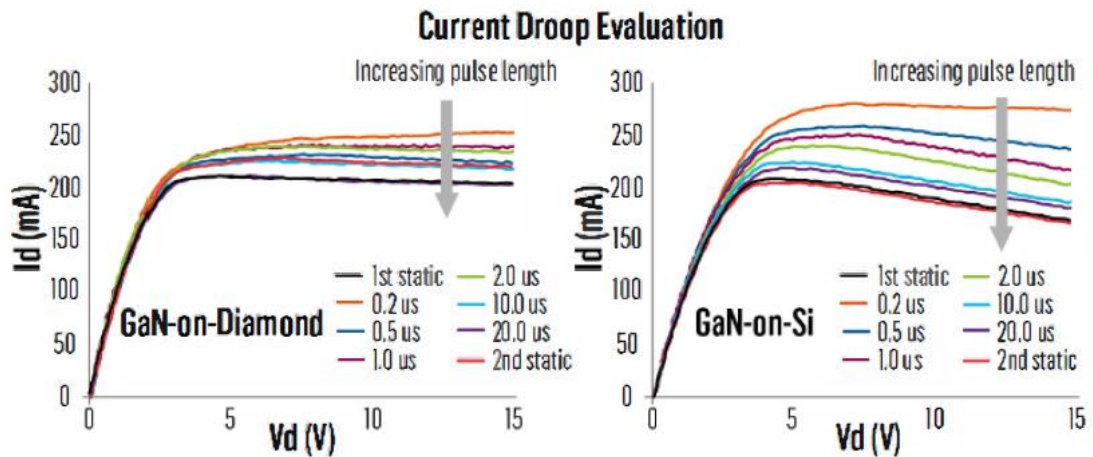


Figure 5.2 Current droop measured from GaN-on-diamond (left) and GaN-on-silicon (right) HEMTs with various pulsed dc duty-cycles.

## 5.2 Diamond as a Heat Spreader

Published literature suggests that there are three different approaches to incorporate diamond with GaN. The first approach, shown in **Figure 5.4(a)**, involves growth of

AlGaIn/GaN device layers on silicon (111) substrates by MOCVD. Then, using low temperature wafer bonding, a sacrificial silicon handle wafer is attached to the front-side of the GaN epi wafer to facilitate removal of the host silicon substrate. The host silicon substrate and epitaxial transition layers (TL) are removed. Next, a dielectric layer (typically  $\text{SiN}_x$ )<sup>73,76,81,82</sup> deposited onto the epi-inverted GaN buffer as an adhesion layer to facilitate seeding with nano-diamond. Approximately 100  $\mu\text{m}$  of polycrystalline diamond is grown on the  $\text{SiN}_x$ . Finally, the handle wafer is removed and the GaN/diamond wafer is ready for device processing.<sup>74,76</sup>

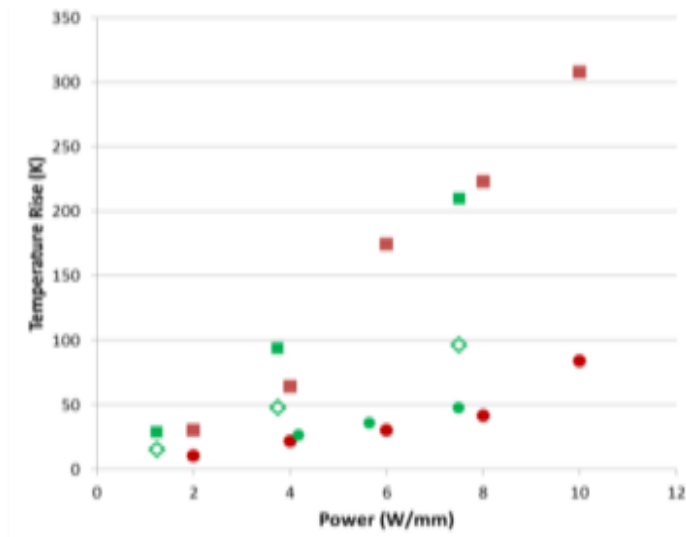


Figure 5.3 Temperature rise near the 2DEG channel measured by IR as a function of substrate material at various input powers. Solid rectangle for GaN-on-Si, open diamond for GaN-on- SiC and solid circle for GaN-on-diamond.

The second approach, shown in **Figure 5.4(b)**, involves growing AlGaIn/GaN device structures on SiC, Si or  $\text{Al}_2\text{O}_3$  substrates by MOCVD. The wafer undergoes front side processing first, followed by bonding a silicon carrier to facilitate substrate removal

<sup>83</sup>. The GaN and diamond surfaces are prepared for dielectric layer deposition and subsequent low temperature (>150 °C) bonding.

The third approach is more direct where no wafer bonding or handle wafer is required. In this approach, shown in **Figure 5.4(c)**, the AlGaN/GaN HEMT is grown on Si or SiC with a GaN cap on top, followed by subsequent deposition of a dielectric adhesion layer for seeding to facilitate the diamond growth on top. The substrate and the transition layers are removed to realize device processing on the N-face GaN buffer layer. <sup>76</sup>

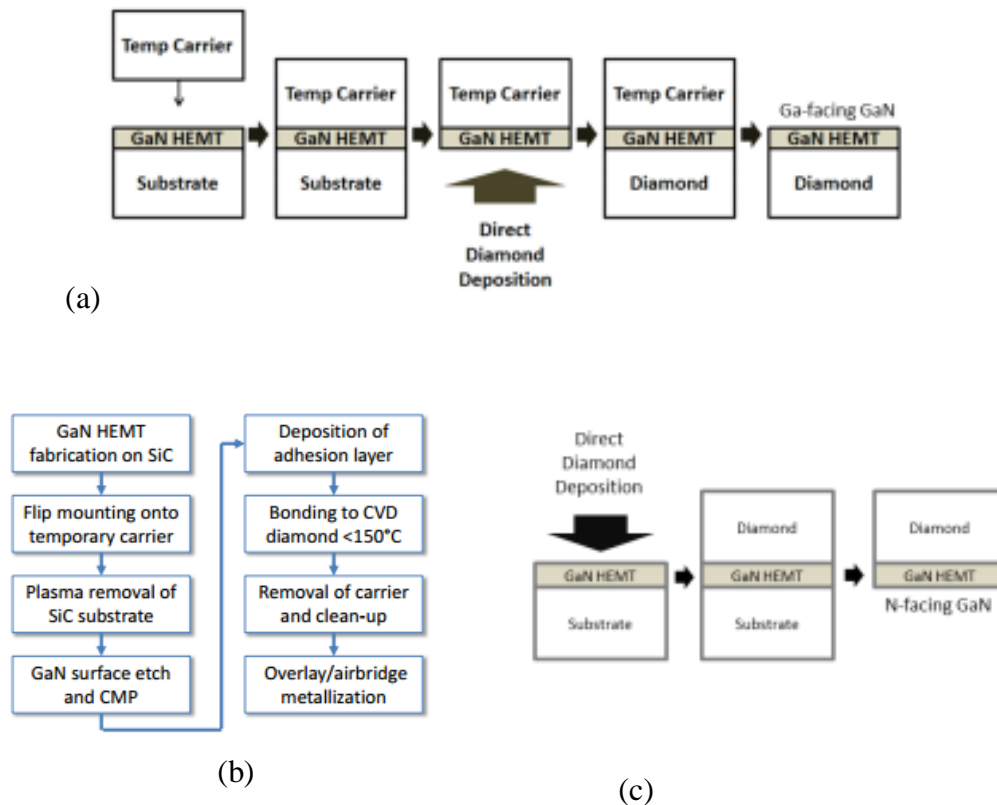


Figure 5.4 Schematic process flows for incorporating diamond as a heat spreader for AlGaN/GaN HEMTs: (a) direct growth of diamond on the back side of the GaN buffer layer after the substrate and the TLs have been etched, while bonding a temporary handle wafer at the front side using wafer bonder, (b) low temperature wafer bonding of diamond with dielectric adhesion layer grown on the GaN buffer back side epilayer, and (c) the direct approach of diamond growth on the front side of the epilayers after subsequent growth of a dielectric layer for seeding adhesion. <sup>74,76</sup>

### 5.3 Effect of TBR on GaN-on-diamond performance

Effective heat spreading within a GaN-on-diamond wafer does not solely depend on the thermal conductivity of CVD diamond, but also the effective thermal boundary resistance ( $TBR_{eff}$ ) at the interface of GaN and diamond.<sup>82,84</sup> This  $TBR_{eff}$  is the effect of acoustic mismatch between materials which includes the dielectric interlayer used for diamond growth seeding, and the defective transition region at the dielectric layer/diamond interface, also referred to as the nucleation layer, or nano crystalline diamond (NCD) layer.<sup>84</sup> Therefore,  $TBR_{eff}$  is not the discrete boundary resistance but it is a collective contribution of multiple resistance components: i) The thermal resistance of low-quality GaN regions near the dielectric adhesion layer/diamond interface,  $R_{Br}(GaN)$ , ii) the two boundary resistances at the adhesion layer interfaces with the GaN and the diamond,  $R_{Br}(GaN - dielectric + dielectric - diamond)$ , iii) the internal thermal resistance of the dielectric adhesion layer,  $R_{Br}(dielectric)$ , and iv) the thermal resistance of near interfacial diamond,  $R_{Br}(NCD)$ . All these resistances lump together to give the effective thermal boundary resistance ( $TBR_{eff}$ ),<sup>79</sup>

$$TBR_{eff} = R_{Br}(GaN - dielectric) + R_{Br}(dielectric - diamond) + \frac{d_{dielectric}}{k_{dielectric}} + R_{Br}(NCD) \quad (5.1)$$

$$Or, TBR_{eff} = R_0 + \frac{d_{SiNx}}{k_{SiNx}} \quad (5.2)$$

$$[ R_0 = R_{Br}(GaN - dielectric) + R_{Br}(dielectric - diamond) + R_{Br}(NCD) ]$$

Where,  $d_{dielectric}$  is the thickness of the dielectric adhesion layer and  $k_{dielectric}$  is the thermal conductivity of the dielectric adhesion layer. From equation (5.2), it is clearly evident that  $TBR_{eff} \propto d_{dielectric}$ ;  $TBR_{eff} \propto 1/K_{dielectric}$ , therefore using a ultra-thin dielectric layer with better thermal conductivity is key to minimizing  $TBR_{eff}$ .

Reported measured values suggest that  $TBR_{eff}$  for GaN-on-diamond ranges from 10 to 50 m<sup>2</sup>K/GW<sup>16,19,76,84–86</sup> which are low in comparison to GaN-on-SiC and GaN-on-Si.<sup>73</sup> But to realize the full potential of the GaN-on-diamond system,  $TBR_{eff}$ , which constitutes a significant portion of the overall wafer thermal resistance, must be minimized.

To date, the reported choice of dielectric adhesion layer for diamond seeding to facilitate diamond growth is SiN<sub>x</sub>, with thickness ranging from 28 nm to 100 nm.<sup>20,84,86</sup> Using SiN<sub>x</sub> as a dielectric adhesion layer, J. Cho et al., showed that  $TBR_{eff}$  is dominated by the effective thermal resistance of SiN<sub>x</sub>,  $R_{Br}(dielectric)$  in this case,  $R_{Br}(SiNx)$ .<sup>20</sup> **Table 5.1** summarizes the published extracted thermal resistance of different samples measured by time domain thermoreflectance (TDTR). The minimum  $TBR_{eff}$  resistance is found to be 17.5 m<sup>2</sup>K/GW for the thinnest SiN<sub>x</sub> layer, and most importantly, the contribution to effective thermal resistance for dielectric adhesion layers  $R_{th}(SiNx)$  is almost 80% for both cases (either SiN<sub>x</sub> on GaN or SiN<sub>x</sub> on diamond).<sup>20</sup> This is because the extracted thermal conductivity of the dielectric layer was very low, ranging from  $k_{dielectric} = 0.94$  Wm<sup>-1</sup>K<sup>-1</sup> to 1.1 Wm<sup>-1</sup>K<sup>-1</sup>, compared to the measured thermal conductivity for GaN,  $k_{GaN} = 170 \pm 10$  Wm<sup>-1</sup>K<sup>-1</sup>, and for diamond,  $k_{diamond} = 1500 \pm 10$  Wm<sup>-1</sup>K<sup>-1</sup>.<sup>20</sup> This result suggests that reducing the thermal resistance of the dielectric layer could result in the optimal total reduction of  $TBR_{eff}$  which would lead to maximum extraction of the dissipated heat energy and, thus, realizing the highest performance GaN-on-diamond

device. Sun et al. varied the  $\text{SiN}_x$  thickness to verify that the dielectric layer thickness has a linear relation with TBR. **Figure 5.5** shows  $TBR_{eff}$  as a function of the dielectric layer thickness,  $d_{dielectric}$ . Here the solid squares represent the  $TBR_{eff}$  for hot filament (HF) CVD diamond, and the solid circles are for microwave (MW) CVD growth.

Table 5.1. Extracted thermal properties of  $\text{SiN}_x$  on diamond and GaN samples measured at room temperature using TDTR.  $R_{Br(Al-SiN)}$  represents the Al- $\text{SiN}_x$  TBR,  $R_{Br(SiNx)}$  represents the effective  $\text{SiN}_x$  resistance and  $TBR_{eff}$  represents the total summed resistance of  $R_{Br(Al-SiN)}$  and  $R_{Br(SiNx)}$ .<sup>20</sup>

Sample		$R_{Br(Al-SiN)}$ $\text{m}^2\text{K/GW}$	$R_{Br(SiNx)}$ $\text{m}^2\text{K/GW}$	$TBR_{eff}$ $\text{m}^2\text{K/GW}$
On Diamond	13 nm $\text{SiN}_x$	N/A	N/A	$17.5 \pm 0.6$
	24 nm $\text{SiN}_x$	$4.8 \pm 0.2$	$21.6 \pm 0.7$	$26.4 \pm 0.9$
	36 nm $\text{SiN}_x$	$5.5 \pm 0.3$	$36.8 \pm 0.8$	$42.3 \pm 1.1$
On GaN	12 nm $\text{SiN}_x$	N/A	N/A	$17.2 \pm 0.7$
	23 nm $\text{SiN}_x$	$7.5 \pm 0.2$	$22.0 \pm 0.9$	$29.5 \pm 1.1$
	35 nm $\text{SiN}_x$	$5.3 \pm 0.3$	$37.3 \pm 1.5$	$42.6 \pm 1.8$

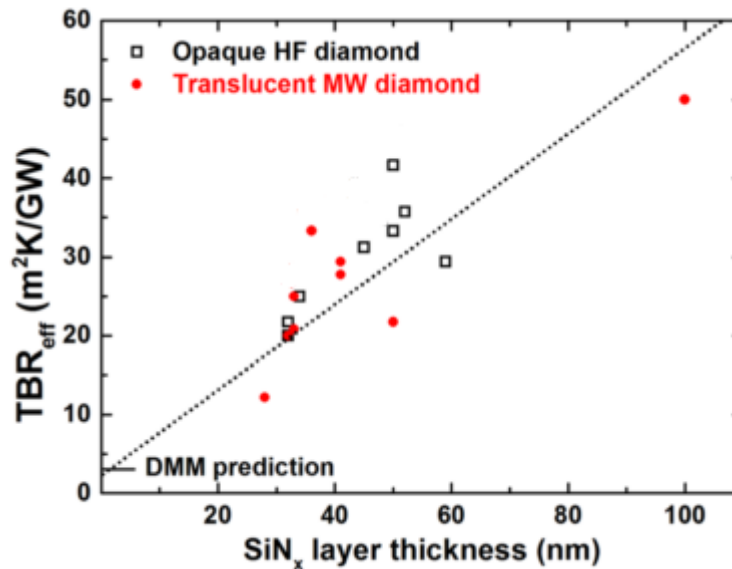


Figure 5.5  $TBR_{eff}$  of GaN-on-diamond as a function of the  $\text{SiN}_x$  layer thickness. The data broadly follow a linear fit and the thermal conductivity of the amorphous  $\text{SiN}_x$  layer is estimated to be  $1.9 \pm 0.4 \text{ W/m-K}$  from the slope.<sup>84</sup>

#### 5.4 Proposed Solution:

Considering the studies discussed above, the effective thermal boundary resistance

$TBR_{eff}$  can be reduced by either,

- i) Reducing the thickness ( $d_{dielectric}$ ) of the dielectric adhesion layers (see Eq (5.2)),
- ii) Finding new material(s) other than  $SiN_x$  with better thermal conductivity ( $k_{dielectric}$ ) and adhesion property, and/or
- iii) Obtaining the thinnest possible diamond nucleation layers or nano crystalline diamond layer.

This dissertation will focus on the first approach listed above.

## 6 STRUCTURAL AND INTERFACE ANALYSIS OF DIAMOND ON AlGaN/GaN HEMT UTILIZING AN IN-SITU SiN<sub>x</sub> INTERLAYER GROWN BY MOCVD

### 6.1 Introduction

For GaN-based HEMTs, the high current driven through the channel is confined to the very narrow, < 10 nm, 2DEG and therefore produces significant self-heating (as high as 350 °C for GaN on Si) in the active region of the device.<sup>16</sup> Since the 2DEG and the active GaN/AlGaN layers are very thin, the dissipation of heat from the self-heating source is predominantly vertical.<sup>16</sup> Therefore, a low resistance thermal pathway from the self-heating source to a nearest heat sink (e.g., a high thermally conductive substrate) is highly desired.

Owing to its outstanding bulk thermal conductivity, which can exceed 2000 W/m-K,<sup>87</sup> CVD polycrystalline diamond is the superior choice as a heat spreading material, especially when compared with standard GaN-based substrates such as Si, 6H-SiC and Al<sub>2</sub>O<sub>3</sub>. Altman et al. used diamond as a substrate to show a 2.7X reduction in the thermal resistivity and 3X increase in device areal density compare to GaN-on-SiC devices.<sup>88</sup> To achieve maximum benefit of diamond heat spreading, the diamond thin film must be in direct contact with the HEMT stack, and most preferably to the topmost AlGaN barrier layer nearest the device active region.

Inclusion of a diamond heat spreader with the AlGaN/GaN HEMT can be realized in different ways. One approach is to replace the original III-Nitride growth substrate by

wafer bonding of a diamond substrate to the AlGaIn/GaN HEMT. A second approach is direct growth of diamond on the back (GaN) side of the wafer.<sup>49,74,86</sup> In both approaches, discussed in detail in Chapter 5, additional processing steps are required, such as transfer to a handle wafer, substrate removal, wafer bonding, and/or handle wafer removal. The electrical, chemical, and thermal properties (thermal conductivity of diamond and thermal boundary resistance)<sup>74,88</sup> of the GaN-diamond interfaces have been extensively studied with these approaches.

A third approach to achieve the desired diamond integration is directly growing the CVD diamond layer on the epi-side (top AlGaIn surface) of the passivated active layer.<sup>89–97</sup> Challenges to diamond-on-AlGaIn/GaN growth include degradation of III-Nitride layers in the harsh CVD environment<sup>98</sup> and thermal stresses due to the mismatch of the materials' TECs.<sup>38</sup> Changes in the stress-strain state in this AlGaIn/GaN heterostructure, especially in the fully strained pseudomorphically grown AlGaIn barrier layer, could have a significant impact on the 2DEG properties<sup>24</sup>. Previous reports, such as A. Wang et al<sup>97</sup>, have shown the overall impact of stress due to high temperature CVD diamond cap integration with a dielectric adhesion layer through simulation (thermal stress on GaN, SiN<sub>x</sub> and Diamond) and Raman measurements (bulk GaN). The strain in pseudomorphically grown AlGaIn barrier layers acts differently than that of bulk GaN. Therefore, for a proper understanding of the impact of CVD diamond integration induced stress-strain state on the 2DEG properties, the barrier layer stress should be evaluated. However, this cannot be done exclusively with Raman. Using direct diamond growth, a 25% improvement in breakdown voltage<sup>99</sup> and a 20% lower channel temperature at equivalent power dissipation have been reported.<sup>96</sup> Zhou et al. predicted that a 15%

reduction in self-heating for devices based on similar material stacks can be realized with CVD diamond grown on the HEMT structure.<sup>93</sup> While the potential effectiveness of this approach is very promising, detailed studies of the diamond-AlGaN/GaN interface properties, as well as the impact of the diamond growth on the III-Nitride materials, requires further investigation.

In this chapter, *in-situ* SiN<sub>x</sub> grown by MOCVD immediately following the AlGaN/GaN HEMT growth is reported. Subsequently, CVD diamond deposition is conducted in Texas State's HFCVD growth system. The impact on the material properties (stress/strain state) of the III-Nitride layers before and after diamond growth by high-resolution x-ray diffraction (HRXRD) based reciprocal space mapping (RSM), and from visible and ultraviolet (UV) micro-Raman measurements was evaluated. HRXRD based RSM measurements around the GaN (10-14) asymmetric peak allowed accurate calculations of the in-plane barrier layer strain thereby obtaining a more accurate stress-strain profile of the AlGaN/GaN heterostructure than characterizing by only Raman (which cannot resolve the AlGaN barrier layer, separately). The details of the measurement approaches are discussed in Chapter 2. Scanning transmission electron microscopy (STEM) imaging was performed to evaluate the structural and elemental properties of the *in-situ* SiN<sub>x</sub> passivated AlGaN/GaN HEMT interface before and after the diamond growth. Finally, time domain thermoreflectance (TDTR) was performed to evaluate the thermal conductivity of the CVD diamond and the effective thermal boundary resistance (TBR<sub>eff</sub>) of the diamond/GaN interface.

## 6.2 Experimental Details

**Figure 6.1(a)** shows a schematic diagram of the target diamond-on-AlGaN/GaN HEMT structure. First, *in-situ* SiN<sub>x</sub> passivated AlGaN/GaN HEMT was grown on Si (111) by MOCVD as discussed in Chapters 2-4. For the experimental wafers, SiH<sub>4</sub> was introduced to the chamber while keeping the same temperature and chamber pressure (100 Torr) of the GaN cap layer to produce the ~ 46 nm thick *in-situ* SiN<sub>x</sub> layer.

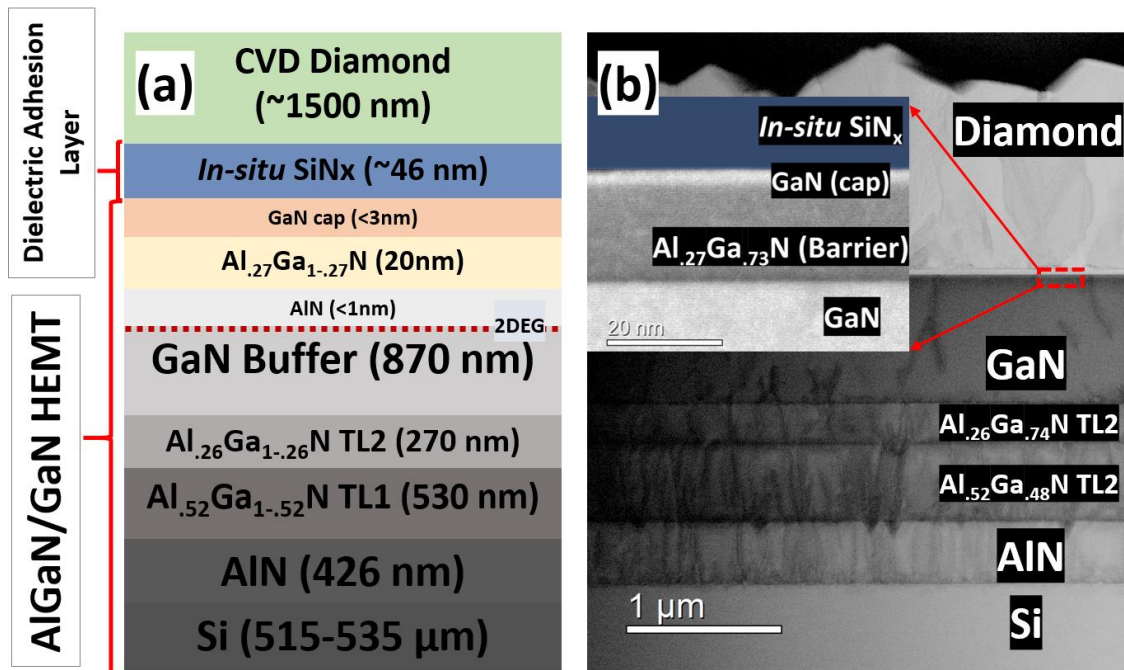


Figure 6.1 (a) Schematic of the target diamond-on-AlGaN/GaN HEMT structure using MOCVD grown *in-situ* SiN<sub>x</sub> as the dielectric adhesion layer (not drawn to the scale), and (b) Bright-field STEM images of the structure after diamond growth. Inset indicates the *in-situ* SiN<sub>x</sub>/GaN(cap)/AlGaN(barrier)/GaN interface region, post diamond growth.

For the diamond CVD process, nano-diamond seeds were dispersed using a photoresist based spin coating technique as reported by Ahmed *et al.*<sup>100</sup> A power of 6 kW was driven through an array of 9 tungsten wires of 0.01" diameter, which resulted in a 2200 °C wire filament temperature. The rotating substrate was positioned 6 mm from the tungsten wire

array to produce a substrate temperature of 720-750 °C and uniform diamond growth rate. Growth was carried out for 7 h using 60 sccm of methane and 3 sccm of oxygen with 2000 sccm of hydrogen into the HFCVD chamber while maintaining a pressure of 20.8 Torr. As discussed below, this process resulted in  $1.46 \pm 0.10 \mu\text{m}$  thick fully coalesced diamond and uniform coverage across the wafer.

X-ray reflectometry (XRR) of the *in-situ* SiN<sub>x</sub> was performed to determine the initial thickness and density of the MOCVD grown SiN<sub>x</sub> dielectric adhesion layer. HRXRD RSM was performed around both the GaN asymmetric (10-14) and symmetric (0002) planes to determine the stress and composition of the constituent layers before and after diamond deposition. Tapping mode AFM measurements of the *in-situ* SiN<sub>x</sub> surface, before diamond growth, and of the diamond surface after growth were taken to evaluate roughness and grain size. Visible (532 nm) and UV (363.8 nm) micro-Raman measurements were performed to evaluate the structural and interface properties of III-Nitride layers and to ascertain the effects on the GaN before and after diamond growth.<sup>37</sup> Bulk samples were used to determine the GaN (TDI, Inc.) and AlN (Crystal IS) reference phonon energies. Further details of the measurements are given in previous chapters, and can also be found elsewhere.<sup>37,38</sup>

STEM was used to analyze the interface characteristics and layer thicknesses before and after diamond deposition. Cross-sectional samples were prepared using standard focused ion beam (FIB) techniques using a FEI Helios Nanolab 400 DualBeam system by first depositing a protective Pt layer and milling using a 30 kV accelerating voltage. A final polishing step was then performed with an accelerating voltage of 2 kV to remove surface damage. Bright-field and high-angle annular dark-field (HAADF) images of the

samples, as well as electron energy loss spectroscopy (EELS), were collected using a JEOL ARM 200F operating at 200 kV.

Finally, time domain thermoreflectance (TDTR) measurements<sup>101</sup> were performed to evaluate the diamond/GaN thermal boundary resistance (TBR) and the thermal conductivity of the polycrystalline diamond. To perform the TDTR, a 96 nm layer of Al was deposited by e-beam evaporation at room temperature.

### 6.3 Results and Discussion

**Figure 6.2** shows specular x-ray reflection from the SiN<sub>x</sub>/ GaN (cap)/ AlGaN (Barrier)/ AlN (profile)/ GaN layer structure, prior to diamond growth. The data exhibit well defined periodic Kiessing fringes and are modeled using layer thicknesses, interface roughness, and material density of each layer as parameters. (Rigaku GlobalFit, which incorporates both optimization and least-square refinement, discussed in Chapter 2 and published elsewhere.<sup>50</sup> The layer thicknesses were determined to be 45.9±0.1 nm for SiN<sub>x</sub>, 0.5±0.1 nm for the GaN cap, and 20.4±0.1 nm for the AlGaN barrier.

The SiN<sub>x</sub> density obtained from the model, 3.47 gm-cm<sup>-3</sup>, is higher than that of plasma enhanced chemical vapor deposition (PECVD) SiN<sub>x</sub> (2.0 - 2.8 gm-cm<sup>-3</sup>) as reported by Huang *et al.*<sup>102</sup> and low pressure chemical vapor deposition (LPCVD) SiN<sub>x</sub> (2.9 - 3.1 gm-cm<sup>-3</sup>) reported by Stoffel *et al.*<sup>103</sup>, while comparable to MOCVD SiN<sub>x</sub> (3.6-3.8 gm-cm<sup>-3</sup>) reported by Gamarra *et al.*<sup>55</sup> The derived growth rate for the *in-situ* MOCVD SiN<sub>x</sub>

was  $\sim 2$  nm/min. From XPS surface stoichiometric analysis,  $x = [\text{N}]/[\text{Si}]$  for this  $\text{SiN}_x$  layer was found to be 1.13.

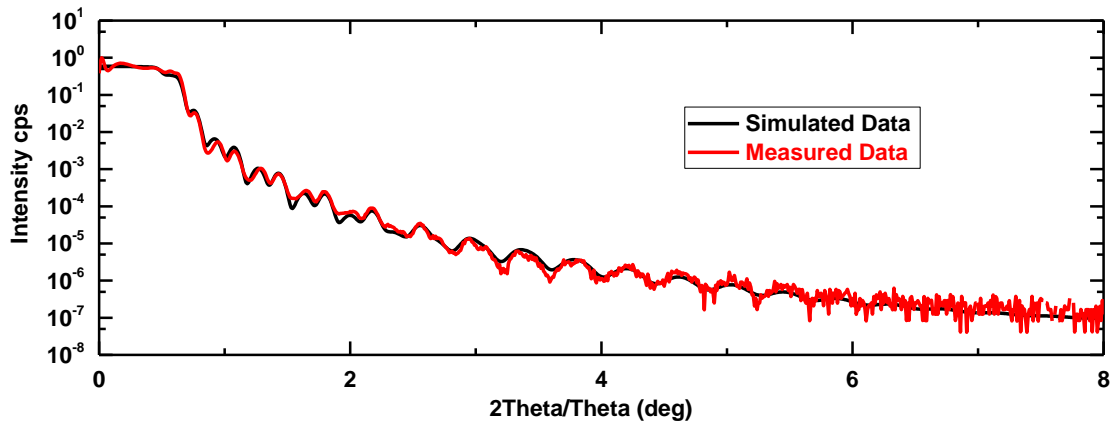


Figure 6.2 Measured and simulated grazing incidence x-ray reflectivity of the *in-situ*  $\text{SiN}_x$  passivated III-Nitride HEMT heterostructure.

**Figure 6.3(a)** shows a  $5 \mu\text{m} \times 5 \mu\text{m}$  AFM image of the *in-situ*  $\text{SiN}_x$  surface before diamond deposition. Very smooth step-flow growth surface morphology is obtained with RMS roughness ( $R_q$ ) of 0.43 nm. **Figure 6.3(b)** shows a  $10 \mu\text{m} \times 10 \mu\text{m}$  AFM image of the diamond surface after 7 h growth. Coalesced diamond coverage is confirmed. The RMS surface roughness is 92.4 nm while the average grain size and distribution calculated by the linear intercept method was  $0.73 \pm 0.32 \mu\text{m}$ , for this  $1.25 \pm_{0.12}^{0.12} \mu\text{m}$  thick diamond film (measured from STEM).

#### 6.4 HRXRD results

HRXRD measurements were used to determine whether the underlying III-Nitride layers have been protected during 7 h of diamond growth in the HFCVD environment. HRXRD 2-Theta/Theta scans in **Figure 6.4** show the diffraction patterns before and after diamond growth. The III-Nitride (GaN, AlN, TL1, and TL2) second order (0002) diffraction peaks are present and have not substantially changed before and after diamond growth. This confirms that the III-Nitride layers beneath the AlGaN barrier layer are fully

protected by the *in-situ* SiN<sub>x</sub> passivation layer during diamond CVD. Following diamond growth, the corresponding diamond (111) diffraction peak is present at 43.90°. The FWHM of the GaN (0002)  $\omega$ -scan, before and after growth, are 587±1 and 598±1 arcsec, respectively. This 2 % increase, post diamond growth compared to pre growth, is

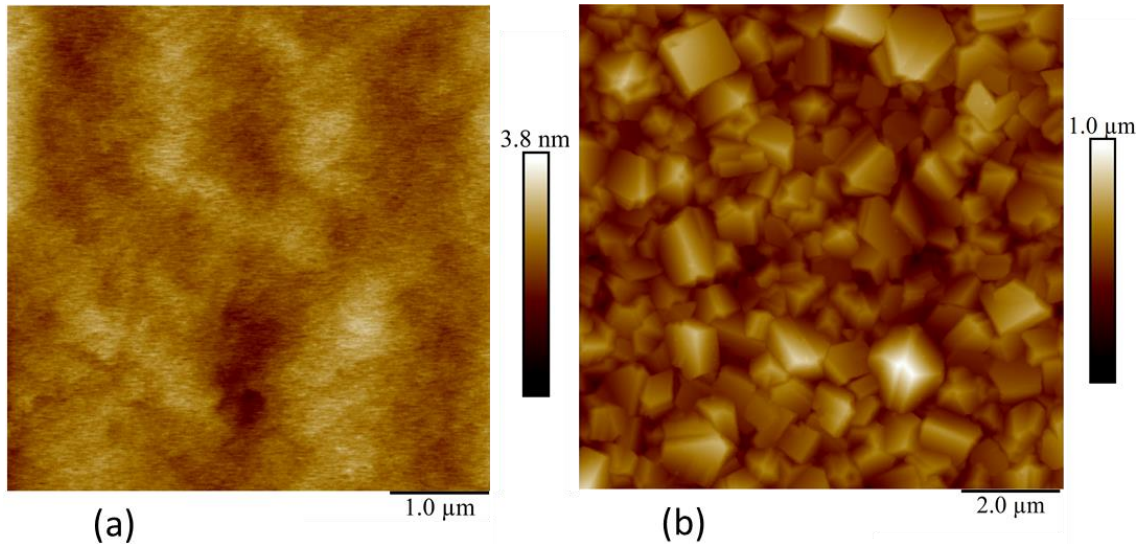


Figure 6.3 AFM images of (a) 5  $\mu\text{m}$  x 5  $\mu\text{m}$  *in-situ* SiN<sub>x</sub> surface, and (b) 10  $\mu\text{m}$  x 10  $\mu\text{m}$  diamond surface confirming the smooth, continuous *in-situ* SiN<sub>x</sub> surface and fully coalesce diamond film.

consistent with similar *in-situ* SiN<sub>x</sub> passivated HEMT structures (600 arcsec) grown by MOCVD as reported by M. Germain *et al.*<sup>14</sup>

Since the strained barrier layer (Al<sub>0.27</sub>Ga<sub>0.73</sub>N) has similar composition as TL2 (Al<sub>0.26</sub>Ga<sub>0.74</sub>N), the symmetric (0002) HRXRD scan cannot independently resolve the barrier layer as they have nearly identical interplanar spacings along the *c*-axis. Therefore, RSM around the asymmetric (10-14) plane was performed to analyze the strained AlGa<sub>N</sub> barrier layer, as described in detail in Chapter 2. **Figure 6.5** presents the HRXRD RSM data before (left) and after (right) diamond deposition. The XRD goniometer was first

normalized to the GaN (10-14) peak. The data are presented in a contour representation of diffraction intensity in reciprocal space coordinates  $Q_{(hkl)z}$  and  $Q_{(hkl)x}$ . Peak positions in this coordinate system are readily converted into interplanar spacing ( $d_z$ ,  $d_x$ ), and hence the lattice constants ( $c$ ,  $a$ ). The details of the lattice constant determination have been discussed in Chapter 2. The vertical dotted line in each panel represents the zero-relaxation line across the GaN  $a$ -axis. For an AlGaN barrier layer grown pseudomorphically on GaN, the barrier layer peak (within the dotted ellipse) lies on the zero-relaxation line. The diffraction peaks from the AlN, TL1, and TL2 layers lie on the right side of the zero-relaxation line corresponding to partially or fully relaxed material.

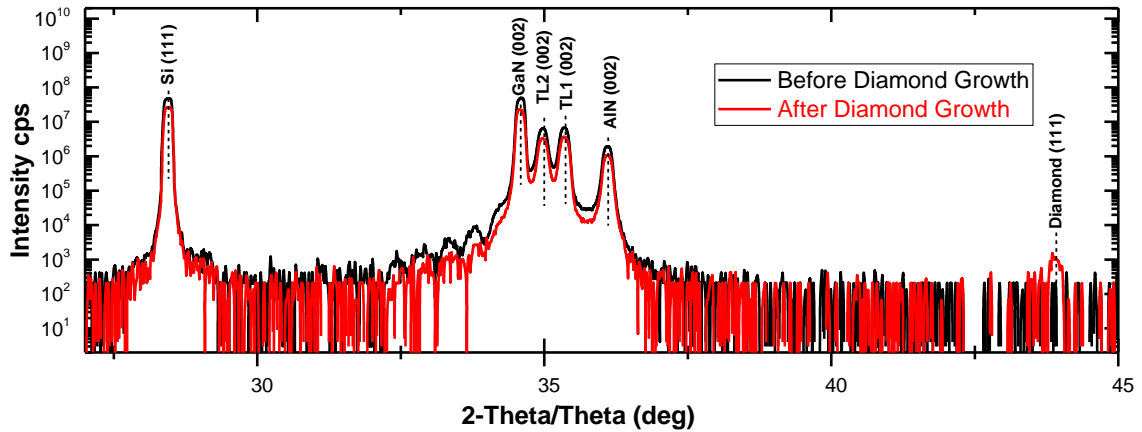


Figure 6.4 HRXRD 2-Theta/Theta spectrum of the AlGaN/GaN structure on Si (111) before and after diamond growth.

The measured lattice parameters  $c_m(x)$  were determined from RSM around the GaN (0002) reflection and lattice parameters  $a_m(x)$  from RSM around the GaN (10-14) reflection (see **Figure 6.5**). By solving Eq. (2.22), the AlN mole fraction for the fully strained AlGaN barrier layer was determined to be  $x = 27\%$ . By determining the exact  $x$  value for the strained barrier layer,  $\epsilon_{xx}$  and  $\epsilon_{zz}$  were determined and are presented in **Table 6.1**.

With the lattice parameters and elastic constants taken from **Table 2.2**, biaxial stresses in the AlN and GaN layers are determined. Vegard's law is employed for the barrier layer material using the AlN mole fraction ( $x = 27\%$ ) discussed earlier. Biaxial stresses for GaN, AlN and the strained barrier layer, using Eq. (2.27-28) are included in **Table 6.1**. Measured uniaxial lattice strain  $\varepsilon_{xx}$  in the pseudomorphic barrier layer is +0.769 % (tensile). The strain in the GaN, AlN, and barrier layers were in reasonable agreement with published reports.<sup>30,36</sup> The uniaxial strain in the GaN buffer and AlN nucleation layers are tensile in nature and arise from the TEC mismatch with the much thicker Si substrate. The measured  $\varepsilon_{zz}$  strain for the III-Nitride layers are compressive, as opposed to the in-plane strain.

Using an analytical approach as reported by Anwar et al.<sup>104</sup> piezoelectric and spontaneous polarization for the AlGaIn barrier ( $P_{PE(Barrier)}$ ,  $P_{SP(Barrier)}$ ) and GaN buffer layer ( $P_{SP(GaN)}$ ) have been calculated from XRD determined parameters represented in **Table 6.2**. There is a 3% change in the barrier layer biaxial strain state observed before and after diamond growth. The piezoelectric polarization before the diamond growth is  $P_{PE(Barrier)} = -0.00945 \text{ C/m}^2$  while the post diamond  $P_{PE(Barrier)} = -0.00906 \text{ C/m}^2$ . Finally, the total 2DEG sheet charge density  $N_s$  has been calculated before and post diamond deposition. Total 2DEG sheet charge density induced before the diamond deposition is found to be  $1.04\text{E}+13 \text{ cm}^{-2}$  while the sheet charge density after the diamond deposition was found to be  $0.994\text{E}+13 \text{ cm}^{-2}$ , which is a 4.5% reduction, pre-diamond deposition. To check the confidence of the measured parameters, uncertainty analysis was performed considering the different sources of uncertainty while determining the RSM peak positions. For the SmartLab Rigaku system with optical precision  $\leq 4 \text{ arcsec}$ , the instrumental contribution

to the uncertainty in determining 2-theta position (and interplanar spacing) is negligible, however, uncertainty arises from the step size in  $\omega$ -space ( $0.03^\circ$ ).

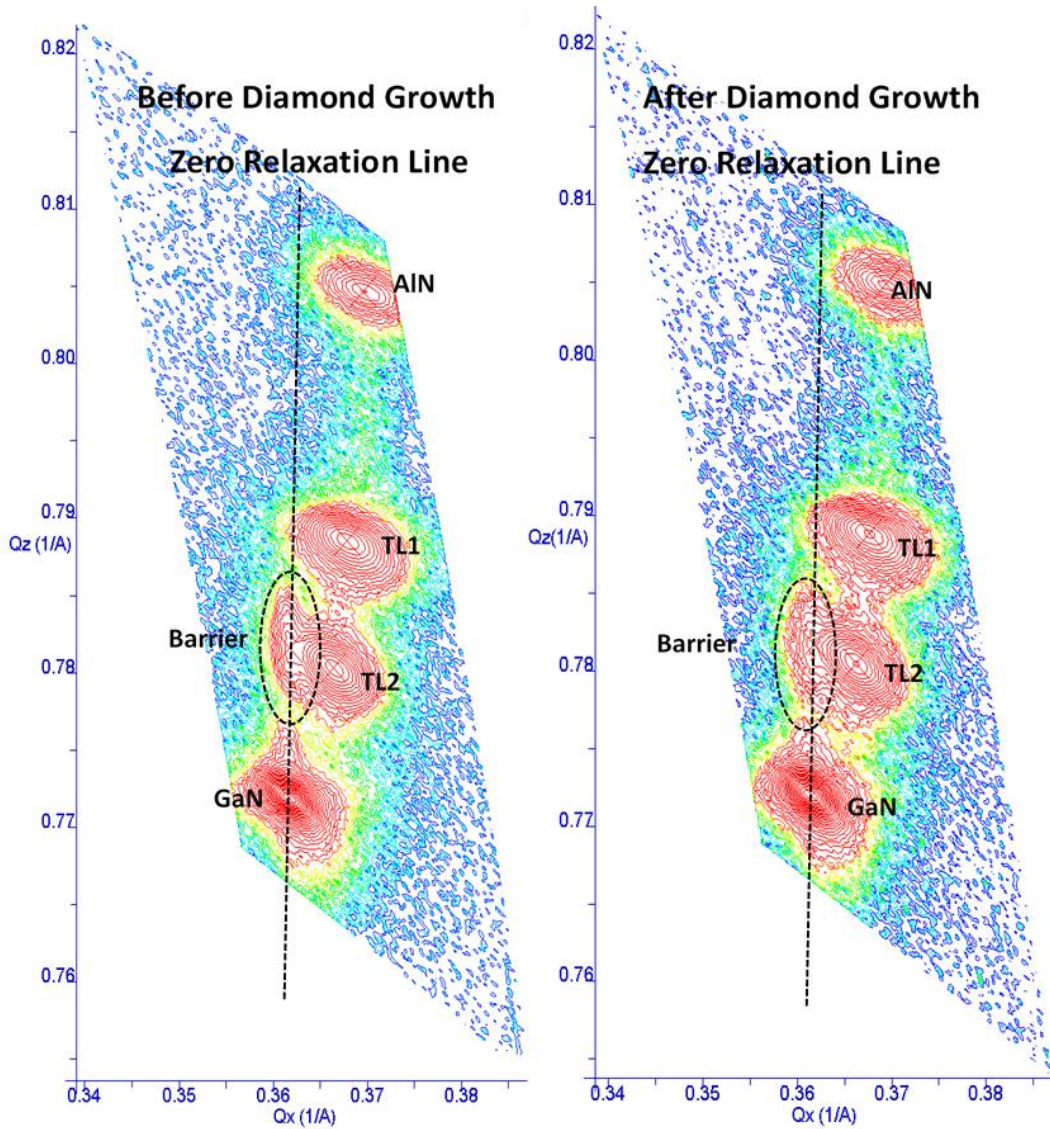


Figure 6.5 RSM contour plots of the AlGaIn/GaN HEMT wafers with AlN, GaN, TL1 ( $\text{Al}_{0.51}\text{Ga}_{0.49}\text{N}$ ), TL2 ( $\text{Al}_{0.26}\text{Ga}_{0.74}\text{N}$ ) and barrier layer ( $\text{Al}_{0.27}\text{Ga}_{0.73}\text{N}$ ) reflections collected around their asymmetric (10-14) planes. The dotted line indicates the zero-relaxation line along the crystallographic  $a$ -axis. The dotted ellipses highlight the strained barrier layer peaks. The axes are converted to  $Q_z$  and  $Q_x$  reciprocal coordinates ( $Q_z = 1/d_z$ ;  $Q_x = 1/d_x$ ). The color scheme shows the variation in intensity of the diffracted beam, with red represents the highest diffraction intensity while blue represents the lowest.

The maximum uncertainty is estimated using the half-width half-maximum (HWHM) of the GaN buffer layer peaks (prior to diamond deposition) in reciprocal space. First, for biaxial strain, the biaxial stress uncertainty is 0.0003 GPa, or 0.05 % of the determined 0.58 GPa value. On the other hand, the uncertainty for determining hydrostatic strain is 8X its calculated value, again, based on the HWHM. Because the hydrostatic strain component is small ( $< 0.1$  %, discussed previously), we conclude that the measurement uncertainty is insignificant.

Table 6.1 Measured lattice parameters along both  $a$ -axis and  $c$ -axis, calculated uniaxial strain, hydrostatic and biaxial stress from the measured lattice parameters, before and after diamond growth.

	Before Diamond Growth							
	Measured lattice constant ( $\text{\AA}$ )		Measured Strain (%)		Hydrostatic Strain	Biaxial Strain (%)		Biaxial Stress (GPa)
	$a$	$c$	$\epsilon_{xx}$	$\epsilon_{zz}$	$\epsilon_h$ (%)	$\epsilon_{xx}^b$	$\epsilon_{zz}^b$	$\sigma_{bs}$
Barrier	3.1911	5.1178	0.769	-0.265	0.099	0.669	-0.365	3.16
GaN	3.1926	5.1827	0.115	-0.071	-0.006	0.121	-0.065	0.58
AlN	3.1232	4.9720	0.327	-0.201	0.007	0.334	-0.193	1.57
	After Diamond Growth							
Barrier	3.1913	5.1178	0.712	-0.288	0.064	0.648	-0.352	3.06
GaN	3.1932	5.1813	0.133	-0.098	-0.018	0.151	-0.080	0.72
AlN	3.1229	4.9709	0.350	-0.198	0.008	0.326	-0.189	1.53

The uncertainty resulting from the empirical values of the elastic constants ( $C_{11}$ ,  $C_{12}$ ,  $C_{13}$ ,  $C_{33}$ ) was also considered, analogous to the approach discussed in Chapter 2. Published elastic constants used here vary up to 19 % as reported in the literature by Vurgaftman *et al.*<sup>43</sup> and by Wright *et al.*<sup>53</sup>, and shown in **Table 2.2**. This results in a

biaxial stress uncertainty of  $\pm 0.07$  GPa, which is 10 % of the determined GaN (post diamond growth) biaxial stress value of 0.72 GPa, given in **Table 6.1**. From this analysis, and using the worst-case uncertainty based on the elastic constants, the change in biaxial tensile stress before ( $0.58\pm 0.05$  GPa) to after ( $0.72\pm 0.07$  GPa) diamond deposition is outside the bounds of the experimental uncertainty. Thus, we conclude that there is an increase in the stress due to diamond deposition. Nevertheless, this increase in stress is still significantly below the critical tensile stress ( $> 20$  GPa) for material deformation.<sup>105</sup> Micro-Raman results

**Figure 6.6** shows UV (a) and visible (b) micro-Raman spectra for the HEMT stack prior to and following diamond growth. Due to the shallow optical penetration depth ( $\leq 100$  nm) in the GaN,<sup>38</sup> the UV spectra exhibit scattering from the thick buffer layer only. Observed are  $E_2^2$ - and  $A_1(LO)$ -symmetry phonons along with second-order quasi- $E_1(LO)$  band<sup>106</sup> at  $1476.2$   $\text{cm}^{-1}$ . Scattering from the GaN layer is strong when using 363.8-nm excitation due to resonance with the direct band gap. The high background in the UV spectra arises from GaN photoluminescence (PL). Post diamond deposition, we see the characteristic  $O(\Gamma)$ -symmetry phonon at  $1332$   $\text{cm}^{-1}$  and, since diamond is transparent at this wavelength, the GaN buffer layer. This diamond peak appears relatively weak due to the strong resonance with the GaN. Since the III-Nitride layers and diamond are transparent to visible light, Raman spectra obtained with this excitation allow the entire material stack to be probed. Consequently, these measurements provide an average property throughout the individual layers. The visible micro-Raman spectra are presented in **Figure 6.6(b)**, we observe GaN  $E_2^2$  and  $A_1(LO)$  phonons, the AlN  $E_2^2$  band, and, post diamond deposition, the associated  $O(\Gamma)$  line.

The  $E_2^2$  peak positions in GaN and AlN layers are sensitive to stress, while the  $A_1(LO)$  position and width are also sensitive to free-carrier concentration. Peak positions and line widths were determined by fitting the data using the Lorentzian function. Results are summarized in **Table 6.2**. For the  $E_2^2$  peak position and shift relative to our measured bulk values for GaN and AlN, the red shift in each case corresponds to biaxial tensile stress.<sup>49</sup> This agrees with the XRD results and, as discussed above, is primarily attributed to TEC mismatches for each layer and the much thicker Si substrate. Shifts in the GaN  $E_2^2$  peak positions, relative to the reference material, are consistent in the visible and UV measurements. This consistency applies to the pre- and post-diamond growth comparison.

Similarly, for the AlN  $E_2^2$  band in the visible Raman spectra is consistent prior and post diamond growth. Stress estimates from the Raman measurements may be obtained from the  $E_2^2$  peak shifts using published stress factors,<sup>44,48,107,108</sup> which vary between reports for both GaN and AlN. For comparing with the XRD stress values presented in **Table 6.1**, the Raman-stress factor  $4.2\pm 0.3$  cm<sup>-1</sup>/GPa of Kisielowski et al.<sup>44</sup> was used. From the visible Raman, a stress value of  $0.76\pm 0.06$  GPa was obtained prior to diamond growth which is close to being within the total error of the XRD result for  $\sigma_{bS} = 0.58\pm 0.07$  GPa. Following diamond growth, stress estimated from the Raman measurement is  $0.80\pm 0.06$  GPa which is within the total error of the XRD value of  $\sigma_{bS} = 0.72\pm 0.07$  GPa. Similarly, the stress estimated for AlN depends strongly on the Raman stress factor and ranges from  $1.36\pm 0.32$  to  $0.95\pm 0.22$  GPa.<sup>108</sup> These are slightly lower than the XRD values presented in **Table 6.1**. Discrepancies in the reported stress factors and elastic coefficients may be attributable to differences in defect densities in the III-Nitride layers investigated

by the respective teams, which has an impact on the strain values, particularly  $\varepsilon_h$ , and the Poisson ratio.<sup>44,51</sup>

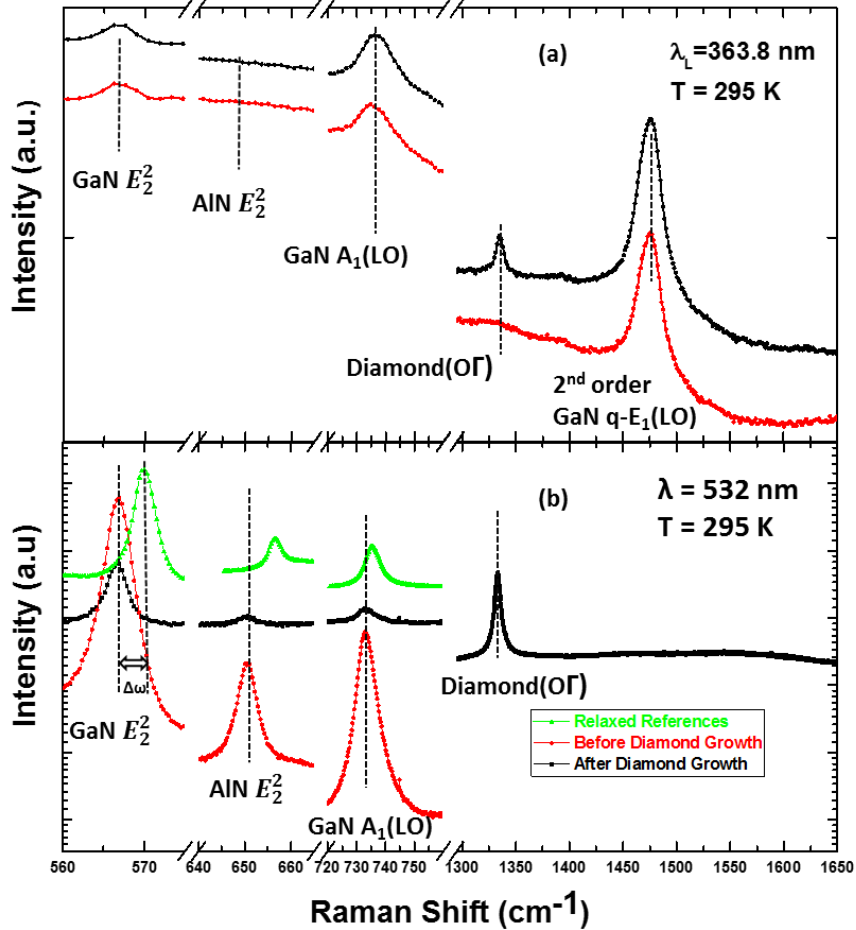


Figure 6.6 Ultraviolet (a) and visible (b) Raman spectra of the AlGaIn/GaN HEMT taken before and after diamond growth. Detailed spectra of  $E_2^2$  (GaN, AlN) and  $A_1(LO)$  (GaN) showing phonon redshift.

The primary conclusion from the Raman  $E_2^2$  measurements is consistency seen in values obtained from the GaN and AlN layers prior to and following the growth of the *in-situ* SiN<sub>x</sub> and diamond layers. Shifts measured for the  $A_1(LO)$  phonon from GaN are also reported in **Table 7.2**. Results obtained using visible Raman scattering are different for the  $A_1(LO)$  and  $E_2^2$  phonons. Since the  $A_1(LO)$  shifts at a rate of  $\sim 2/3$  that of the  $E_2^2$ ,

based on reported Raman stress factors for these two phonons,<sup>72</sup> the observed shifts from the visible measurements are attributable to average stress in the GaN layer.

Table 6.2 Peak positions from micro-Raman spectroscopy before and after diamond growth. Before and after comparisons are from spatially similar sample locations. Variation obtained by measuring at different positions on the samples range from 0.1 to 0.3  $\text{cm}^{-1}$  for visible and UV measurements, respectively. The measured reference values for GaN phonon energies are  $570.0 \pm 0.1 \text{ cm}^{-1}$  for  $E_2^2$  and  $737.6 \pm 0.1 \text{ cm}^{-1}$  for  $A_1(LO)$ . For the AlN reference, the measured value is  $656.7 \pm 0.1 \text{ cm}^{-1}$  for  $E_2^2$ .

Parameters		Before diamond growth		After diamond growth	
		Peak position ( $\text{cm}^{-1}$ )	Relative shift ( $\text{cm}^{-1}$ )	Peak position ( $\text{cm}^{-1}$ )	Relative shift ( $\text{cm}^{-1}$ )
Visible Raman Spectroscopy	GaN $E_2^2$ (FWHM) ( $\text{cm}^{-1}$ )	$566.8 \pm 0.1$ ( $3 \pm 0.1$ )	$-3.2 \pm 0.1$	$566.6 \pm 0.1$ ( $3.4 \pm 0.5$ )	$-3.4 \pm 0.1$
	GaN $A_1(LO)$ (FWHM)	$733.3 \pm 0.1$ ( $6.4 \pm 1$ )	$-2.3 \pm 0.2$	$733.6 \pm 0.1$ ( $5.9 \pm 1$ )	$-1.9 \pm 0.1$
	AlN $E_2^2$ (FWHM)	$650.6 \pm 0.1$ ( $4.1 \pm 0.2$ )	$-6.0 \pm 0.1$	$650.8 \pm 0.1$ ( $3.2 \pm 0.3$ )	$-5.9 \pm 0.1$
	Diamond O( $\Gamma$ ) (FWHM)			$1333.2 \pm 0.1$ ( $6.4 \pm 0.1$ )	
UV Raman Spectroscopy	GaN $E_2^2$ (FWHM)	$566.8 \pm 0.1$ ( $4.3 \pm 0.1$ )	$-3.3 \pm 0.1$	$566.6 \pm 0.1$ ( $4.1 \pm 0.2$ )	$-3.4 \pm 0.1$
	GaN $A_1(LO)$ (FWHM)	$736.1 \pm 0.1$ ( $14.0 \pm 1$ )	$-1.4 \pm 0.2$	$736.4 \pm 0.1$ ( $13.3 \pm 3$ )	$-1.1 \pm 0.2$
	Diamond O( $\Gamma$ ) (FWHM)			$1333.2 \pm 0.1$ ( $7.3 \pm 0.1$ )	
	2 <sup>nd</sup> -order quasi- $E_1(LO)$	$1474.8 \pm 0.1$ ( $20.4 \pm 0.2$ )		$1475.1 \pm 0.1$ ( $20.3 \pm 0.1$ )	

In the UV measurements, however, the shift observed for the  $A_1(LO)$  phonon is smaller than what is expected from stress. This is tentatively attributed to photo-induced free-carrier concentration estimated to be  $n = (0.76 \pm 0.31) \times 10^{17} \text{ cm}^{-3}$  based on the empirical formula of Hiroshi et al.<sup>109</sup>

## 6.5 Interface analysis by STEM

Although the impact of CVD diamond integration on the structural and material properties of the AlGaN layers have been investigated through HRXRD and micro-Raman measurements, it is also important to examine the interface properties. To do so, cross-sectional STEM measurements were taken before and after diamond growth. The bright-field STEM images in **Figure 6.7(a) and (b)** both show an abrupt interface between the *in-situ* SiN<sub>x</sub> and AlGaN barrier layer. A continuous SiN<sub>x</sub> layer is critical for effective passivation of state-of-the-art AlGaN/GaN HEMTs.<sup>55,110</sup> However, minimizing the thickness of the SiN<sub>x</sub> layer is highly beneficial for heat transport from the 2DEG channel to the diamond.<sup>20,84</sup> Through this research, a 45 nm *in-situ* SiN<sub>x</sub> passivation-adhesion layer as the ideal compromise for these diamond growth conditions.<sup>111</sup> In particular, the selective thermochemical etching/degradation of the SiN<sub>x</sub>, shown in **Figure 6.7(b)**, must be considered. The initial 45 nm SiN<sub>x</sub> layer, while thinned to 20 nm in some regions, nonetheless remains continuous across the entirety of the AlGaN barrier layer. The AlGaN barrier layer thickness is seen to be unaffected by the diamond deposition as indicated by the consistent 20 nm thickness after diamond growth, and in agreement with XRR. Additionally, **Figure 6.7(b)** shows a dark contrast region above the SiN<sub>x</sub> layer that is due to nanometer scale material from the filament depositing at the initial stage of diamond deposition. This filament material is known to occur in HFCVD diamond<sup>112</sup>.

Carbon diffusion during the CVD diamond deposition process into the GaN buffer layer can be detrimental to device performance and may result in severe current collapse.<sup>113</sup>

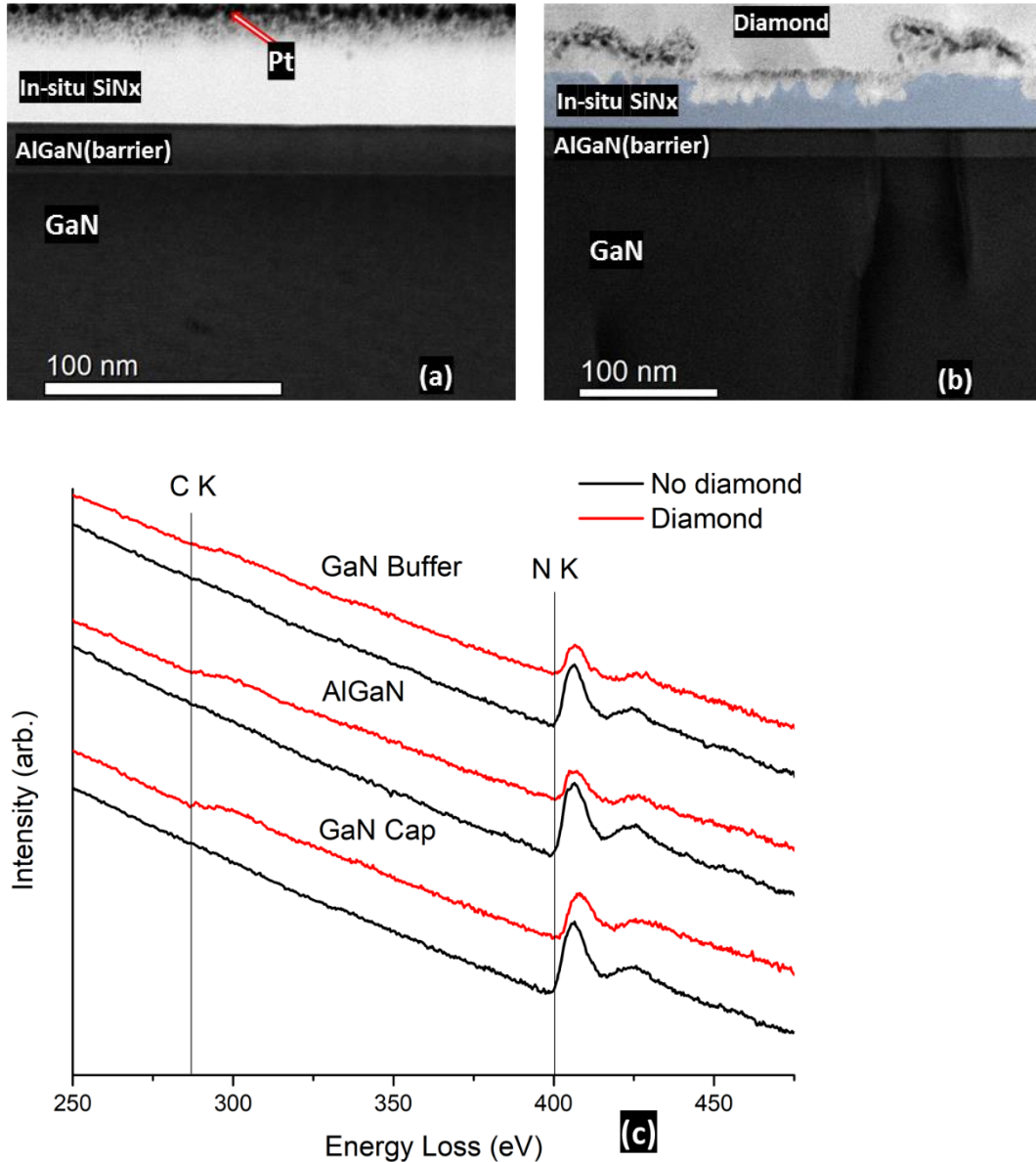


Figure 6.7 Bright-field STEM images showing the Al(Ga)N/SiN<sub>x</sub> layer interfacial region (a) before and (b) after diamond growth. EELS data comparison (c) point scan with extended collection time

To evaluate carbon diffusion, TEM-EELS analysis was chosen because of its higher sensitivity to light elements compared to EDS<sup>14</sup> and also to avoid issues with secondary x-ray fluorescence from the nearby diamond which could give inaccurate results. Typical area mapping does not indicate carbon diffusion into the AlGaN/GaN layers. However, point scans with extended collection times shown in **Figure 6.7(c)** were able to detect trace

amounts of carbon, likely near the detectable limit (generally accepted to be ~0.1 % for EELS), in the GaN cap and AlGaN barrier while the GaN buffer layer exhibits no carbon signal, which is identical to the point scan taken from the wafer before diamond deposition.

## 6.6 Thermal Characterization by TDTR

Determination of the diamond thermal conductivity and the diamond/GaN TBR was carried out using TDTR. TDTR is an optical pump-probe method that utilizes an ultrafast laser with a sub-micron pulse width. Polarizing optics are used to separate the pulses into separate pump and probe paths. The pump beam then periodically heats the sample, while the probe beam provides information about the transient temperature decay at the surface of the sample. More details of the system used in this study can be found in the literature.<sup>101</sup> Due to the complexity of the diamond/HEMT structure in this work, the SiN<sub>x</sub>, GaN cap, AlGaN, and AlN between the CVD diamond and the GaN buffer layer were treated as a single interface. This allowed for the determination of an effective TBR that includes the aforementioned layers. Additionally, the relatively large surface roughness of the diamond, 92.4 nm RMS, complicates this measurement and contributes to the uncertainty. Previous work has shown TDTR measurements with a diamond surface roughness RMS up to 100 nm<sup>115</sup>, however, this is not typical for the majority of reported TDTR studies. By simultaneously fitting for the diamond thickness, diamond thermal conductivity, and diamond/GaN TBR we were able to determine the unknown parameters as well as check the diamond thickness as reported in the growth. The parameters used in the model are given in **Table 6.3**.

It has been shown that for thin diamond films the thermal conductivity is anisotropic due to the columnar polycrystalline growth.<sup>116</sup> Here, the simplifying

assumption of an effective isotropic thermal conductivity is applied. The diamond thickness determined from the fit was  $1.46 \pm_{0.10}^{0.09} \mu\text{m}$ , which is in reasonable agreement with what is measured directly by STEM  $1.25 \pm_{0.12}^{0.12} \mu\text{m}$ . For this thickness the effective isotropic thermal conductivity of the diamond was  $176 \pm_{35}^{40} \text{W/m-K}$ , and the effective TBR of the diamond/GaN interface (including the  $\text{SiN}_x$  and additional layers) was  $52.8 \pm_{3.2}^{5.1} \text{m}^2\text{K/GW}$ . It is important to note the significant difference between bulk diamond thermal conductivity and that of thin films. The thermal conductivity of CVD diamond has been shown to be highly dependent on the thickness of the material due to the nature of the columnar growth structure<sup>98</sup>. For instance, Yates *et al.* have reported measurements of diamond films ranging from  $5 \mu\text{m}$  to  $13.9 \mu\text{m}$  in which the thermal conductivity was shown to vary from  $712 \text{W/m-K}$  to  $1362 \text{W/m-K}$  for the respective film thicknesses. Additionally, their work demonstrated the ability to measure high quality bulk diamond with a thickness  $> 300 \mu\text{m}$ . In the same work, the impact of boron doping demonstrated thermal conductivity values in a bulk sample of only  $650 \text{W/m-K}$ , while samples with no additional doping were measured to be up to  $2200 \text{W/m-K}$ <sup>117</sup>. Further work has demonstrated the significantly reduced and non-homogenous thermal conductivity of  $1 \mu\text{m}$  diamond films by using TDTR to spatially map a suspended membrane. Additionally, a thorough analysis of the implications of using TDTR to measure the thermal conductivity of both diamond films and bulk samples has been undertaken by Bougher *et al.*, where they demonstrated the exceptional capabilities of TDTR as a method to measure the thermal conductivity of such materials<sup>118</sup>.

Measurement uncertainties were determined using a Monte Carlo method with the 5<sup>th</sup> and 95<sup>th</sup> percentiles used as the upper and lower bounds. This method has been

previously described in detail<sup>101</sup> and consists of assigning each value in the thermal model a relative uncertainty. For each parameter that is not included as a fit parameter a random distribution of possible values for the non-fit parameters is created based on the assigned uncertainty.

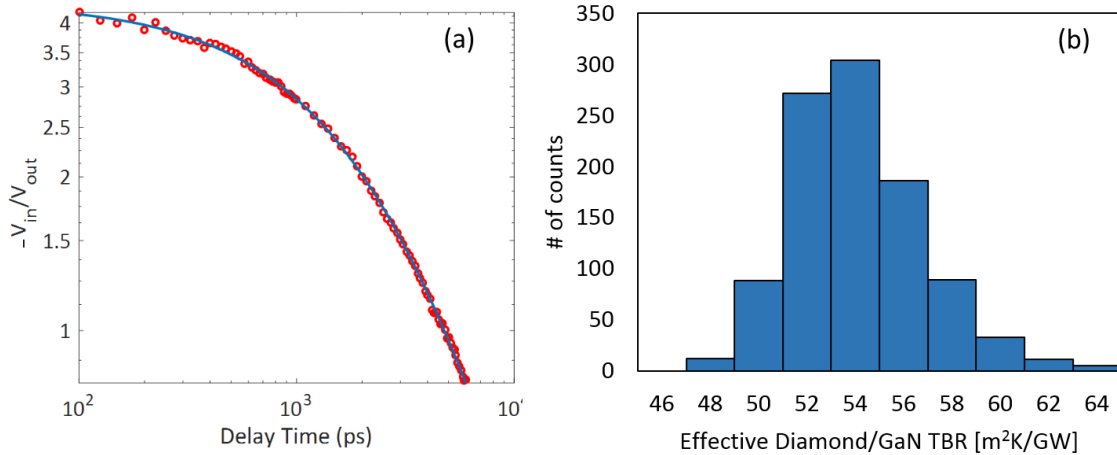


Figure 6.8 (a) Experimental TDTR data (red circles) and the analytical fit solution (blue line). The experimental data is fit using a Levenberg-Marquardt algorithm that considers multi-variable and non-linear data fitting. This routine is used to compare the experimentally measured data to a solution for cylindrical radial heat transport through multiple thin films and has been extensively documented in literature<sup>119</sup> (b) Normal distribution of the effective diamond/GaN TBR as determined from the Monte Carlo uncertainty. Each fit parameter was estimated by considering the 50<sup>th</sup> percentile as the measured value, with the 5<sup>th</sup> and 95<sup>th</sup> percentile taken as the lower and upper bounds of uncertainty. The experimental data were subjected to 1000 iterations of the Monte Carlo method in order to obtain the normal distributions.

The thermal model is then fit to the experimental data multiple times with values for each of the non-fit parameters being randomly varied according to the previously assigned uncertainty. This is performed until convergence on the fit parameters is reached and allows for a normal distribution for each of the fit parameters to be created. In this work convergence was obtained after 500 iterations, however 1000 iterations were performed in order to create the normal distributions for each fit parameter. **Figure 6.8** shows the TDTR data fit of the experimental data and the normal distribution of the

effective diamond/GaN TBR. The thermal conductivity of the polycrystalline diamond and TBR values for the diamond/AlGaIn/GaN HEMT interface are in the same range (for  $1000 \pm 100$  nm thick diamond, thermal conductivity 150 to 450 W/m-K, and TBR 50 to 95  $\text{m}^2\text{K}/\text{GW}$ ) as reported for a similar structure by Zhou *et al.*<sup>98</sup>

The non-fit values used in the thermal model, shown in **Table 6.3**, were found in literature and have been consistent with what has been used in previous TDTR models.<sup>116</sup> The thermal conductivity of the AlGaIn was taken from data reported from Lui *et al.*<sup>120</sup> In their work, they show no significant variation in thermal conductivity for AlGaIn compositions consisting of Al varied between 0.2 and 0.8. This is relevant since the present assumption is the two AlGaIn layers are considered as a single layer in the model. The AlN thermal properties used in the model were taken from Zhao *et al.*<sup>121</sup>, where they measured thin AlN films ranging from 100 nm to 1050 nm. The value of 1.5 W/m-K is substantially lower than the extrapolated value of 320 W/m-K that was first inferred by Slack *et al.*<sup>122</sup> This very large value considered single crystal, defect free AlN. It has, however, been shown that AlN has a significant size dependence on thermal conductivity.<sup>123</sup> In addition to a size dependence, the quality of AlN films which depends on deposition process, grain size, and impurity concentrations has been shown to have measured variations between 0.4 W/m-K to 270 W/m-K.<sup>124,125</sup> In all cases, the thermal conductivity of the AlN in the present model is of little consequence to the fit values of the CVD diamond parameters because the AlN layer is buried below both the GaN and the AlGaIn. The use of a pulsed thermal technique such as TDTR will be limited due to the penetration depth of the thermal wave.<sup>126</sup> In the case of the experimental stack there is no sensitivity to the AlN thermal conductivity regardless if it is 1.5 W/m-K or 300 W/m-K. TDTR sensitivity has been well

documented,<sup>118</sup> as it considers a fractional change in an independent parameter to the overall change in the reflectance signal. It is clear from **Figure 6.9** that changing the assumed AlN thermal conductivity from 1.5 W/m-K to 300 W/m-K has no impact on the measurement, while the other parameters of interest remain sensitive to the measurement.

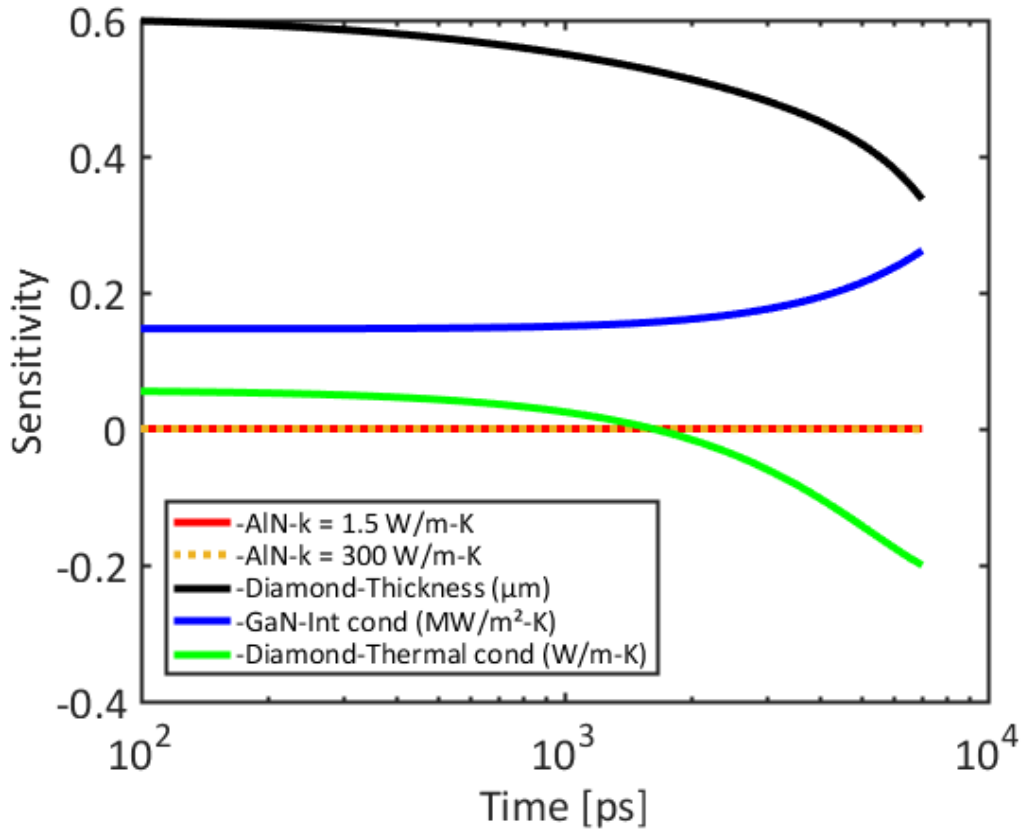


Figure 6.9 Sensitivity analysis of the TDTR model used in this work. It is clear that the diamond thickness is the most sensitive parameter and the fit value was found to be in good agreement with the STEM measurements. It is important to point out the lack of sensitivity to the thermal conductivity of the AlN layer. The solid red line indicates an AlN thermal conductivity of 1.5 W/m-K as was used in the model, while the dashed orange line is indicative of using an AlN thermal conductivity of 300 W/m-K. In both scenarios we had no sensitivity to this parameter, and it did not impact the other fit parameters of the model.

Table 6.3 Parameters used in TDTR model. The TBR between the Al/diamond and the effective TBR between the CVD diamond/GaN are also fit parameters. All other TBRs were held constant at 10 m<sup>2</sup>K/GW.

Material	Thickness (nm)	Thermal Conductivity [W/m-K]	Vol. Heat Capacity [J/m <sup>3</sup> K]
Al	96 ± 3%	150 ± 5%	2.43E6 ± 2%
CVD Diamond	fit	fit	1.73E6 ± 5%
GaN	870 ± 10%	130 ± 10%	2.64E6 ± 5%
AlGa <sub>N</sub>	800 ± 10%	25 ± 10%	3.09E6 ± 5%
AlN	426 ± 10%	1.5 ± 10%	2.41E6 ± 5%
Si	Semi-inf	148 ± 5%	1.66E6 ± 5%

## 6.7 Conclusions

The effects of diamond growth on AlGa<sub>N</sub>/Ga<sub>N</sub> HEMTs when protected by a 46 nm thick *in-situ* SiN<sub>x</sub> passivation/adhesion layer have been investigated. The SiN<sub>x</sub> was grown using MOCVD in the same chamber and immediately following the III-Nitride growth process. The diamond was grown in a HFCVD reactor.

Structural integrity and materials properties of the AlGa<sub>N</sub>/Ga<sub>N</sub> HEMT were evaluated using HRXRD, specifically RSM, and micro-Raman measurements. HRXRD shows a slight increase in the biaxial stress in the Ga<sub>N</sub> layer when comparing before (0.58±0.05 GPa) to after (0.73±0.07 GPa) diamond growth. The RSMs show that the AlGa<sub>N</sub> barrier layer is unaffected by the diamond deposition. Consistency in the Ga<sub>N</sub>  $E_2^2$  shifts for both visible and UV Raman signifies that the Ga<sub>N</sub> crystal quality is intact and uniform across the thickness before and after the diamond growth.

Abrupt *in-situ* SiN<sub>x</sub>/AlGa<sub>N</sub>/Ga<sub>N</sub> interface without any degradation is observed

before and post diamond growth. Selective degradation to the *in-situ* SiN<sub>x</sub> layer at the SiN<sub>x</sub>/diamond interface is confirmed using STEM cross-sectional analysis. Even with some selective degradation to the *in-situ* SiN<sub>x</sub> layer, there is still > 20 nm intact SiN<sub>x</sub> to protect the underlying III-Nitride layers. Although the degree of degradation to the interface layers depends on the seeding density and diamond growth conditions, in these experiments, for 2% CH<sub>4</sub> and with this seeding method, a 46 nm thick SiN<sub>x</sub> passivation/adhesion layer is sufficient to fully protect the AlGaIn/GaN HEMT structure during HFCVD diamond growth.

Finally, the thermal conductivity of polycrystalline diamond (176 + 40/-35 W/m-K) and the diamond-GaN interface TBR (52.8 + 5.1/-3.2 m<sup>2</sup>K/GW) values reported here are consistent with those reported for a similar material stack.<sup>93</sup>

## 7 OPTIMIZATION OF THERMAL BOUNDARY RESISTANCE OF DIAMOND- $\text{AlGaN}/\text{GaN}$ INTERFACE BY *IN-SITU* $\text{SiN}_x$ THICKNESS REDUCTION AND CVD DIAMOND GROWTH OPTIMIZATION

### 7.1 Introductions

$TBR_{eff}$  is the effect of acoustic mismatch between materials which includes the dielectric interlayer used for diamond growth seeding, and the defective transition region at the dielectric layer/diamond interface, also referred to as the nucleation layer, or nano crystalline diamond (NCD) layer.<sup>84</sup> As discussed in Chapter 6, the thinner the dielectric adhesion layer the better the effective heat spreading from a self-heating  $\text{AlGaN}/\text{GaN}$  HEMT using a diamond heat spreader.

However, thinning the dielectric adhesion layer comes with some serious challenges. In particular, etching and decomposition of the underlying III-Nitride layers during harsh diamond growth condition is of substantial concern<sup>98</sup> if the protective dielectric adhesion layer is not sufficiently thick. As discussed in Chapter 6, higher seeding density results in quicker coalesce of diamond and reduced  $\text{SiN}_x$  etching, thereby effectively protecting the  $\text{AlGaN}$  barrier layer. As studied separately by my colleague which would be report elsewhere found that increasing the  $\text{CH}_4$  concentration during CVD diamond growth significantly increases the diamond growth rate, thereby ensuring quicker coalesce and lateral coverage. The high growth rate also provides for a smoother diamond surface for an equivalent coalesced diamond thickness. Having a smoother diamond surface would benefit the determination of thermal properties (TBR, thermal conductivity) of diamond-on-GaN by the time domain thermoreflectance (TDTR) technique.

Although successful integration of CVD diamond into AlGaIn/GaN HEMTs has been achieved without any degradation and reasonable TBR values, there is still room for improvement to further reduce TBR to realize the most efficient thermal pathway to dissipate heat. In this chapter further optimization of TBR is achieved by reducing the thickness of the dielectric adhesion layer while simultaneously increasing the CH<sub>4</sub> content during CVD diamond growth. Surface, structural and interfacial properties were determined using atomic force microscopy (AFM), x-ray reflectivity (XRR), high resolution x-ray diffraction, scanning electron microscopy (SEM) and TDTR.

## 7.2 Experimental Details

The standard baseline AlGaIn/GaN HEMT structure was grown on a low resistivity (100 mm, 40 Ω-cm) Si (111) substrate using the Texas State MOCVD reactor<sup>127</sup>, followed by *in-situ* SiN<sub>x</sub> growth at 1020 °C and a chamber pressure of 100 Torr. Two different *in-situ* SiN<sub>x</sub> SiH<sub>4</sub>/NH<sub>3</sub> ratios are evaluated: 22.2E-6 for sample X25 and 88.9E-6 for sample X100. These conditions are identical to samples C1 and D1 researched in Chapter 4. Details of the *in-situ* SiN<sub>x</sub> passivated AlGaIn/GaN HEMT growth process have been discussed in Chapters 4.

For the diamond CVD process, a photoresist based seeding technique is used, as reported by Ahmed *et al.*<sup>100</sup> A power of 6 kW was driven through an array of 9 tungsten wires of 0.01" diameter, which resulted in a 2200 °C wire filament temperature. The rotating substrate was positioned 6 mm from the tungsten wire array to produce a substrate temperature of 720-750 °C and uniform diamond growth rate. Growth was carried out for 7 h using 60 sccm of methane and 3 sccm of oxygen with 2,000 sccm of hydrogen (3% CH<sub>4</sub> in H<sub>2</sub>) into HFCVD chamber while maintaining a pressure of 20.8 Torr. As discussed

below, this process results in 315 to 353 nm  $\pm$  50 nm thick fully coalesced diamond and uniform coverage across the wafer.

X-ray reflectometry (XRR) of the *in-situ* SiN<sub>x</sub> was performed to determine the initial thickness and density of the MOCVD grown SiN<sub>x</sub> dielectric adhesion layer. HRXRD RSM was performed around both the GaN asymmetric (10-14) and symmetric (0002) planes to determine the stress and composition of the constituent layers before and after diamond deposition. Tapping mode AFM measurements of the *in-situ* SiN<sub>x</sub> surface, before diamond growth, and of the diamond surface after growth were taken to evaluate surface roughness and diamond grain size.

Cross-sectional samples were fabricated using the standard focused ion beam (FIB) technique using a FEI Helios Nanolab 400 DualBeam system by first depositing a protective Pt layer and milling using a 30 kV accelerating voltage. A final polishing step was then performed with an accelerating voltage of 2 kV to remove surface damage.

Finally, time domain thermoreflectance (TDTR) measurements<sup>101</sup> were performed to evaluate the diamond/GaN thermal boundary resistance (TBR) and the thermal conductivity of the polycrystalline diamond. To perform the TDTR, an 87  $\pm$ 3 nm layer of Al was deposited by e-beam evaporation at room temperature.

### **7.3 Surface, structural and interface characterization of Diamond-on-AlGaIn/GaN HEMT**

The top surface layers were characterized using grazing incident XRR. SiN<sub>x</sub> thickness was estimated by fitting the specular reflection spectrum using the Globalfit

software, as discussed in Chapter 2. The thickness and the SiN<sub>x</sub> density of the passivated sample wafers are tabulated in **Table 7.1**.

Table 7.1 Thickness of the top layers of *in-situ* SiN<sub>x</sub> passivated AlGaIn/GaN HEMT wafers determined by XRR.

	<b>X25</b>	<b>X100</b>
SiN <sub>x</sub> (nm)	35.9	36.0
GaN (cap) (nm)	0.7	1.9
AlGaIn barrier (nm)	20.2	20.0

To evaluate the surface morphology of the *in-situ* SiN<sub>x</sub> passivated HEMT, tapping mode AFM was performed. Smooth surface morphology of the SiN<sub>x</sub> is observed without any degradation to the underlying III-Nitride layers as shown in **Figure 7.1**. From the 2D AFM 5 μm x 5 μm scans, the RMS roughness for both samples, X25 and X100, is 0.39 nm. **Figure 7.2** shows the 2D AFM images of the CVD diamond surface for (a) 10 μm x 10 μm, and (b) 5 μm x 5 μm diamond surface of the sample X25. Fully coalesced diamond is observed with an RMS roughness of ~38 nm for 10 μm x 10 μm scan while for a 5 μm by 5 μm the roughness is found to be ~37 nm with grain-size of ~375 ± 120 nm and ~340 ± 110 nm calculated using the linear intercept method. The values are within their uncertainty limit, which proves consistency of grain size and roughness over a large area.

To evaluate the effect of diamond growth on the *in-situ* SiN<sub>x</sub> passivated AlGaIn/GaN HEMT structure, HRXRD measurements were used to determine whether the underlying III-Nitride layers have been protected during 3 h of diamond growth in the HFCVD environment. HRXRD RSM scans around the asymmetric (10-14) III-Nitride planes, shown in **Figure 7.3** and **7.4**, indicate no change in the patterns before and after diamond growth which confirms the III-Nitride layers are not degraded during diamond

CVD. Specifically, distinct peaks for all the III-Nitride (GaN, AlN, TL1, and TL2) layers are present before and after diamond deposition. The barrier layer peak (indicated inside the ellipse) is invariant before and after diamond deposition. Thus, for both samples, X25 and X100, the AlGaN/GaN heterostructure is not degraded confirming that the *in-situ* SiN<sub>x</sub> dielectric adhesion layer has fully protected the III-Nitride

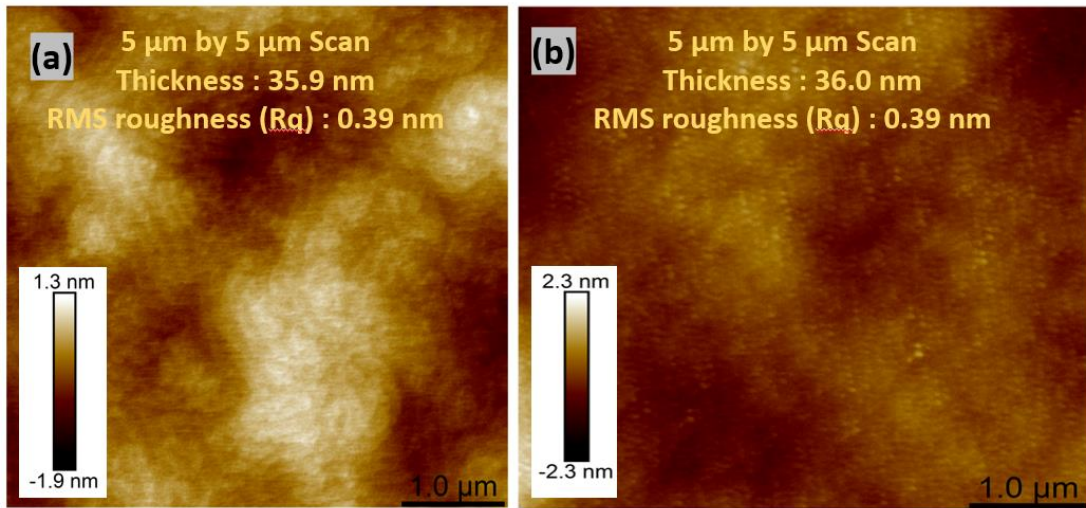


Figure 7.1 Tapping mode 2D AFM 5 μm x 5 μm images of the SiN<sub>x</sub> surface, (a) sample X25, and (b) sample X100.

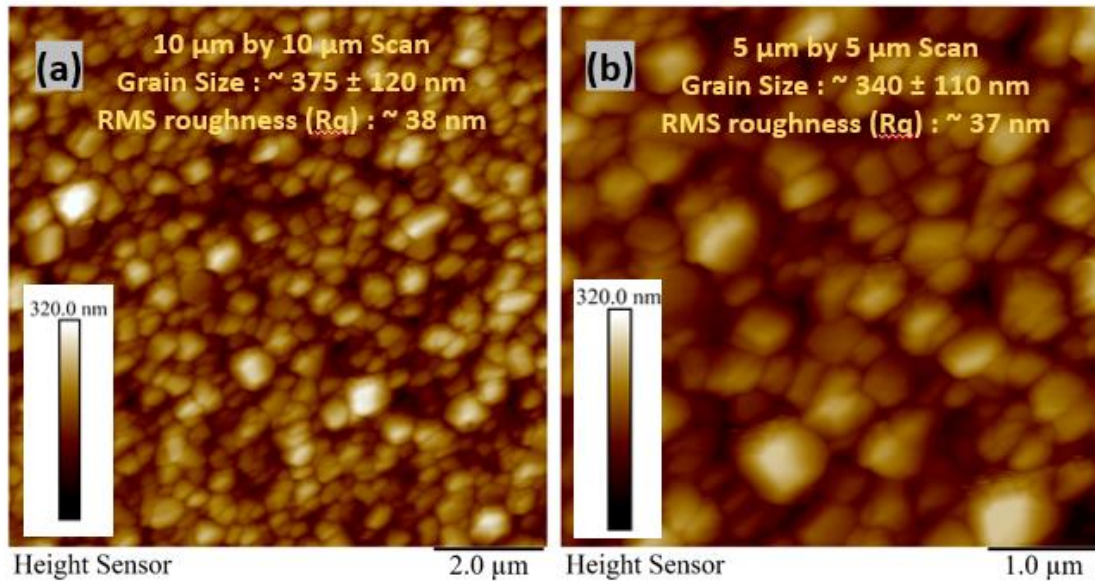


Figure 7.2 AFM images of the diamond surfaces of sample X25, (a) 10 μm x10 μm diamond, and (b) 5 μm x 5 μm diamond surface confirming fully coalesced diamond. surface.

While it is evident from **Figures 7.3** and **7.4** that the structure of the AlGaIn/GaN HEMT for both experimental samples are intact, to further characterize the interface SEM cross-sections were analyzed. **Figure 7.5** shows the cross-sectional SEM images of the diamond-on-AlGaIn/GaN HEMT interfaces with the two *in-situ* SiN<sub>x</sub> dielectric adhesion layers. An abrupt AlGaIn/GaN interface is visible for both samples. The SiN<sub>x</sub> dielectric layers are selectively etched, analogous to the experiments discussed in Chapter 6. The SiN<sub>x</sub> in the X25 sample is somewhat more etched compared to the X100 sample. This may be a result of the X100 SiN<sub>x</sub>, with  $x = [N]/[Si] = 1.13$ , being slightly more dense than the X25 SiN<sub>x</sub>, with  $x = 1.17$ , and, thereby, being better able to withstand the harsh diamond growth environment. Nevertheless, continuous SiN<sub>x</sub>-diamond interfaces are obtained for both samples ensuring that there is no discontinuity to the III-Nitride surface and

enabling a good thermal pathway for heat transfer from the AlGaIn/GaN HEMT to the HFCVD diamond.

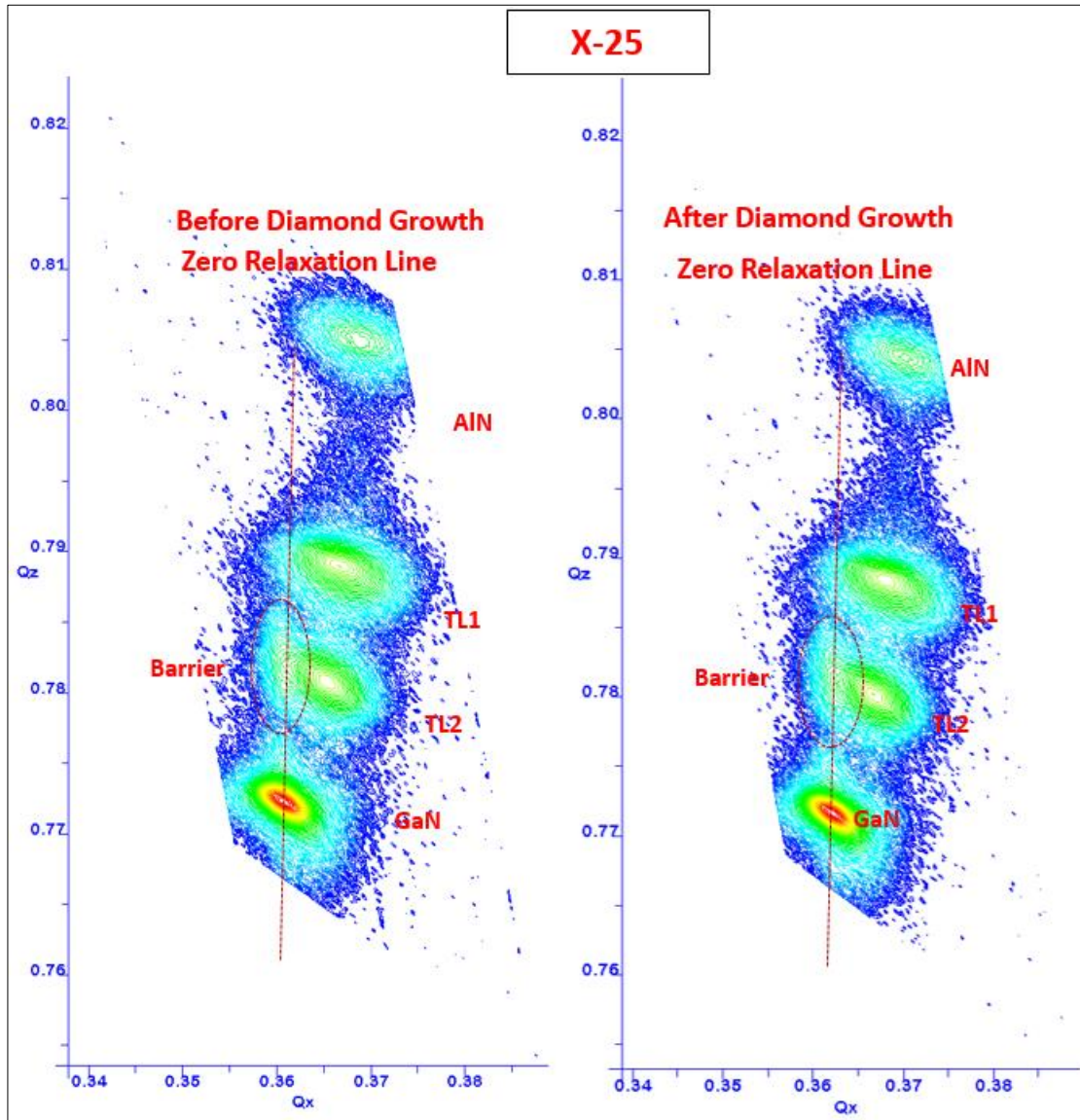


Figure 7.3 RSM contour plots of the X25 wafer collected around the asymmetric (10-14) planes before (left) and after (right) diamond deposition. The dotted line indicates the zero-relaxation line along the crystallographic  $a$ -axis.

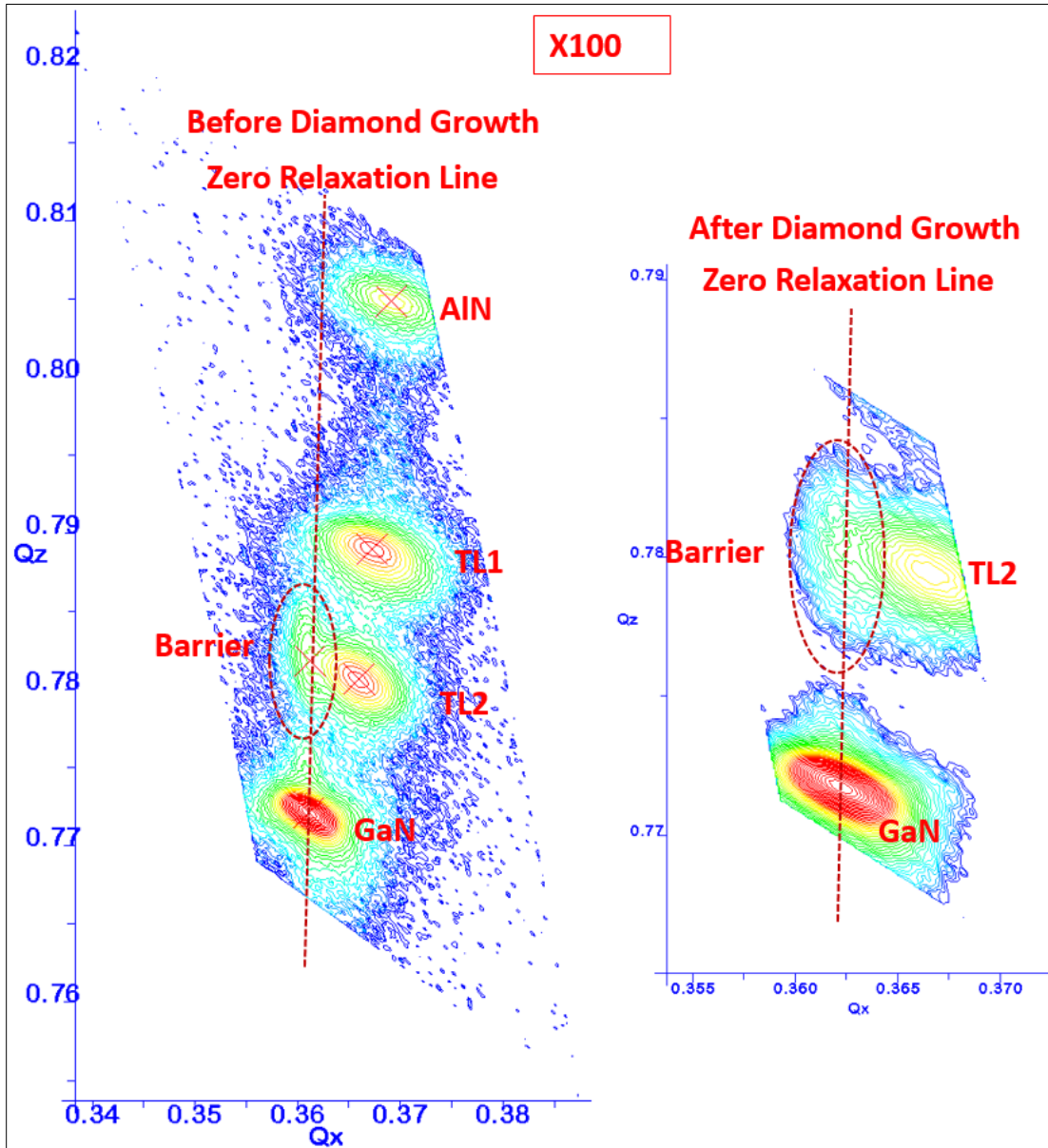


Figure 7.4 RSM contour plots of the X100 wafer collected around the asymmetric (10-14) planes before (left) and after (right) diamond deposition. The dotted line indicates the zero-relaxation line along the crystallographic  $a$ -axis.

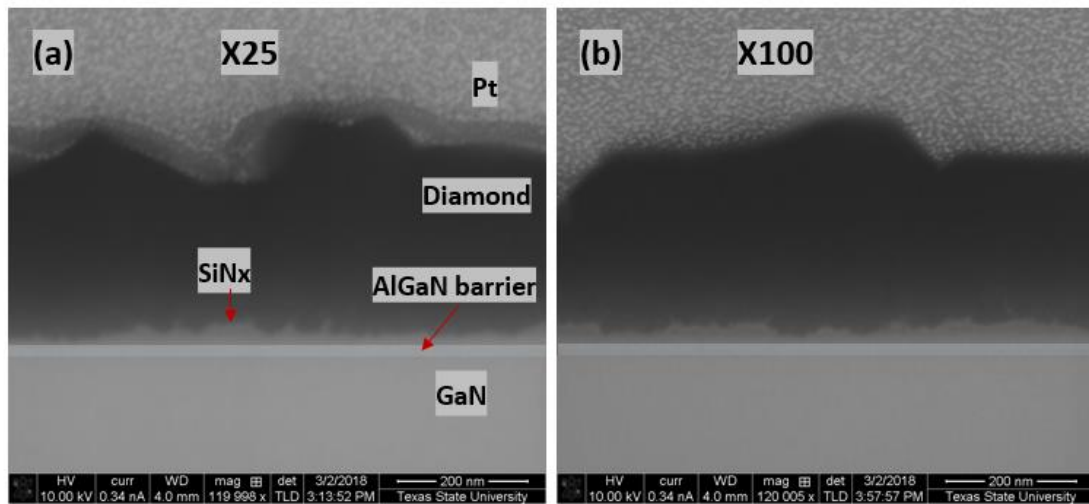


Figure 7.5 Cross-sectional SEM of Diamond-on-AlGaIn/GaN HEMT with experimental *in-situ* SiN<sub>x</sub> dielectric adhesion layers, (a) X25 and (b) X100.

#### 7.4 Thermal Characterization by TDTR

The detail of the TDTR measurement technique and the model employed in the present study is described in Chapter 6 and can also be found elsewhere<sup>101,117,118,128</sup>. For simplicity, as with the previous study, the diamond/ HEMT structure (SiN<sub>x</sub>, GaN cap, AlGaIn barrier, and AlN spacer) between the CVD diamond and the GaN buffer layer are treated as a single interface. This allows for the determination of an effective TBR that includes the aforementioned layers. By simultaneously fitting for diamond thermal conductivity, the diamond thickness, and diamond/ GaN TBR, the unknown parameters may be determined. Furthermore, the diamond thickness may be compared to SEM cross-section measurements. The estimated data with their normal distribution from the fitted model is presented in **Figures 7.6** and **7.7**, along with a tabulated summary in **Table 7.2**.

As reported in Chapter 6, a thin CVD diamond film thermal conductivity is anisotropic in nature due to the columnar polycrystalline growth.<sup>116</sup> However, a simplifying assumption was made to include an effective isotropic thermal conductivity. For the X25 sample diamond thickness ( $336 \pm 42$  nm), the effective isotropic thermal conductivity of the diamond is  $36 \pm_{-9}^{+19}$  W/m-K, and the effective TBR of the diamond/GaN interface (including the SiN<sub>x</sub> + profile(AlN) + barrier (AlGaIn) + GaN cap layers) was  $32 \pm 3.6$  m<sup>2</sup>K/GW. For the X100 sample the effective isotropic diamond thermal conductivity is slightly higher, at  $43 \pm_{-8}^{+15}$  W/m-K, and the effective TBR is slightly lower, at  $31 \pm 2.5$  m<sup>2</sup>K/GW.

**Figures 7.6 and 7.7** show the TDTR data for X25 and X100, respectively, presenting (a) the normal distribution of the effective diamond/GaN TBR, and (b) the normal distribution of thermal conductivity. For sample X100, the diamond thickness is determined to be  $334 \pm 40$  nm, the effective isotropic thermal conductivity of diamond layer is  $43 \pm_{-8}^{+15}$  W/m-K and the effective TBR for GaN-diamond interface is  $31 \pm 2.5$  m<sup>2</sup>K/GW.

The TBR values for X25 are almost identical, even though the residual SiN<sub>x</sub> thickness is higher for X100. This could be because of the denser SiN<sub>x</sub> in X100 which may have higher thermal conductivity compared to X25.

For polycrystalline diamond of similar thickness ( $300 \pm 100$  nm), the thermal conductivity reported by Zhou *et al.*<sup>98</sup> ranged from 50 to 125 W/m-K, which is higher than the values in the present study. This may be due to inclusions of impurities (W, WC) during HFCVD diamond growth. However, the TBR's range is ~ twice what have been found for

X25 and X100. Nevertheless, the TBR values reported in the present study are the lowest measured for similar diamond-on-HEMT structures.

Table 7.2 Thermal properties of the GaN-diamond interface from TDTR measurement

	<b>X25</b>	<b>X100</b>
GaN/Diamond TBC [MW/m <sup>2</sup> -K]	31 ± 3.5	32 ± 2.6
GaN/Diamond TBR [m <sup>2</sup> -K/ GW]	32 ± 3.6	31 ± 2.5
Diamond/Al TBC [MW/m <sup>2</sup> -K]	105 ± 6	79 ± 2.7
Diamond thermal conductivity [W/m-K]	36 +19/-9	43 +15/-8
Diamond thickness (nm)	336 ± 42	334 ± 40

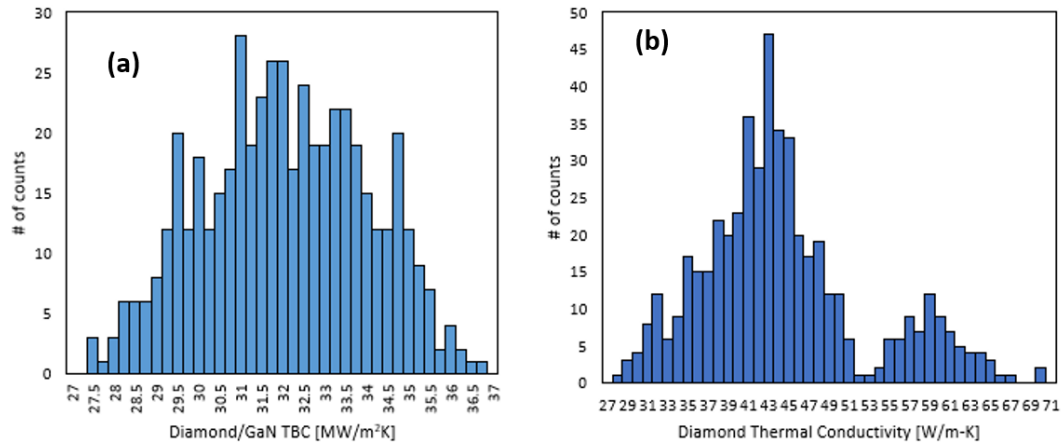


Figure 7.6 Normal distribution of the (a) effective diamond/GaN TBC, and (b) thermal conductivity of CVD diamond of sample X25 determined from the Monte Carlo uncertainty. Each fit parameter was estimated by considering the 50<sup>th</sup> percentile as the measured value, with the 5<sup>th</sup> and 95<sup>th</sup> percentile taken as the lower and upper bounds of uncertainty. The experimental data were subjected to 1000 iterations of the Monte Carlo method in order to obtain the normal distributions.

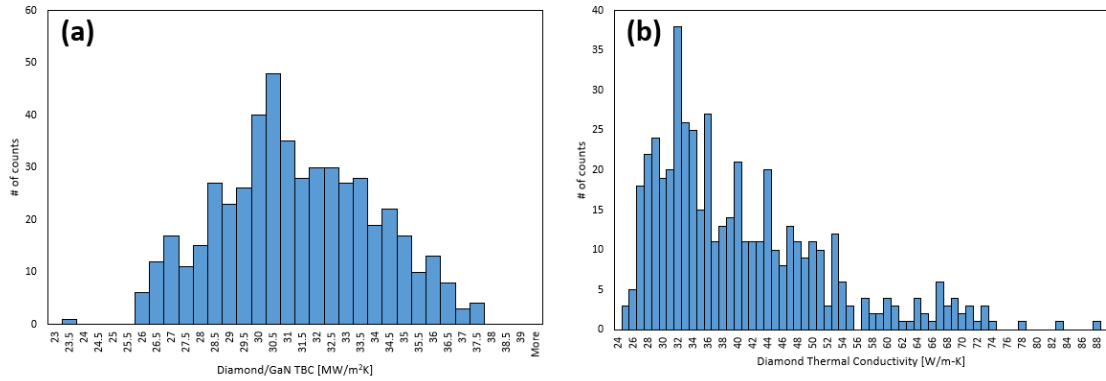


Figure 7.7 Normal distribution of the (a) effective diamond/GaN TBC, and (b) thermal conductivity of CVD diamond of sample X100 determined from the Monte Carlo uncertainty. Each fit parameter was estimated by considering the 50<sup>th</sup> percentile as the measured value, with the 5<sup>th</sup> and 95<sup>th</sup> percentile taken as the lower and upper bounds of uncertainty. The experimental data were subjected to 1000 iterations of the Monte Carlo method in order to obtain the normal distributions.

## 7.5 Conclusions

$TBR_{eff}$  across diamond-on-AlGaIn/GaN HEMT using an *in-situ* SiN<sub>x</sub> dielectric adhesion layer is achieved by increasing the diamond growth rate compared to the study discussed in Chapter 6. 3.0% CH<sub>4</sub> is used during diamond growth compared to the previously reported 2.0% CH<sub>4</sub> to ensure a higher lateral coverage rate, thereby reducing the diamond growth induced etching of the *in-situ* SiN<sub>x</sub>. 36 nm thick *in-situ* SiN<sub>x</sub> is found to be sufficient to fully protect the AlGaIn/GaN heterostructure during 3 h of diamond growth. The lowest reported  $TBR_{eff}$  ( $31 \pm 2.5 \text{ m}^2\text{K/GW}$ ) for diamond-on-AlGaIn is determined from time domain thermoreflectance (TDTR) measurement, while the thermal conductivity of the polycrystalline diamond is found to be  $43 +15/-8 \text{ W/m-K}$

## 8 CONCLUSIONS AND FUTURE WORKS

### 8.1 Conclusions

The MOCVD growth process of *in-situ* SiN<sub>x</sub> on AlGa<sub>0.3</sub>N/GaN HEMTs is optimized at typical III-Nitride growth conditions without any degradation to the underlying AlGa<sub>0.3</sub>N/GaN heterostructure. The *in-situ* SiN<sub>x</sub> passivated AlGa<sub>0.3</sub>N/GaN HEMT is evaluated to study the effect of constituent gas chemistry on the AlGa<sub>0.3</sub>N/GaN HEMT's morphology, structural and electrical properties. Successful integration of HFCVD diamond on the AlGa<sub>0.3</sub>N/GaN HEMT is realized using MOCVD grown *in-situ* SiN<sub>x</sub> as a dielectric adhesion layer to facilitate diamond seeding and to act as a barrier layer to protect the underlying III-Nitride layers from the harsh diamond growth environment. Structural and interface properties of diamond-on-AlGa<sub>0.3</sub>N/GaN HEMT is evaluated to study the effect of diamond growth on the AlGa<sub>0.3</sub>N/GaN heterostructure. Thermal properties of the diamond-on-AlGa<sub>0.3</sub>N HEMT is determined to ascertain the thermal performance. The key findings learned from this dissertation project include:

- i. SiH<sub>4</sub> induced selective etching of the underlying III-Nitride layers is prevalent with lower SiH<sub>4</sub> and lower NH<sub>3</sub> gas ratios.
- ii. The selective etching of III-Nitride material is a result of SiH<sub>4</sub> induced etching of the Al(Ga)N around the screw and mixed dislocation cores, and simultaneous selective SiH<sub>4</sub> etching of the Al(Ga)N around fractal-like SiN<sub>x</sub> masking during the initial stages of growth before SiN<sub>x</sub> coalescence.
- iii. With increased SiH<sub>4</sub> flow and, thus, increased SiN<sub>x</sub> growth rate, faster surface coverage is achieved, and III-Nitride etching is reduced or mitigated.

- iv. Suppression of strain relaxation in the barrier layer has been observed for passivated samples, which provides increased piezoelectric polarization in the barrier layer.
- v. Enhanced electrical properties are attributed to the simultaneous effects of SiN<sub>x</sub> induced suppression of strain relaxation in the barrier layer, increased GaN buffer stress and surface state filling by optimizing the  $x = [\text{Si}]/[\text{N}]$  stoichiometry.
- vi. The combination of (a) low  $x$  (Si-rich SiN<sub>x</sub>) contributing to low interface alloy scattering and a more abrupt heterointerface, (b) minimal barrier layer relaxation, and (c) lower effective mass of the carriers in the channel due to the higher strain in the GaN material results in an optimized *in-situ* SiN<sub>x</sub> passivation process. The resulting 2DEG has the lowest sheet resistance (276 Ω-sq) representing a substantial reduction compared to the unpassivated, or PECVD SiN<sub>x</sub> passivated, baseline reference structure.
- vii. A 46 nm thick *in-situ* SiN<sub>x</sub> passivation/adhesion layer is sufficient to protect the underlying III-Nitride layers while growing 7 hours of HFCVD diamond with 2% CH<sub>4</sub>.
- viii. Minimal change in residual stress state is observed before and after diamond growth on GaN.
- ix. Smooth, abrupt *in-situ* SiN<sub>x</sub>/AlGaN interface is observed before and after diamond growth via STEM, and from EELS analysis it is found that there is no detectable diffusion of C into the AlGaN/GaN heterostructure.
- x. Selective degradation of the *in-situ* SiN<sub>x</sub> dielectric layer is prevalent but is reduced with an increased CVD diamond lateral growth rate.

## 8.2 Publications

Publications stemming from this dissertation project include,

1. Anwar Siddique, Raju Ahmed, Jonathan Anderson, and Edwin L. Piner, “Effect of Reactant Gas Stoichiometry of In-Situ SiN<sub>x</sub> Passivation on Structural Properties of MOCVD AlGa<sub>N</sub>/Ga<sub>N</sub> HEMTs” *J. Cryst. Growth* 2019, 517 (March), 28–34.  
<https://doi.org/10.1016/j.jcrysgro.2019.03.020>
2. Anwar Siddique, Raju Ahmed, Jonathan Anderson, Mohammed Nazari, Luke Yates, Samuel Graham, Mark Holtz, and Edwin Piner, “Hot Filament Chemical Vapor Deposition of Diamond on GaN Using In-situ SiN<sub>x</sub> Grown by MOCVD as Dielectric Adhesion Layer” *ACS Appl. Electron. Mater* 2019.  
<https://doi.org/10.1021/acsaelm.9b00131>. (accepted manuscript)
3. Anwar Siddique, Raju Ahmed, Jonathan Anderson, Mohammed Nazari, Mark Holtz, and Edwin Piner, “Chemical Vapor Deposition of Diamond on GaN Using MOCVD Grown In-Situ SiN<sub>x</sub> as Dielectric Adhesion Layer” *MRS-2018 New Diamond and Nano Carbons Conference*
4. Anwar Siddique, Raju Ahmed, Jonathan Anderson, and Edwin Piner “AlGa<sub>N</sub>/Ga<sub>N</sub> HEMT 2DEG Impact by in-situ SiN<sub>x</sub> Passivating Layer Stoichiometry Grown by MOCVD” *ICNS 2019* (accepted abstract)

## 8.3 Future Works

This dissertation research has been an effort to prove the feasibility of integrating AlGa<sub>N</sub>/Ga<sub>N</sub> HEMT and CVD diamond using *in-situ* SiN<sub>x</sub> as a dielectric adhesion layer to

dissipate heat from the 2DEG self-heating source. Successful optimization of *in-situ* SiN<sub>x</sub> growth by MOCVD at typical III-Nitride growth conditions is realized. Using optimized *in-situ* SiN<sub>x</sub> as a dielectric adhesion layer, CVD diamond is successfully optimized and integrated into the AlGa<sub>x</sub>N/GaN HEMT. Still, there are plenty of exciting research areas needing to be investigated, especially to achieve a functioning AlGa<sub>x</sub>N/GaN HEMT with the highest power density possible. Here are some of the research ideas for future works.

### **8.3.1 Device fabrication, electrical and thermal properties comparison of HEMT with different TL scheme**

Optimized step graded transition layers were grown and structural properties (Al % and stress profile) determined (See Chapter 2). The addition of an extra step graded transition layer (SG0) reduces residual stress in the GaN buffer layer while with a continuous graded transition layer (CG) the residual stress in GaN is entirely eliminated, making the GaN buffer fully relaxed. Clover-leaf Hall structures can be fabricated to determine the 2DEG mobility, sheet resistance and sheet charge density. Furthermore, diodes and/or transistors can be fabricated to realize the breakdown voltage, on-resistance and saturation current. Comparisons of electrical properties would provide insight into the effect of buffer layer stress contribution to the AlGa<sub>x</sub>N/GaN heterostructure. The difference in electro-thermal properties (temperature rise in the device during operation) due to different transition layer schemes can also be evaluated using 3D micro-Raman thermography, as reported by Nazari *et al.*<sup>129</sup>. Reduction of transition layer interfaces by switching to CG transition layer should provide better thermal performance.

### **8.3.2 Effect of *in-situ* SiN<sub>x</sub> passivated AlGa<sub>N</sub>/Ga<sub>N</sub> HEMT on surface-state reduction, RF dispersion and device characterization**

Details of structural properties with outstanding 2DEG sheet resistance are demonstrated in Chapter 3. However, detailed insights into the surface state filling and surface state defect reduction need to be performed to understand better and to pinpoint the individual contribution of surface state filling to the 2DEG. C-V may determine the threshold voltages, and frequency dependent conductance measurements could be performed to interrogate the surface-state defect densities. Corresponding RF dispersion and transistor characteristics can also be determined by characterizing the *in-situ* SiN<sub>x</sub> passivated AlGa<sub>N</sub>/Ga<sub>N</sub> HEMT fabricated via photolithography, metal liftoff and dry-etch processes.

### **8.3.3 Build a theoretical model to explain the outstanding electrical performance of Si-rich *in-situ* SiN<sub>x</sub> passivated HEMT**

The typical theoretical model of the 2DEG induced at AlGa<sub>N</sub>/Ga<sub>N</sub> HEMT seems inadequate to explain the outstanding 2DEG properties of Si-rich *in-situ* SiN<sub>x</sub> passivated HEMT, especially the near theoretical limit 2DEG mobility. The typical AlGa<sub>N</sub>/Ga<sub>N</sub> heterostructure model does not consider the contribution of buffer layer piezoelectric contribution to the 2DEG. A new model considering the effect of both buffer layer and barrier layer piezoelectric contribution, as well as effective mass of the charge carrier within the strained buffer layer, needs to be developed to predict the 2DEG properties accurately.

#### **8.3.4 Thermal conductivity comparison of PECVD or LPCVD vs *in-situ* SiN<sub>x</sub>**

Successful integration of CVD diamond to the AlGa<sub>N</sub>/Ga<sub>N</sub> HEMT is realized using *in-situ* SiN<sub>x</sub> as a dielectric adhesion layer. And we have some preliminary data that show SiN<sub>x</sub> grown at elevated temperature is less susceptible to the diamond growth conditions than that of PECVD and LPCVD SiN<sub>x</sub> and has higher density. Although the stoichiometry of the *in-situ* SiN<sub>x</sub> is determined, proper determination of mechanical properties, optical properties and especially the thermal conductivity of *in-situ* SiN<sub>x</sub> need to be determined and compared with the typical PECVD and LPCVD SiN<sub>x</sub>.

#### **8.3.5 Fabrication of RF devices using Diamond-on-AlGa<sub>N</sub>/Ga<sub>N</sub> HEMTs**

While the successful integration of CVD diamond with the AlGa<sub>N</sub>/Ga<sub>N</sub> HEMT is realized with the lowest TBR values ever reported, fabrication and characterization of RF devices need to be performed to fully appreciate the thermal performance of this diamond on Ga<sub>N</sub> stack. Maximum driving powers with corresponding temperature rises need to be evaluated.

#### **8.3.6 TBR Optimization of diamond-AlGa<sub>N</sub>/Ga<sub>N</sub> HEMT by further thinning the SiN<sub>x</sub> thickness**

Higher seeding density with higher lateral diamond growth rate with increased CH<sub>4</sub> concentration seems to increase lateral coverage thereby suppressing degradation to the SiN<sub>x</sub> dielectric adhesion layer. By optimizing the seeding density and growth chemistry either by increasing CH<sub>4</sub> concentration or perhaps by means of a catalyst such as Ni, the lateral growth rate of diamond and, hence, quicker coalesce of the diamond grains will minimize damage to the dielectric adhesion layer.

## REFERENCES

- (1) Wu, Y.-F.; Moore, M.; Saxler, A.; Wisleder, T.; Parikh, P. 40-W/Mm Double Field-Plated GaN HEMTs. In *2006 64th Device Research Conference*; IEEE, 2006; pp 151–152. <https://doi.org/10.1109/DRC.2006.305162>.
- (2) El Fatimy, A.; Dyakonova, N.; Meziani, Y.; Otsuji, T.; Knap, W.; Vandenbrouk, S.; Madjour, K.; Théron, D.; Gaquiere, C.; Poisson, M. A.; et al. AlGa<sub>N</sub>/Ga<sub>N</sub> High Electron Mobility Transistors as a Voltage-Tunable Room Temperature Terahertz Sources. *J. Appl. Phys.* **2010**, *107* (2), 1–5. <https://doi.org/10.1063/1.3291101>.
- (3) Dyakonova, N.; Coquillat, D.; But, D. B.; Teppe, F.; Coulomb, L. C. Terahertz Detection by AlGa<sub>N</sub> / Ga<sub>N</sub> HEMTs at High Intensity. In *2016 21st International Conference on Microwave, Radar and Wireless Communications (MIKON)*; IEEE: Krakow, Poland, 2016; pp 6–8. <https://doi.org/10.1109/MIKON.2016.7492133>.
- (4) Cywinski, G.; Szkudlarek, K.; Yahniuk, I.; Yatsunenko, S.; Siekacz, M.; Skierbiszewski, C.; Knap, W.; But, D. B.; Coquillat, D.; Dyakonova, N.; et al. Ga<sub>N</sub>/AlGa<sub>N</sub> Based Transistors for Terahertz Emitters and Detectors. In *2016 21st International Conference on Microwave, Radar and Wireless Communications (MIKON)*; IEEE, 2016; pp 1–4. <https://doi.org/10.1109/MIKON.2016.7492076>.
- (5) Johnson, J. W.; Piner, E. L.; Vescan, A.; Therrien, R.; Rajagopal, P.; Roberts, J. C.; Brown, J. D.; Singhal, S.; Linthicum, K. J. 12 W/Mm AlGa<sub>N</sub>-Ga<sub>N</sub> HFETs on Silicon Substrates. *IEEE Electron Device Lett.* **2004**, *25* (7), 459–461. <https://doi.org/10.1109/LED.2004.831190>.
- (6) Marti, D.; Tirelli, S.; Alt, A. R.; Roberts, J.; Bolognesi, C. R. 150-GHz Cutoff Frequencies and 2-W/Mm Output Power at 40 GHz in a Millimeter-Wave AlGa<sub>N</sub>/Ga<sub>N</sub> HEMT Technology on Silicon. *IEEE Electron Device Lett.* **2012**, *33* (10), 1372–1374. <https://doi.org/10.1109/LED.2012.2204855>.

- (7) Ambacher, O.; Foutz, B.; Smart, J.; Shealy, J. R.; Weimann, N. G.; Chu, K.; Murphy, M.; Sierakowski, A. J.; Schaff, W. J.; Eastman, L. F.; et al. Two Dimensional Electron Gases Induced by Spontaneous and Piezoelectric Polarization in Undoped and Doped AlGa<sub>N</sub>/Ga<sub>N</sub> Heterostructures. *J. Appl. Phys.* **2000**, *87* (1), 334–344.
- (8) Derluyn, J.; Boeykens, S.; Cheng, K.; Vandersmissen, R.; Das, J.; Ruythooren, W.; Degroote, S.; Leys, M. R.; Germain, M.; Borghs, G. Improvement of AlGa<sub>N</sub>Ga<sub>N</sub> High Electron Mobility Transistor Structures by in Situ Deposition of a Si<sub>3</sub>N<sub>4</sub> surface Layer. *J. Appl. Phys.* **2005**. <https://doi.org/10.1063/1.2008388>.
- (9) Vetury, R.; Zhang, N. Q.; Keller, S.; Misha, U. K. The Impact of Surface States on the DC and RF Characteristics of AlGa<sub>N</sub>/Ga<sub>N</sub> HFETs. *IEEE Trans. Electron Devices* **2001**, *48* (3), 560–566. <https://doi.org/10.1109/16.906451>.
- (10) Meneghesso, G.; Verzellesi, G.; Pierobon, R.; Rampazzo, F.; Chini, A.; Mishra, U. K.; Canali, C.; Zanoni, E. Surface-Related Drain Current Dispersion Effects in AlGa<sub>N</sub>-Ga<sub>N</sub> HEMTs. *IEEE Trans. Electron Devices* **2004**, *51* (10), 1554–1561.
- (11) Omika, K.; Tateno, Y.; Kouchi, T.; Komatani, T.; Yaegassi, S.; Yui, K.; Nakata, K.; Nagamura, N.; Kotsugi, M.; Horiba, K.; et al. Operation Mechanism of Ga<sub>N</sub>-Based Transistors Elucidated by Element-Specific X-Ray Nanospectroscopy. *Sci. Rep.* **2018**, *8* (1), 1–9. <https://doi.org/10.1038/s41598-018-31485-4>.
- (12) Hashizume, T.; Nakasaki, R. Discrete Surface State Related to Nitrogen-Vacancy Defect on Plasma-Treated Ga<sub>N</sub> Surfaces. *Appl. Phys. Lett.* **2002**, *80* (24), 4564–4566. <https://doi.org/10.1063/1.1485309>.
- (13) Derluyn, J.; Boeykens, S.; Cheng, K.; Vandersmissen, R.; Das, J.; Ruythooren, W.; Degroote, S.; Leys, M. R.; Germain, M.; Borghs, G. Improvement of AlGa<sub>N</sub>/Ga<sub>N</sub> High Electron Mobility Transistor Structures by *in Situ* Deposition of a Si<sub>3</sub>N<sub>4</sub> Surface Layer. *J. Appl. Phys.* **2005**, *98* (5), 054501. <https://doi.org/10.1063/1.2008388>.

- (14) Germain, M.; Cheng, K.; Derluyn, J.; Degroote, S.; Das, J.; Lorenz, A.; Marcon, D.; Van Hove, M.; Leys, M.; Borghs, G. In-Situ Passivation Combined with GaN Buffer Optimization for Extremely Low Current Dispersion and Low Gate Leakage in Si<sub>3</sub>N<sub>4</sub>/AlGa<sub>N</sub>/ GaN HEMT Devices on Si (111). *Phys. Status Solidi Curr. Top. Solid State Phys.* **2008**, *5* (6), 2010–2012.  
<https://doi.org/10.1002/pssc.200778688>.
- (15) Jiang, H.; Liu, C.; Chen, Y.; Lu, X.; Tang, C. W.; Lau, K. M. Investigation of in Situ SiN as Gate Dielectric and Surface Passivation for GaN MISHEMTs. *IEEE Trans. Electron Devices* **2017**, *64* (3), 832–839.  
<https://doi.org/10.1109/TED.2016.2638855>.
- (16) Nazari, M.; Hancock, B. L.; Piner, E. L.; Holtz, M. W. Self-Heating in a GaN-Based Heterojunction Field-Effect Transistor Investigated by Ultraviolet and Visible Micro-Raman Spectroscopy. *2015 IEEE Compd. Semicond. Integr. Circuit Symp.* **2015**, *62* (5), 1–4. <https://doi.org/10.1109/CSICS.2015.7314522>.
- (17) Anaya, J.; Rossi, S.; Alomari, M.; Kohn, E.; Tóth, L.; Pécz, B.; Hobart, K. D.; Anderson, T. J.; Feygelson, T. I.; Pate, B. B.; et al. Control of the In-Plane Thermal Conductivity of Ultra-Thin Nanocrystalline Diamond Films through the Grain and Grain Boundary Properties. *Acta Mater.* **2016**, *103*, 141–152.  
<https://doi.org/10.1016/j.actamat.2015.09.045>.
- (18) Cho, J.; Li, Z.; Asheghi, M.; Goodson, K. E. Near-Junction Thermal Management: Thermal Conduction in Gallium Nitride Composite Substrates. *Annu. Rev. Heat Transf.* **2014**, *18*, 1–65.
- (19) Cho, J.; Li, Z.; Bozorg-Grayeli, E.; Kodama, T.; Francis, D.; Ejeckam, F.; Faili, F.; Asheghi, M.; Goodson, K. E. Improved Thermal Interfaces of GaN-Diamond Composite Substrates for HEMT Applications. *IEEE Trans. Components, Packag. Manuf. Technol.* **2013**, *3* (1), 79–85.  
<https://doi.org/10.1109/TCPMT.2012.2223818>.

- (20) Cho, J.; Chu, K. K.; Chao, P. C.; McGray, C.; Asheghi, M.; Goodson, K. E. Thermal Conduction Normal to Thin Silicon Nitride Films on Diamond and GaN. *Thermomechanical Phenom. Electron. Syst. -Proceedings Intersoc. Conf.* **2014**, 1186–1191. <https://doi.org/10.1109/ITHERM.2014.6892414>.
- (21) Wood, C.; Jena, D. *Polarization Effects in Semiconductors: From Ab Initio Theory to Device Applications*; Springer US, 2007.
- (22) Quay, R. *Gallium Nitride Electronics*; Springer Series in Materials Science; Springer Berlin Heidelberg, 2008.
- (23) Ambacher, O.; Smart, J.; Shealy, J. R.; Weimann, N. G.; Chu, K.; Murphy, M.; Schaff, W. J.; Eastman, L. F.; Dimitrov, R.; Wittmer, L.; et al. Two-Dimensional Electron Gases Induced by Spontaneous and Piezoelectric Polarization Charges in N- and Ga-Face AlGaIn/GaN Heterostructures. *J. Appl. Phys.* **1999**, 85 (6), 3222. <https://doi.org/10.1063/1.369664>.
- (24) Ambacher, O. Growth and Applications of Group III-Nitrides. *J. Phys. D. Appl. Phys.* **1998**, 31 (20), 2653–2710. <https://doi.org/10.1088/0022-3727/31/20/001>.
- (25) Higashiwaki, M.; Chowdhury, S.; Miao, M. S.; Swenson, B. L.; Van De Walle, C. G.; Mishra, U. K. Distribution of Donor States on Etched Surface of AlGaIn/GaN Heterostructures. *J. Appl. Phys.* **2010**, 108 (6). <https://doi.org/10.1063/1.3481412>.
- (26) *Chemical Vapour Deposition: Precursors, Processes and Applications*, 2009th ed.; Jones, A. C., Hitchman, M. L., Eds.; Royal Society of Chemistry, [www.rsc.org](http://www.rsc.org).
- (27) Anderson, J. W. Metalorganic Chemical Vapor Deposition and Investigation of AlGaInN Microstructure, Texas State University, <https://digital.library.txstate.edu/handle/10877/5254>, 2014.
- (28) Mishra, U. K.; Shen, L.; Kazior, T. E.; Wu, Y.-F. GaN-Based RF Power Devices and Amplifiers. *Proc. IEEE* **2008**, 96 (2), 287–305.

- (29) Moram, M. A.; Vickers, M. E. X-Ray Diffraction of III-Nitrides. *Reports Prog. Phys.* **2009**, *72* (3), 036502. <https://doi.org/10.1088/0034-4885/72/3/036502>.
- (30) Kadir, A.; Huang, C.; Eng, K.; Lee, K.; Fitzgerald, E. A. System Determination of Alloy Composition and Strain in Multiple AlGa<sub>N</sub> Buffer Layers in GaN / Si System. **2015**, *232113* (2014), 1–6. <https://doi.org/10.1063/1.4904007>.
- (31) Wallis, D. J.; Zhu, D.; Oehler, F.; Westwater, S. P.; Pujol, A.; Humphreys, C. J. Measuring the Composition of AlGa<sub>N</sub> Layers in GaN Based Structures Grown on 150 Mm Si Substrates Using (2 0 5) Reciprocal Space Maps. *Semicond. Sci. Technol.* **2013**, *28* (9), 094006. <https://doi.org/10.1088/0268-1242/28/9/094006>.
- (32) Liu, H. F.; Zhang, L.; Chua, S. J.; Chi, D. Z. Crystallographic Tilt in GaN-on-Si (111) Heterostructures Grown by Metal-Organic Chemical Vapor Deposition. *J. Mater. Sci.* **2014**, *49* (9), 3305–3313. <https://doi.org/10.1007/s10853-014-8025-6>.
- (33) Zhu, D.; McAleese, C.; McLaughlin, K. K.; Häberlen, M.; Salcianu, C. O.; Thrush, E. J.; Kappers, M. J.; Phillips, W. A.; Lane, P.; Wallis, D. J.; et al. GaN-Based LEDs Grown on 6-Inch Diameter Si (111) Substrates by MOVPE. **2009**, *723118* (February 2009), 723118. <https://doi.org/10.1117/12.814919>.
- (34) Liu, H. F.; Dolmanan, S. B.; Bhat, T. N.; Tripathy, S. Comment on “Determination of Alloy Composition and Strain in Multiple AlGa<sub>N</sub> Buffer Layers in GaN/Si System” [Appl. Phys. Lett. 105, 232113 (2014)]. *Appl. Phys. Lett.* **2015**, *106* (17), 2014–2016. <https://doi.org/10.1063/1.4919592>.
- (35) Oehler, F.; Vickers, M. E.; Kappers, M. J.; Humphreys, C. J.; Oliver, R. A. Fundamentals of X-Ray Diffraction Characterisation of Strain in GaN Based Compounds. *Jpn. J. Appl. Phys.* **2013**, *52* (8S), 08JB29. <https://doi.org/10.7567/JJAP.52.08JB29>.

- (36) Jana, S. K.; Mukhopadhyay, P.; Ghosh, S.; Kabi, S.; Bag, A.; Kumar, R.; Biswas, D. High-Resolution X-Ray Diffraction Analysis of  $\text{Al}_x\text{Ga}_{1-x}\text{N}/\text{In}_x\text{Ga}_{1-x}\text{N}/\text{GaN}$  on Sapphire Multilayer Structures: Theoretical, Simulations, and Experimental Observations. *J. Appl. Phys.* **2014**, *115* (17), 174507. <https://doi.org/10.1063/1.4875382>.
- (37) Nazari, M.; Holtz, M. W. Near-Ultraviolet Raman and Micro-Raman Analysis of Electronic Materials. *Appl. Phys. Rev.* **2018**, *5* (4), 041303. <https://doi.org/10.1063/1.5054660>.
- (38) Hancock, B. L.; Nazari, M.; Anderson, J.; Piner, E. L.; Holtz, M. W. Investigation of Stresses in GaN HEMT Layers on a Diamond Substrate Using Micro-Raman Spectroscopy. *Tech. Dig. - IEEE Compd. Semicond. Integr. Circuit Symp. CSIC* **2016**, *2016-Novem*, 1–4. <https://doi.org/10.1109/CSICS.2016.7751050>.
- (39) Kidd, P. XRD of Gallium Nitride and Related Compounds: Strain, Composition and Layer Thickness. *Panalytical X-ray Co.* **2009**.
- (40) Fewster, P. F. X-Ray Analysis of Thin Films and Multilayers. *Reports Prog. Phys.* **1996**, *59* (11), 1339–1407. <https://doi.org/10.1088/0034-4885/59/11/001>.
- (41) Ashcroft, N. W. Vegard's Law. *Phys. Rev. A* **1991**, *43* (6), 3161–3164. <https://doi.org/https://doi.org/10.1103/PhysRevA.43.3161>.
- (42) Kadir, A.; Huang, C. C.; Kian Lee, K. E.; Fitzgerald, E. A.; Chua, S. J. Determination of Alloy Composition and Strain in Multiple AlGa<sub>N</sub> Buffer Layers in GaN/Si System. *Appl. Phys. Lett.* **2014**, *105* (23), 232113. <https://doi.org/10.1063/1.4904007>.
- (43) Vurgaftman, I.; Meyer, J. R.; Ram-Mohan, L. R. Band Parameters for III-V Compound Semiconductors and Their Alloys. *J. Appl. Phys.* **2001**, *89* (11 I), 5815–5875. <https://doi.org/10.1063/1.1368156>.

- (44) Kisielowski, C.; Krüger, J.; Ruvimov, S.; Suski, T.; Ager, J.; Jones, E.; Liliental-Weber, Z.; Rubin, M.; Weber, E.; Bremser, M.; et al. Strain-Related Phenomena in GaN Thin Films. *Phys. Rev. B - Condens. Matter Mater. Phys.* **1996**, *54* (24), 17745–17753. <https://doi.org/10.1103/PhysRevB.54.17745>.
- (45) Sewell, R. H.; Musca, C. A.; Dell, J. M.; Faraone, L.; Usher, B. F.; Dieing, T. High-Resolution X-Ray Diffraction Studies of Molecular Beam Epitaxy-Grown HgCdTe Heterostructures and CdZnTe Substrates. *J. Electron. Mater.* **2005**, *34* (6), 795–803. <https://doi.org/10.1007/s11664-005-0023-7>.
- (46) Harutyunyan, V. S.; Aivazyan, a P.; Weber, E. R.; Kim, Y.; Park, Y.; Subramanya, S. G. High-Resolution x-Ray Diffraction Strain-Stress Analysis of GaN/Sapphire Heterostructures. *J. Phys. D. Appl. Phys.* **2001**, *34* (10A), A35–A39. <https://doi.org/10.1088/0022-3727/34/10A/308>.
- (47) Chowdhury, S.; Biswas, D. Plasma Assisted Molecular Beam Epitaxy Growth and Effect of Varying Buffer Thickness on the Formation of Ultra-Thin In<sub>0.17</sub>Al<sub>0.83</sub>N/GaN Heterostructure on Si(111). *Appl. Phys. Lett.* **2015**, *106* (8). <https://doi.org/10.1063/1.4913843>.
- (48) Ahmad, I.; Holtz, M.; Faleev, N. N.; Temkin, H. Dependence of the Stress-Temperature Coefficient on Dislocation Density in Epitaxial GaN Grown on ??-Al<sub>2</sub>O<sub>3</sub> and 6H-SiC Substrates. *J. Appl. Phys.* **2004**, *95* (4), 1692–1697. <https://doi.org/10.1063/1.1637707>.
- (49) Hancock, B. L.; Nazari, M.; Anderson, J.; Piner, E.; Faili, F.; Oh, S.; Twitchen, D.; Graham, S.; Holtz, M. Ultraviolet Micro-Raman Spectroscopy Stress Mapping of a 75-Mm GaN-on-Diamond Wafer. *Appl. Phys. Lett.* **2016**, *108* (21), 24–29. <https://doi.org/10.1063/1.4952596>.
- (50) Stoev, K.; Sakurai, K. Recent Theoretical Models in Grazing Incidence X-Ray Reflectometry. *Rigaku J* **1997**, *14* (2), 22–37.

- (51) Song, D. Y.; Holtz, M. E.; Chandolu, A.; Bernussi, A.; Nikishin, S. A.; Holtz, M. W.; Gherasoiu, I. Effect of Stress and Free-Carrier Concentration on Photoluminescence in InN. *Appl. Phys. Lett.* **2008**, *92* (12), 1–4. <https://doi.org/10.1063/1.2899941>.
- (52) Wallis, D. J.; Keir, A. M.; Balmer, R. S.; Soley, D. E. J.; Martin, T. Composition Measurement in Strained AlGa<sub>N</sub> Epitaxial Layers Using X-Ray Diffraction. *Appl. Phys. Lett.* **2004**, *85* (26), 6359–6361. <https://doi.org/10.1063/1.1835999>.
- (53) Wright, A. F. Elastic Properties of Zinc-Blende and Wurtzite AlN, GaN, and InN. *J. Appl. Phys.* **1997**, *82* (6), 2833–2839. <https://doi.org/10.1063/1.366114>.
- (54) Ma, J.; Lu, X.; Jiang, H.; Liu, C.; Lau, K. M. In situ Growth of SiN<sub>x</sub> as Gate Dielectric and Surface Passivation for AlN/GaN Heterostructures by Metalorganic Chemical Vapor Deposition. *Appl. Phys. Express* **2014**, *7*, 091002. <https://doi.org/10.7567/APEX.7.091002>.
- (55) Gamarra, P.; Lacam, C.; Tordjman, M.; Medjdoub, F.; di Forte-Poisson, M. A. In-Situ Passivation of Quaternary Barrier InAlGa<sub>N</sub>/Ga<sub>N</sub> HEMTs. *J. Cryst. Growth* **2017**, *464*, 143–147. <https://doi.org/10.1016/j.jcrysgro.2016.11.014>.
- (56) Darakchieva, V.; Beckers, M.; Xie, M. Y.; Hultman, L.; Monemar, B.; Carlin, J. F.; Feltn, E.; Gonschorek, M.; Grandjean, N. Effects of Strain and Composition on the Lattice Parameters and Applicability of Vegard's Rule in Al-Rich Al<sub>1-x</sub>In<sub>x</sub>N Films Grown on Sapphire. *J. Appl. Phys.* **2008**, *103* (10). <https://doi.org/10.1063/1.2924426>.
- (57) Gatabi, I. R.; Johnson, D. W.; Woo, J. H.; Anderson, J. W.; Coan, M. R.; Piner, E. L.; Harris, H. R. PECVD Silicon Nitride Passivation of Algan/Gan Heterostructures. *IEEE Trans. Electron Devices* **2013**, *60* (3), 1082–1087. <https://doi.org/10.1109/TED.2013.2242075>.

- (58) Kojima, I.; Li, B.; Fujimoto, T. High Resolution Thickness and Interface Roughness Characterization in Multilayer Thin Films by Grazing Incidence X-Ray Reflectivity. *Thin Solid Films* **1999**, 355 (1999), 385–389.  
[https://doi.org/10.1016/S0040-6090\(99\)00544-1](https://doi.org/10.1016/S0040-6090(99)00544-1).
- (59) Lugani, L.; Carlin, J. F.; Py, M. A.; Grandjean, N. Thermal Stability and in Situ SiN Passivation of InAlN/GaN High Electron Mobility Heterostructures. *Appl. Phys. Lett.* **2014**, 105 (11). <https://doi.org/10.1063/1.4895807>.
- (60) Pakuła, K.; Bozek, R.; Baranowski, J. M.; Jasinski, J.; Liliental-Weber, Z. Reduction of Dislocation Density in Heteroepitaxial GaN: Role of SiH<sub>4</sub> treatment. *J. Cryst. Growth* **2004**, 267 (1–2), 1–7.  
<https://doi.org/10.1016/j.jcrysgro.2004.03.020>.
- (61) Oliver, R. A.; Kappers, M. J.; Sumner, J.; Datta, R.; Humphreys, C. J. Highlighting Threading Dislocations in MOVPE-Grown GaN Using an in Situ Treatment with SiH<sub>4</sub> and NH<sub>3</sub>. *J. Cryst. Growth* **2006**, 289 (2), 506–514.  
<https://doi.org/10.1016/j.jcrysgro.2005.12.075>.
- (62) Cheng, K.; Leys, M.; Derluyn, J.; Degroote, S.; Xiao, D. P.; Lorenz, A.; Boeykens, S.; Germain, M.; Borghs, G. AlGaIn/GaN HEMT Grown on Large Size Silicon Substrates by MOVPE Capped with in-Situ Deposited Si<sub>3</sub>N<sub>4</sub>. *J. Cryst. Growth* **2007**, 298 (SPEC. ISS), 822–825. <https://doi.org/10.1016/j.jcrysgro.2006.10.185>.
- (63) Darakchieva, V.; Beckers, M.; Xie, M. Y.; Hultman, L.; Monemar, B.; Carlin, J. F.; Feltin, E.; Gonschorek, M.; Grandjean, N. Effects of Strain and Composition on the Lattice Parameters and Applicability of Vegard's Rule in Al-Rich Al<sub>1-x</sub>In<sub>x</sub>N Films Grown on Sapphire. *J. Appl. Phys.* **2008**, 103 (10), 1–7.  
<https://doi.org/10.1063/1.2924426>.
- (64) Masaki, Y.; Gibson, R. A. G.; LeComber, P. G. Structural and Electrical Properties of SiN<sub>x</sub>:H Films. *J. Appl. Phys.* **1993**, 73 (10), 5088–5094.  
<https://doi.org/10.1063/1.353780>.

- (65) Downey, B. P.; Meyer, D. J.; Katzer, D. S.; Marron, T. M.; Pan, M.; Gao, X. Effect of SiN<sub>x</sub>gate Insulator Thickness on Electrical Properties of SiN<sub>x</sub>/In<sub>0.17</sub>Al<sub>0.83</sub>N/AlN/GaN MIS-HEMTs. *Solid. State. Electron.* **2015**, *106*, 12–17. <https://doi.org/10.1016/j.sse.2014.12.025>.
- (66) Koide, N.; Kato, H.; Sassa, M.; Yamasaki, S.; Manabe, K.; Hashimoto, M.; Amano, H.; Hiramatsu, K.; Akasaki, I. Doping of GaN with Si and Properties of Blue m<sup>i</sup>/n/N<sup>+</sup> GaN LED with Si-Doped N<sup>+</sup>-Layer by MOVPE. *J. Cryst. Growth Vol. 115, Issues 1–4, 2 December 1991, Pages 639-642* **1991**, *115* (1–4), 639–642. [https://doi.org/10.1016/0022-0248\(91\)90818-P](https://doi.org/10.1016/0022-0248(91)90818-P).
- (67) Moulder, J. F.; Stickle, W. F.; Sobol, P. E.; Bomben, K. D. Handbook of X-Ray Photoelectron Spectroscopy Edited By. *Handb. X-ray Photoelectron Spectrosc.* **1992**, 261.
- (68) Blech, M.; Laades, A.; Ronning, C.; Schröter, B.; Borschel, C.; Rzesanke, D.; Lawerenz, A. Detailed Study of {PECVD} Silicon Nitride and Correlation of Various Characterization Techniques. *24th Eur. Photovolt. Sol. Energy Conf.* **2009**, 507–511. <https://doi.org/10.4229/24thEUPVSEC2009-1CV.4.30>.
- (69) Azize, M.; Palacios, T. Effect of Substrate-Induced Strain in the Transport Properties of AlGa<sub>N</sub>/Ga<sub>N</sub> Heterostructures. *J. Appl. Phys.* **2010**, *108* (2), 023707. <https://doi.org/10.1063/1.3463150>.
- (70) Kang, B. S.; Kim, S.; Kim, J.; Ren, F.; Baik, K.; Pearton, S. J.; Gila, B. P.; Abernathy, C. R.; Pan, C.-C.; Chen, G.-T.; et al. Effect of External Strain on the Conductivity of AlGa<sub>N</sub>/Ga<sub>N</sub> High-Electron-Mobility Transistors. *Appl. Phys. Lett.* **2003**, *83* (23), 4845–4847. <https://doi.org/10.1063/1.1631054>.
- (71) Dreyer, C. E.; Janotti, A.; Van de Walle, C. G. Effects of Strain on the Electron Effective Mass in Ga<sub>N</sub> and Al<sub>N</sub>. *Appl. Phys. Lett.* **2013**, *102* (14), 142105. <https://doi.org/10.1063/1.4801520>.

- (72) Beechem, T.; Christensen, A.; Green, D. S.; Graham, S. Assessment of Stress Contributions in GaN High Electron Mobility Transistors of Differing Substrates Using Raman Spectroscopy. *J. Appl. Phys.* **2009**, *106* (11).  
<https://doi.org/10.1063/1.3267157>.
- (73) Sarua, A.; Ji, H.; Hilton, K. P.; Wallis, D. J.; Uren, M. J.; Martin, T.; Kuball, M. Thermal Boundary Resistance Between GaN and Substrate in AlGaN / GaN Electronic Devices. **2007**, *54* (12), 3152–3158.
- (74) Blevins, J. D.; Via, G. D.; Sutherlin, K.; Tetlak, S.; Poling, B.; Gilbert, R.; Moore, B.; Hoelscher, J.; Stumpff, B.; Bar-Cohen, A.; et al. Recent Progress in GaN-on-Diamond Device Technology. *CS MANTECH 2014 - 2014 Int. Conf. Compd. Semicond. Manuf. Technol.* **2014**, 105–108.
- (75) Kuzmík, J.; Tapajna, M.; Válik, L.; Molnár, M.; Donoval, D.; Fleury, C. C.; Pogany, D.; Strasser, G.; Hilt, O.; Brunner, F.; et al. Self-Heating in GaN Transistors Designed for High-Power Operation. *IEEE Electron Device Lett.* **2014**, *61* (10), 3429–3434. <https://doi.org/10.1109/TED.2014.2350516>.
- (76) Ejeckam, F.; Francis, D.; Faili, F.; Twitchen, D.; Bolliger, B.; Babic, D.; Felbinger, J. S2-T1: GaN-on-Diamond: A Brief History. *Lester Eastman Conf. 2014 - High Perform. Devices, LEC 2014* **2014**, No. April 2016.  
<https://doi.org/10.1109/LEC.2014.6951556>.
- (77) Mishra, U.; Singh, J. *Semiconductor Device Physics and Design*; 2007.
- (78) Jessen, G. H.; Gillespie, J. K.; Via, G. D.; Crespo, A.; Langley, D.; Wasserbauer, J.; Faili, F.; Francis, D.; Babic, D.; Ejeckam, F.; et al. AlGaN / GaN HEMT on Diamond Technology Demonstration. *IEEE Compd. Semicond. Integr. Circuit Symp. Tech. Dig.* **2006**, 271–274.

- (79) Cho, J.; Won, Y.; Francis, D.; Asheghi, M.; Goodson, K. E. Thermal Interface Resistance Measurements for GaN-on-Diamond Composite Substrates. *Tech. Dig. - IEEE Compd. Semicond. Integr. Circuit Symp. CSIC* **2014**, 1–4. <https://doi.org/10.1109/CSICS.2014.6978583>.
- (80) Ejeckam, F.; Francis, D.; Faili, F.; Twitchen, D.; Bolliger, B.; Felbinger, J. GaN-on-Diamond : A Brief History. **2005**.
- (81) Pomeroy, J.; Bernardoni, M.; Sarua, A.; Manoi, A.; Dumka, D. C.; Fanning, D. M.; Kuball, M. Achieving the Best Thermal Performance for GaN-on-Diamond. In *Technical Digest - IEEE Compound Semiconductor Integrated Circuit Symposium, CSIC*; 2013. <https://doi.org/10.1109/CSICS.2013.6659210>.
- (82) Pomeroy, J. W.; Bernardoni, M.; Dumka, D. C.; Fanning, D. M.; Kuball, M. Low Thermal Resistance GaN-on-Diamond Transistors Characterized by Three-Dimensional Raman Thermography Mapping. *Appl. Phys. Lett.* **2014**, *104* (8), 0–5. <https://doi.org/10.1063/1.4865583>.
- (83) Hemts, H. P. G.; Chu, K. K.; Chao, P. C.; Diaz, J. A.; Yurovchak, T.; Creamer, C. T.; Sweetland, S.; Kallaher, R. L.; Mcgray, C. Low-Temperature Substrate Bonding Technology For. **2014**, 1–4.
- (84) Sun, H.; Simon, R. B.; Pomeroy, J. W.; Francis, D.; Faili, F.; Twitchen, D. J.; Kuball, M. Reducing GaN-on-Diamond Interfacial Thermal Resistance for High Power Transistor Applications. *Appl. Phys. Lett.* **2015**, *106* (11), 111906. <https://doi.org/10.1063/1.4913430>.
- (85) Asubar, J. T.; Yatabe, Z.; Hashizume, T. Reduced Thermal Resistance in AlGaN / GaN Multi-Mesa-Channel High Electron Mobility Transistors Reduced Thermal Resistance in AlGaN / GaN Multi-Mesa-Channel High Electron Mobility Transistors. **2014**, *053510* (2014), 4–9. <https://doi.org/10.1063/1.4892538>.

- (86) Sun, H.; Pomeroy, J. W.; Simon, R. B.; Francis, D.; Faili, F.; Twitchen, D. J.; Kuball, M. Temperature-Dependent Thermal Resistance of GaN-on-Diamond HEMT Wafers. *IEEE Electron Device Lett.* **2016**, *37* (5), 621–624.  
<https://doi.org/10.1109/LED.2016.2537835>.
- (87) Coe, S. ; Sussmann, R. . Optical, Thermal and Mechanical Properties of CVD Diamond. *Diam. Relat. Mater.* **2000**, *9* (9–10), 1726–1729.  
[https://doi.org/10.1016/S0925-9635\(00\)00298-3](https://doi.org/10.1016/S0925-9635(00)00298-3).
- (88) Altman, D.; Tyhach, M.; McClymonds, J.; Kim, S.; Graham, S.; Cho, J.; Goodson, K.; Francis, D.; Faili, F.; Ejeckam, F.; et al. Analysis and Characterization of Thermal Transport in GaN HEMTs on Diamond Substrates. In *Fourteenth Intersociety Conference on Thermal and Thermomechanical Phenomena in Electronic Systems (ITherm)*; IEEE, 2014; pp 1199–1205.  
<https://doi.org/10.1109/ITHERM.2014.6892416>.
- (89) Anderson, T. J.; Hobart, K. D.; Tadjer, M. J.; Koehler, A. D.; Imhoff, E. A.; Hite, J. K.; Feygelson, T. I.; Pate, B. B.; Eddy, C. R.; Kub, F. J. Nanocrystalline Diamond Integration with III-Nitride HEMTs. *ECS J. Solid State Sci. Technol.* **2017**, *6* (2), Q3036–Q3039. <https://doi.org/10.1149/2.0071702jss>.
- (90) Meyer, D. J.; Feygelson, T. I.; Anderson, T. J.; Roussos, J. A.; Tadjer, M. J.; Downey, B. P.; Katzer, D. S.; Pate, B. B.; Ancona, M. G.; Koehler, A. D.; et al. Large-Signal RF Performance of Nanocrystalline Diamond Coated AlGaIn/GaN High Electron Mobility Transistors. *IEEE Electron Device Lett.* **2014**, *35* (10), 1013–1015. <https://doi.org/10.1109/LED.2014.2345631>.
- (91) Anderson, T. J.; Hobart, K. D.; Tadjer, M. J.; Koehler, A. D.; Feygelson, T. I.; Hite, J. K.; Pate, B. B.; Kub, F. J.; Eddy, C. R. Nanocrystalline Diamond for near Junction Heat Spreading in GaN Power HEMTs. *Tech. Dig. - IEEE Compd. Semicond. Integr. Circuit Symp. CSIC* **2013**, 8–11.  
<https://doi.org/10.1109/CSICS.2013.6659241>.

- (92) Tadjer, M. J.; Anderson, T. J.; Hobart, K. D.; Mastro, M. A.; Hite, J. K.; Caldwell, J. D.; Picard, Y. N.; Kub, F. J.; Eddy, C. R. Electrical and Optical Characterization of AlGaN/GaN HEMTs with in Situ and Ex Situ Deposited SiN<sub>x</sub> Layers. *J. Electron. Mater.* **2010**, *39* (11), 2452–2458. <https://doi.org/10.1007/s11664-010-1343-9>.
- (93) Zhou, Y.; Ramaneti, R.; Anaya, J.; Korneychuk, S.; Derluyn, J.; Sun, H.; Pomeroy, J.; Verbeeck, J.; Haenen, K.; Kuball, M. Thermal Characterization of Polycrystalline Diamond Thin Film Heat Spreaders Grown on GaN HEMTs. *Appl. Phys. Lett.* **2017**, *111* (4). <https://doi.org/10.1063/1.4995407>.
- (94) Babchenko, O.; Vanko, G.; Gerboc, M.; Ižák, T.; Vojs, M.; Lalinský, T.; Kromka, A. Study on Electronic Properties of Diamond/SiN<sub>x</sub>-Coated AlGaN/GaN High Electron Mobility Transistors Operating up to 500 °C. *Diam. Relat. Mater.* **2018**, *89* (5), 266–272. <https://doi.org/10.1016/j.diamond.2018.09.014>.
- (95) Seelmann-Eggebert, M.; Meisen, P.; Schaudel, F.; Koidl, P.; Vescan, A.; Leier, H. Heat-Spreading Diamond Films for GaN-Based High-Power Transistor Devices. *Diam. Relat. Mater.* **2001**, *10* (3–7), 744–749. [https://doi.org/10.1016/S0925-9635\(00\)00562-8](https://doi.org/10.1016/S0925-9635(00)00562-8).
- (96) Tadjer, M. J.; Anderson, T. J.; Hobart, K. D.; Feygelson, T. I.; Caldwell, J. D.; Eddy, C. R.; Kub, F. J.; Butler, J. E.; Pate, B.; Melngailis, J. Reduced Self-Heating in AlGaN/GaN HEMTs Using Nanocrystalline Diamond Heat-Spreading Films. *IEEE Electron Device Lett.* **2012**, *33* (1), 23–25. <https://doi.org/10.1109/LED.2011.2171031>.
- (97) Gan, A.; Wang, A.; Tadjer, M. J.; Anderson, T. J.; Baranyai, R.; Pomeroy, J. W.; Feygelson, T. I.; Hobart, K. D.; Pate, B. B.; Calle, F.; et al. Impact of Intrinsic Stress in Diamond Capping Layers on the Electrical. *IEEE Trans. Electron Devices* **2013**, *60* (10), 3149–3156. <https://doi.org/10.1109/TED.2013.2275031>.

- (98) Zhou, Y.; Anaya, J.; Pomeroy, J.; Sun, H.; Gu, X.; Xie, A.; Beam, E.; Becker, M.; Grotjohn, T. A.; Lee, C.; et al. Barrier-Layer Optimization for Enhanced GaN-on-Diamond Device Cooling. *ACS Appl. Mater. Interfaces* **2017**, *9* (39), 34416–34422. <https://doi.org/10.1021/acsami.7b08961>.
- (99) Anderson, T. J.; Hobart, K. D.; Tadjer, M. J.; Koehler, A. D.; Imhoff, E. A.; Hite, J. K.; Feygelson, T. I.; Pate, B. B.; Eddy, C. R.; Kub, F. J. Nanocrystalline Diamond Integration with III-Nitride HEMTs. *ECS J. Solid State Sci. Technol.* **2017**, *6* (2), Q3036–Q3039. <https://doi.org/10.1149/2.0071702jss>.
- (100) Ahmed, R.; Nazari, M.; Hancock, B. L.; Simpson, J.; Engdahl, C.; Piner, E. L.; Holtz, M. W. Ultraviolet Micro-Raman Stress Map of Polycrystalline Diamond Grown Selectively on Silicon Substrates Using Chemical Vapor Deposition. *Appl. Phys. Lett.* **2018**, *112* (18), 181907. <https://doi.org/10.1063/1.5027507>.
- (101) Bougher, T. L.; Yates, L.; Lo, C. F.; Johnson, W.; Graham, S.; Cola, B. A. Thermal Boundary Resistance in GaN Films Measured by Time Domain Thermoreflectance with Robust Monte Carlo Uncertainty Estimation. *Nanoscale Microscale Thermophys. Eng.* **2016**, *20* (1), 22–32. <https://doi.org/10.1080/15567265.2016.1154630>.
- (102) Huang, H.; Winchester, K. J.; Suvorova, A.; Lawn, B. R.; Liu, Y.; Hu, X. Z.; Dell, J. M.; Faraone, L. Effect of Deposition Conditions on Mechanical Properties of Low-Temperature PECVD Silicon Nitride Films. *Mater. Sci. Eng. A* **2006**, *435–436*, 453–459. <https://doi.org/10.1016/j.msea.2006.07.015>.
- (103) Stoffel, A.; Kovács, A.; Kronast, W.; Müller, B. LPCVD against PECVD for Micromechanical Applications. *J. Micromechanics Microengineering* **1996**, *6* (1), 1–13. <https://doi.org/10.1088/0960-1317/6/1/001>.

- (104) Siddique, A.; Ahmed, R.; Anderson, J.; Piner, E. L. Effect of Reactant Gas Stoichiometry of In-Situ SiN<sub>x</sub> Passivation on Structural Properties of MOCVD AlGaN/GaN HEMTs. *J. Cryst. Growth* **2019**, *517* (March), 28–34.  
<https://doi.org/10.1016/j.jcrysgro.2019.03.020>.
- (105) Umeno, Y.; Kubo, A.; Nagao, S. Density Functional Theory Calculation of Ideal Strength of SiC and GaN: Effect of Multi-Axial Stress. *Comput. Mater. Sci.* **2015**, *109*, 105–110. <https://doi.org/10.1016/j.commatsci.2015.07.025>.
- (106) Bergman, L.; Dutta, M.; Balkas, C.; Davis, R. F.; Christman, J. A.; Alexson, D.; Nemanich, R. J. Raman Analysis of the E1 and A1 Quasi-Longitudinal Optical and Quasi-Transverse Optical Modes in Wurtzite AlN. *J. Appl. Phys.* **1999**, *85* (7), 3535–3539. <https://doi.org/10.1063/1.369712>.
- (107) Kozawa, T.; Kachi, T.; Kano, H.; Taga, Y.; Hashimoto, M.; Koide, N.; Manabe, K. Raman Scattering from LO Phonon-Plasmon Coupled Modes in Gallium Nitride. *J. Appl. Phys.* **1994**, *75* (2), 1098–1101. <https://doi.org/10.1063/1.356492>.
- (108) Prokofyeva, T.; Seon, M.; Vanbuskirk, J.; Holtz, M.; Nikishin, S. A.; Faleev, N. N.; Temkin, H.; Zollner, S. Vibrational Properties of AlN Grown on (111)-Oriented Silicon. *Phys. Rev. B - Condens. Matter Mater. Phys.* **2001**, *63* (12), 1–7. <https://doi.org/10.1103/PhysRevB.63.125313>.
- (109) Harima, H. Properties of GaN and Related Compounds Studied by Means of Raman Scattering. *J. Phys. Condens. Matter* **2002**, *14* (38), R967–R993.  
<https://doi.org/10.1088/0953-8984/14/38/201>.
- (110) Ma, J.; Lu, X.; Zhu, X. L.; Huang, T. D.; Xu, P. Q.; Lau, K. M. MOVPE Growth of in Situ SiN<sub>x</sub> / AlN / GaN MISHEMTs with Low Leakage Current and High on / off Current Ratio. **2014**, *3998* (2000), 5–6.

- (111) Ahmed, R.; Siddique, A.; Anderson, J.; Engdahl, C.; Holtz, M.; Piner, E. Selective Area Deposition of Hot Filament CVD Diamond on 100 Mm MOCVD Grown AlGaIn/GaN Wafers. *Cryst. Growth Des.* **2019**, *19* (2), 672–677. <https://doi.org/10.1021/acs.cgd.8b01260>.
- (112) Oliphant, C. J.; Arendse, C. J.; Camagu, S. T.; Swart, H. EBSD Analysis of Tungsten-Filament Carburization during the Hot-Wire CVD of Multi-Walled Carbon Nanotubes. *Microsc. Microanal.* **2014**, *20* (1), 4–13. <https://doi.org/10.1017/S1431927613014001>.
- (113) Klein, P. B.; Binari, S. C.; Ikossi, K.; Wickenden, A. E.; Koleske, D. D.; Henry, R. L. Current Collapse and the Role of Carbon in AlGaIn/GaN High Electron Mobility Transistors Grown by Metalorganic Vapor-Phase Epitaxy. *Appl. Phys. Lett.* **2001**, *79* (21), 3527–3529. <https://doi.org/10.1063/1.1418452>.
- (114) Leapman, R. D.; Hunt, J. A. Comparison of Detection Limits for EELS and EDXS. *Microsc. Microanal. Microstruct.* **1991**, *2* (2–3), 231–244. <https://doi.org/10.1051/mmm:0199100202-3023100>.
- (115) Gengler, J. J.; Roy, S.; Jones, J. G.; Gord, J. R. Two-Color Time-Domain Thermoreflectance of Various Metal Transducers with an Optical Parametric Oscillator. *Meas. Sci. Technol.* **2012**, *23* (5). <https://doi.org/10.1088/0957-0233/23/5/055205>.
- (116) Yates, L.; Anderson, J.; Gu, X.; Lee, C.; Bai, T.; Mecklenburg, M.; Aoki, T.; Goorsky, M. S.; Kuball, M.; Piner, E. L.; et al. Low Thermal Boundary Resistance Interfaces for GaN-on-Diamond Devices. *ACS Appl. Mater. Interfaces* **2018**, *10* (28), 24302–24309. <https://doi.org/10.1021/acsami.8b07014>.

- (117) Yates, L.; Sood, A.; Cheng, Z.; Bougher, T.; Malcolm, K.; Cho, J.; Asheghi, M.; Goodson, K.; Goorsky, M.; Faili, F.; et al. Characterization of the Thermal Conductivity of CVD Diamond for GaN-on-Diamond Devices. *Tech. Dig. - IEEE Compd. Semicond. Integr. Circuit Symp. CSIC* **2016**, 2016-Novem, 31–34. <https://doi.org/10.1109/CSICS.2016.7751032>.
- (118) Bougher, T. L.; Yates, L.; Cheng, Z.; Cola, B. A.; Graham, S.; Chaeito, R.; Sood, A.; Ashegi, M.; Goodson, K. E. Experimental Considerations of CVD Diamond Film Measurements Using Time Domain Thermoreflectance. In *2017 16th IEEE Intersociety Conference on Thermal and Thermomechanical Phenomena in Electronic Systems (ITherm)*; IEEE, 2017; pp 30–38. <https://doi.org/10.1109/ITHERM.2017.7991853>.
- (119) Liu, J.; Zhu, J.; Tian, M.; Gu, X.; Schmidt, A.; Yang, R. Simultaneous Measurement of Thermal Conductivity and Heat Capacity of Bulk and Thin Film Materials Using Frequency-Dependent Transient Thermoreflectance Method. *Rev. Sci. Instrum.* **2013**, 84 (3). <https://doi.org/10.1063/1.4797479>.
- (120) Liu, W.; Balandin, A. A. Temperature Dependence of Thermal Conductivity of Al XGa 1-x Thin Films Measured by the Differential  $3\omega$  Technique. *Appl. Phys. Lett.* **2004**, 85 (22), 5230–5232. <https://doi.org/10.1063/1.1829168>.
- (121) Zhao, Y.; Zhu, C.; Wang, S.; Tian, J. Z.; Yang, D. J.; Chen, C. K.; Cheng, H.; Hing, P. Pulsed Photothermal Reflectance Measurement of the Thermal Conductivity of Sputtered Aluminum Nitride Thin Films. *J. Appl. Phys.* **2004**, 96 (8), 4563–4568. <https://doi.org/10.1063/1.1785850>.
- (122) Slack, G. A. Nonmetallic Crystals with High Thermal Conductivity. *J. Phys. Chem. Solids* **1973**, 34 (2), 321–335. [https://doi.org/10.1016/0022-3697\(73\)90092-9](https://doi.org/10.1016/0022-3697(73)90092-9).

- (123) Freedman, J. P.; Leach, J. H.; Preble, E. A.; Sitar, Z.; Davis, R. F.; Malen, J. A. Universal Phonon Mean Free Path Spectra in Crystalline Semiconductors at High Temperature. *Sci. Rep.* **2013**, *3*, 1–6. <https://doi.org/10.1038/srep02963>.
- (124) Kuo, P. K.; Auner, G. W.; Wu, Z. L. Microstructure and Thermal Conductivity of Epitaxial AlN Thin Films. *Thin Solid Films* **1994**, *253* (1–2), 223–227. [https://doi.org/10.1016/0040-6090\(94\)90324-7](https://doi.org/10.1016/0040-6090(94)90324-7).
- (125) Watari, K.; Shinde, S. L. High Thermal Conductivity Materials. *MRS Bull.* **2001**, *26* (06), 440–444. <https://doi.org/10.1557/mrs2001.113>.
- (126) Braun, J. L.; Hopkins, P. E. Upper Limit to the Thermal Penetration Depth during Modulated Heating of Multilayer Thin Films with Pulsed and Continuous Wave Lasers: A Numerical Study. *J. Appl. Phys.* **2017**, *121* (17). <https://doi.org/10.1063/1.4982915>.
- (127) Brown, J. D.; Borges, R.; Piner, E.; Vescan, A.; Singhal, S.; Therrien, R. AlGaIn/GaN HFETs Fabricated on 100-Mm GaN on Silicon (111) Substrates. *Solid. State. Electron.* **2002**, *46* (10), 1535–1539. [https://doi.org/10.1016/S0038-1101\(02\)00101-6](https://doi.org/10.1016/S0038-1101(02)00101-6).
- (128) Thermoreflectance, M. T.; Cheng, Z.; Bougher, T.; Bai, T.; Wang, S. Y.; Li, C.; Yates, L.; Foley, B.; Goorsky, M. S.; Cola, B. A.; et al. Probing Growth-Induced Anisotropic Thermal Transport in High-Quality CVD Diamond Membranes by Multi-Frequency Probing Growth-Induced Anisotropic Thermal Transport in High-Quality CVD Diamond George W. Woodruff School of Mechanical Engineering, Georgia I. **2018**. <https://doi.org/10.1021/acsami.7b16812>.
- (129) Nazari, M.; Hancock, B. L.; Piner, E. L.; Holtz, M. W. Self-Heating Profile in an AlGaIn/GaN Heterojunction Field-Effect Transistor Studied by Ultraviolet and Visible Micro-Raman Spectroscopy. *IEEE Trans. Electron Devices* **2015**, *62* (5). <https://doi.org/10.1109/TED.2015.2414718>.